



Virginia Commonwealth University
VCU Scholars Compass

Theses and Dissertations

Graduate School

2020

Synthesis of Supported Metal Nanoparticles on High Surface Area Supports for Application in Energy Conversion and Heterogeneous Catalysis

Nazgol Norouzi
Virginia Commonwealth University

Follow this and additional works at: <https://scholarscompass.vcu.edu/etd>

 Part of the [Inorganic Chemistry Commons](#), and the [Materials Chemistry Commons](#)

© The Author

Downloaded from

<https://scholarscompass.vcu.edu/etd/6251>

This Dissertation is brought to you for free and open access by the Graduate School at VCU Scholars Compass. It has been accepted for inclusion in Theses and Dissertations by an authorized administrator of VCU Scholars Compass. For more information, please contact libcompass@vcu.edu.

Copyright © Nazgol Norouzi 2020

All Rights Reserved

**Synthesis of Supported Metal Nanoparticles on High Surface
Area Supports for Application in Energy Conversion and
Heterogeneous Catalysis**

A dissertation submitted in partial fulfillment of the requirements for the degree of Doctor of Philosophy in Nanoscience and Nanotechnology at Virginia Commonwealth University.

by

Nazgol Norouzi

Bachelor of Science,

Azad University, Science and Research Branch, 2012

Master of Product Innovation,

Virginia Commonwealth University, 2014

Director: Dr. Hani M. El-Kaderi, Associate

Professor, Department of Chemistry

Virginia Commonwealth University

Richmond, Virginia

May, 2020

Acknowledgments

I would like to acknowledge the support and guidance of my advisor, Dr. Hani M. El-Kaderi, whose ideas, encouragement and patience have made all of this possible. The things I have learned from him are beyond chemistry and I will always be truly grateful for all the effort he has made to advance my research skills. I would also like to express my sincere appreciation for my committee members, the amazing Dr. Puru Jena, Dr. Indika U. Arachchige, and Dr. Katharine Tibbetts for their invaluable input, in pursuit of my Ph.D. degree. I am very thankful to Dr. Dmitry Pestov and Dr. Joseph Turner for training me on how to operate various characterization instruments. I want to acknowledge Dr. Samy M. El-shall for his support throughout our collaborations. I would also like to acknowledge the Nanoscience and Nanotechnology program of Virginia Commonwealth University for providing me the opportunity to pursue my Ph.D. studies. I wish to thank the Chemistry Department of Virginia Commonwealth University for providing a great atmosphere for completing my research.

I am thankful to all my previous and current colleagues in the lab, Dr. Pezhman Arab, Dr. Babak Ashourirad, Dr. Timur Islamoglu, Dr. Tsemre Tessema, Dr. Yomna Abdelmoaty, Dr. Fatema Choudhury, Dr. Ahmed Alzharani, Shamara Weeraratne, Ahmed Abdelkader, Omniya Alomainy, Alexander Richard, and Mohammad Shahab, for their continuous help and support. Special thanks to Shamara and Fatema for encouraging and

helping me as a friend. I would also like to thank our collaborators Dr. Noushin Mir, Dr. Dylan Rodene, and Mrinmoy Das. It has been a pleasure to work with all of you.

Finally, I would like to acknowledge my parents, Shahin Nematzadeh and Ali Norouzi, without their unconditional love, continuous support, and encouragement none of this would be possible. I would like to acknowledge my sister and best friend, Nahal Norouzi (Lili), for being there for me and telling me how it is. Finally, I would like to thank my partner, Adel Shahrezaei, for his love, care, and sense of adventure. I feel truly blessed to have these people in my life.

This work is dedicated to my mother, Shahin Nematzadeh.

TABLE OF CONTENTS

LIST OF TABLES	xi
LIST OF FIGURES	xiii
Chapter 1	23
Introduction.....	23
1.1 High Surface Area Supports.....	23
1.2 Fuel Cells	25
.....	27
1.2.1 ORR Reaction in Fuel Cells.....	27
1.2.2 Pt Loaded Carbon and Platinum Group Metal Catalysts	28
1.2.3 Heteroatom and Transition Metal Dopants	29
1.2.4 Iron and Phosphorus-doped Carbon as a New Class of Electrocatalysts	32
1.3 Cross-coupling Reactions	34
1.3.1 Heterogeneous Catalysts for Cross-coupling Reactions	35
1.3.2 Palladium Metal as an Active center in Cross-coupling Reactions	37
1.3.3 Suzuki-Miyaura Reaction	38
1.3.4 Characteristics of an Outstanding Heterogeneous Catalysts	39

1.4 Lithium Sulfur Batteries	45
1.4.1 Lithium Ion and Lithium Sulfur Batteries	45
1.4.2 Lithium-sulfur Batteries Operating Principles.....	47
1.4.3 Optimization of Cathode for Lithium-sulfur Batteries	48
1.5 Thesis Statement	51
References.....	55
Chapter 2.....	64
Characterization Techniques and Instrumentations	64
2.1 Introduction.....	64
2.2 Characterization techniques	65
2.3 Oxygen Reduction Reaction	69
2.3.1 Electrochemical Measurements Instrumentation.....	69
2.3.2 Catalyst Preparation.....	75
2.4 Lithium-sulfur Batteries.....	75
2.4.1 Electrode and coin cell Preparation	75
References.....	78
Chapter 3.....	79
Iron Phosphide Doped Porous Carbon as an Efficient Electrocatalyst for Oxygen Reduction Reaction.....	79
3.1 Introduction.....	79

3.2 Experimental Section	82
3.2.1 Sample Preparation	82
.....	83
3.2.2 Electrochemical Measurements	84
3.2.3 Physical Characterization.....	85
3.3 Result and Discussion	87
3.3.1 Characterization	87
3.3.2 Electrochemical Measurements	103
3.4 conclusion	113
References.....	114
Chapter 4.....	117
Heterogeneous Catalysis by Ultra-small Bimetallic Nanoparticles Surpassing Homogeneous Catalysis for Carbon-Carbon Bond Forming Reactions	117
4.1 Introduction.....	117
4.2 Experimental Section.....	119
4.2.1 Materials and Preparation of Silica Supported Bimetallic Nanoparticles	119
4.2.2 Instrumentation	119
4.2.3 Suzuki Cross-coupling reaction at room temperature and pressure condition	121
4.2.4 Suzuki Cross-coupling Reaction at Microwave reaction condition	121

4.3 Results and Discussions	123
4.3.1 Catalysts Preparation and Characterization	123
4.3.2 Catalysts Characterization	125
4.4 Suzuki cross-coupling catalytic performance	140
4.4.1 Catalyst Recycling Studies under Microwave Irradiation	142
4.5 Conclusion	148
References	150
Chapter 5	153
5.1 Introduction	153
5.2 Experimental Section	154
5.2.1 Synthesis of Nitrogen-doped Carbon Support	154
5.2.2 Strong Electrostatic Adsorption	156
.....	158
5.2.3 Electrochemical Measurements	159
5.2.4 Instrumentation	161
5.3 Result and Discussion	163
5.3.1 Characterization	163
5.3.2 Electrochemical Measurements	170
5.4 Outlook	177
5.5 conclusion	179
References	180

Chapter 6.....	182
Conclusions and Outlook.....	182

LIST OF TABLES

Table 3.1 Textural Properties of PFeCs Determined by Nitrogen Porosity Measurements.	89
Table 3.2 Surface and bulk chemical composition of PFeC-800, 900, 1000 and PC-900 collected from XPS, EDX and the iron weight percent collected from ICP-OES.....	97
Table 3.3 Electrocatalytic Activity, Onset Potential, Half Wave Potential and Limiting Current of PFeC-800, 900, 1000, PC-900 and Pt/C in O ₂ Saturated 0.1 M KOH.	104
Table 3.4 Comparison of preparation methods and ORR activities of reported phosphorus-doped, Iron phosphorous-doped electrocatalysts with PFeC-900 and PC-900 in 0.1 M KOH (Al.) medium or 0.1 M HClO ₄ / 0.5 M H ₂ SO ₄ (Ac.). (If the exact values are not mentioned in the paper, an estimated number from the corresponding graphs is used for this Table.).....	112
Table 4.1 Bulk composition of metals for mono and bimetallic samples collected by ICP-OES. (BM stands for base metal).....	127
Table 4.2 Bulk composition of various metal loading for Cu-Pd combination collected by ICP- OES	127

Table 4.3 Bulk composition of metals for Pd/SiO ₂ catalyst after each recycling run.	128
Table 4.4 Bulk composition of metals for CuPd/SiO ₂ catalyst after each recycling run.	128
Table 4.5 Surface composition of mono and bimetallic samples. Collected with XPS.	136
Table 4.6 Surface composition of CuPd/SiO ₂ and the 3 rd and 6 th recycled catalysts. Collected with XPS.	136
Table 4.7. Recyclability of CuPd/SiO ₂ for Suzuki cross-coupling.	144
Table 4.8 Biphenyl conversions for recyclability of Pd/SiO ₂ for Suzuki cross-coupling.....	144
Table 4.9. TON and TOF calculation for bimetallic catalysts and 1 Pd for different mol% Pd.....	146

LIST OF FIGURES

Figure 1.1 (a) Alkaline fuel cell with platinum loaded carbon catalyst, Apollo lunar mission, NASA space program. (b) a schematic of an alkaline fuel cell.....	27
Figure 1.2 ORR electron transfer mechanism on the Pt catalyst in alkaline medium. (Copyright 2012 Advances in Physical Chemistry).....	29
Figure 1.3 Cobalt phthalocyanines, as a catalyst for the ORR and the half-cell voltage and current density data reported. (Copyright 1964 Nature)	30
Figure 1.4 Heteroatom doping effects on surface charge distribution. (Copyright 2009 Science).....	31
.....	31
Figure 1.5 ORR mechanism catalyzed by FN_4 active centers in an alkaline electrolyte. (Copyright 2012 Advances in Physical Chemistry).....	31
Figure 1.6 ORR catalyzed by Fe-P active centers in an alkaline electrolyte. (Copyright 2015 Journal of American Chemical Society)	33
Figure 1.7 Cross-coupling catalytic cycle for Pd catalyzed reactions.	35
Figure 1.8 Different catalytically active species of a Heterogeneous catalyst in Suzuki cross-coupling reaction. (Copyright 2017 American Chemical Society).....	36

Figure 1.9 (a) Schematic of the SEA synthesis technique: Electrostatic adsorption of the mixed monolayer of charged precursors on the Silica support, and formation of the alloyed nanoparticles upon reduction with hydrogen at elevated temperatures. (b) ultrasmall bimetallic nanoparticles deposited on the surface of silica. (Copyright 2017 Science).....	42
Figure 1.10 Schematic of a lithium-sulfur batteries.....	46
Figure 1.11 Operating principle of LSBs.....	48
Figure 2.1 Schematic of an alkaline and acidic half-cell electrochemistry setup.....	71
Figure 2.2 Ring and disk currents at 60°C for the determination of the collection efficiency on a Pt/C thin-film RRDE in 0.1 M NaOH supporting electrolyte with 10 mM K ₃ Fe(CN) ₆ . Positive sweeps at 20 mV s ⁻¹ ; E _{Ring} =1.55 V. (Copyright 2001 Journal of the Electrochemical Chemistry).....	74
Figure 2.3 The order of the coin cell components.	76
Figure 3.1 Reaction schematic of PFeC-900 and PC-900.	83
Figure 3.2 (a) N ₂ sorption isotherm of PFeC-800, PFeC-900, PFeC-1000, and PC-900 at 77 K (solid symbols denote adsorption points, and hollow symbols denote desorption points; isotherms are offset in steps of 100). (b) Pore size distribution from NLDFT model using N ₂ isotherms at 77 K (PSD curves are offset in steps of 1). The inset in panel b compares the pore size distribution in the range of 4–15 nm without an offset.	88

Figure 3.3 (a) P-XRD patterns for PFeCs and PC-900. The inset depicts the detailed pattern for PC-900. (b) Raman spectra with corresponding D and G bands. 91

Figure 3.4 (a) Survey spectra of PFeC-800. (b) Deconvoluted C 1s spectra. (c) Deconvoluted P 2p spectra. (d) Deconvoluted Fe 2p spectra. (e) Deconvoluted O 2p spectra. 93

Figure 3.5 (a) Survey spectra of PFeC-900. (b) Deconvoluted C 1s spectra. (c) Deconvoluted P 2p spectra. (d) Deconvoluted Fe 2p spectra. (e) Deconvoluted O 2p spectra. 94

Figure 3.6 (a) Survey spectra of PFeC-1000 (b) Deconvoluted C 1s spectra (c) Deconvoluted P 2p spectra (d) Deconvoluted Fe 2p spectra (e) Deconvoluted O 1s spectra. 95

Figure 3.7 (a) Survey spectra of PC-900 (b) Deconvoluted C 1s spectra (c) Deconvoluted P 2p spectra (d) Deconvoluted O 1s spectra..... 96
 99
 99

Figure 3.8 (a–d) SEM images of PFeC-800. (e–i) EDX elemental mapping displaying the distribution of elements in PFeC-800..... 99

Figure 3.9 (a–d) SEM images of PFeC-900. (e–i) EDX elemental mapping displaying the distribution of elements in PFeC-900..... 100

Figure 3.10 (a–d) SEM images of PFeC-1000. (e–i) EDX elemental mapping displaying the distribution of elements in PFeC-1000..... 101

Figure 3.11 (a–d) SEM images of PC-900. (e–h) EDX elemental mapping displaying the distribution of elements in PC-900..... 102

Figure 3.12 (a) LSV curves for PFeC-800, -900, and -1000, PC-900, and Pt/C in O₂-saturated 0.1 M KOH using RRDE and the corresponding ring current densities. (b) Polarization curves for PFeC-900 in O₂-saturated 0.1 M KOH at rotation rates 100–2500 rpm. (c) Top graph, H₂O⁻ % and bottom graph, electron transfer numbers for PFeC-900, PC-900, and Pt/C calculated from the LSV curves at 1600 rpm, and (d) Tafel slopes for PFeC-900 and Pt/C. 105

Figure 3.13 The CV of (a) PFeC-900 and (b) Pt/C (c) PFeC-800, (d) PFeC-1000 (e) PC-900 in N₂ and O₂ saturated 0.1 M KOH using RDE at scan rate of 50 mV s⁻¹.. 107

Figure 3.14 (a) LSV curves for PFeC-900, PC-900, and Pt/C in O₂-saturated 0.5 M H₂SO₄ using RRDE and their corresponding ring currents. (b) Top graph, H₂O₂ yielded % and bottom graph, electron transfer numbers for PFeC-900, PC-900, and Pt/C calculated from the LSV curves at 1600 rpm..... 109

Figure 3.15 The polarization curves for PFeC-900 in O₂ saturated 0.5 M H₂SO₄ at rotation rates 100-2500 rpm..... 109

Figure 3.16 The CV of (a) PFeC-900. (b) Pt/C in N₂ and O₂ saturated 0.5 M H₂SO₄ using RDE at scan rate of 50 mV s⁻¹. 110

Figure 3.17 Comparison between onset potentials in O₂ saturated (a) 0.1 M KOH. (b) 0.5 M H₂SO₄ using RDDE at 1600 rpm and scan rate of 10 mV s⁻¹. 110

Figure 3.18 (a) Durability test. (b) Chronoamperometric response of PFeC-900 and Pt/C with the addition of 3 M methanol at 500 s at the rotation rate of 1600 rpm. The inset in panel b shows behavior of PFeC-900 in the first hour. 111

..... 125

Figure 4.1 SEA and Co-SEA reaction schematic. 125

Figure 4.2 TPR patterns for (a) Pd/SiO₂, Cu/SiO₂, and CuPd/SiO₂, (b) Pd/SiO₂, Ni/SiO₂, and NiPd/SiO₂, and (c) Pd/SiO₂, Co/SiO₂, and CoPd/SiO₂. 130

Figure 4.3 (a) XRD patterns for all mono and bimetallic catalysts. (b) XRD patterns for pristine CuPd/SiO₂ and consecutive recycling test catalysts..... 131

Figure 4.4 XPS spectra of all bimetallic and monometallic samples (a) Survey spectra (b) Deconvoluted Si 2p spectra, (c) Deconvoluted O 1s spectra, (d) Deconvoluted Cu 2p spectra, (e) Deconvoluted Ni 2p spectra, (f) Deconvoluted Co 2p spectra, (g) Deconvoluted Pd 3d spectra..... 135

Figure 4.5 HRTEM, STEM, and the corresponding particle size distribution for (a) Pd/SiO₂, (b) CuPd/SiO₂, (c) NiPd/SiO₂ and (d) CoPd/SiO₂. 138

..... 139

Figure 4.6 HRTEM, STEM and the corresponding particle size distribution for (a) CuPd/SiO₂ 3rd, (b) CuPd/SiO₂ 6th recycled runs. 139

Figure 4.7 (a) Cross-coupling reaction between Bromobenzene with benzenboronic acid (b) Biphenyl conversion of mono and bimetallic NP, (c) biphenyl conversion of various dilution of Pd in Cu NP. 142

Figure 4.8 Biphenyl Conversion % for bimetallic catalysts and 1 Pd for different mol% Pd. 145

Figure 4.9 Aryl bromide (0.32 mmol, 1 equiv), arylboronic acid (0.38 mmol, 1.2 equiv), potassium carbonate (133 mg, 0.96 mmol, 3 equiv), and 1Cu1Pd (10.5 mg, 1.05 mmol, 0.3 mol %) in 4 mL (1:1 H₂O–EtOH) was heated at 60 °C (MWI) for 5 min. Conversion (%) was determined by GC–FID analysis. 147

Figure 5.1 (a) Thermogravimetric analysis of a pure organic building block versus a mixture of BI with KOH. (b) The reaction of the organic building block with KOH and conversion to porous carbon using excess KOH. (Copyright 2016 American Chemical Society) 156

Figure 5.2 Final pH vs. initial pH, PZC measured using pH drift method. 157

Figure 5.3 Synthesis of Ni/BIDC-900 using the SEA method. 158

Figure 5.4 (a) N₂ sorption isotherm of BIDC-900 at 77 K (solid symbols denote adsorption points, and hollow symbols denote desorption points). (b) Pore size distribution from QSDFT model using N₂ isotherms at 77 K. 164

Figure 5.5 P-XRD patterns for BIDC-900 and Ni/BIDC-900. 165

Figure 5.6 (a) Survey spectra of Ni/BIDC-900. (b) Deconvoluted C 1s spectra. (c) Deconvoluted N 1s spectra. (d) Deconvoluted O 1s spectra. (e) Deconvoluted Ni 2p spectra.	168
Figure 5.7 HRTEM, STEM, and the corresponding particle size distribution for Ni/BIDC-900.....	169
Figure 5.8 cyclic voltammetry profile of S/Ni-BIDC-900 and S/BIDC-900 collected at a scan rate of 0.1 mV S^{-1} in the potential range 1.75–3 V	171
Figure 5.9 The charge/discharge voltage profile for the 5 cycles at 0.05 C for (a) S/Ni/BIDC-900 and (b) S/BIDC-900.....	174
Figure 5.10 The charge/discharge profile of S/Ni/BIDC-900 with S loading of 4.20 mgs cm^{-1} at 0.05-2C.	175
Figure 5.11 The rate performances of S/Ni/BIDC-900 at current densities varying from 0.05 to 2C.	176
Figure 5.12 long-term stability (50 cycles) and coulombic efficiency of S/Ni/BIDC-900.	177

ABSTRACT

Synthesis of Supported Metal Nanoparticles on High Surface Area Supports for Application in Energy Conversion and Heterogeneous Catalysis

By Nazgol Norouzi, Ph.D.

A dissertation submitted in partial fulfillment of the requirements for the degree of Doctor of Philosophy in Nanoscience and Nanotechnology at Virginia Commonwealth University.

Virginia Commonwealth University, 2020

Director: Hani M. El-Kaderi, Associate Professor, Department of Chemistry

Precise control of metal nanoparticles' size, composition, and dispersity over high surface area supports are highly desirable to address current challenges in energy storage and conversion as well as catalytic processes involving precious metals. Therefore, developing viable synthetic routes that enable new catalytic systems derived from inexpensive transition metals or limited use of precious metals is vital for clean energy

applications such as fuel cells and rechargeable batteries or affordable drugs in the pharmaceuticals arena. In addition to metal components of heterogeneous catalysts, the catalyst support is an integral part of catalyst design as it can impart both physical stability and catalytic enhancement through strong metal-support interactions. In particular, recent studies have shown that the incorporation of heteroatoms like nitrogen and phosphorus in high surface area carbon supports is an effective approach for tailoring the textural and electronic properties of carbon supports.

Here we introduce different supported metal nanoparticles on high surface area supports, with their characteristic tuned toward different applications. In the first project, we developed an iron phosphide doped porous carbon system (PFeC) and used it as a cathode catalyst for oxygen reduction reaction (ORR) in fuel cells. The conversion of chemical energy to electrical energy is a sustainable approach for energy production achieved by fuel cells. Currently, the noble metal platinum, in the form of 20 wt% Pd deposited on carbon support (Pt/C) is the commercially available catalyst for the ORR. Sluggish ORR mechanism and lack of long-term stability demand for a more sustainable, inexpensive, and kinetically efficient replacement catalyst. Here iron phosphide nanoparticles (NPs) incorporated in a phosphorus-doped porous carbon, with a high specific area ($S_{\text{BET}} = 967 \text{ m}^2 \text{ g}^{-1}$) was synthesized using inexpensive reactants, triphenylphosphine and iron chloride by a facile carbonization/chemical activation method via zinc chloride. PFeC selectively reduces O_2 via an efficient reaction pathway and exhibits superior long-term stability than Pt/C. The superior electrocatalytic performance is credited to the synergistic effects between the P and Fe which, form well-defined and well-distributed nanoparticles confined in highly porous carbon nanosheets.

In the second project, supported palladium-based ultra-small bimetallic NPs deposited on mesoporous fumed silica support ($S_{\text{BET}} = 350 \text{ m}^2 \text{ g}^{-1}$) were synthesized and used as a catalyst for Suzuki -Miyaura cross-coupling (SCC) reactions. Bimetallic NPs consisting of active metal Pd and base metals (Cu, Ni, and Co) were deposited on the silica support through strong electrostatic (SEA) synthesis method yielding homogeneously alloyed nanoparticles with an average size of 1.3 nm. All bimetallic catalysts were found to be highly active toward SCC surpassing the activity of monometallic Pd/SiO₂. In particular, the catalyst consisting of Cu and Pd (CuPd/SiO₂), performed the SCC with a remarkable turn over frequency of 248000. The combination of Pd with base metals helps in retaining the Pd⁰ status by charge donation from base metals to Pd and thus facilitating the SCC, in specific lowering the activation energy of the aryl halide oxidative addition rate-limiting step.

In the third and last project, functionalized supports are widely utilized in energy conversion and energy storage applications. High surface area porous carbon materials have been introduced as a highly active cathode material for Lithium-sulfur batteries (LSB). The electrochemical performance of the LSB can be largely improved by the efficient reversible conversion of lithium polysulfides to Li₂S during discharge and to elemental sulfur during charge. Nickel NPs deposited on high surface area nitrogen-doped carbon support (Ni/BIDC-900, $S_{\text{BET}} = 3560 \text{ m}^2 \text{ g}^{-1}$) act as active centers for the adsorption of polysulfides during the discharge process and rapidly convert them to Li₂S while catalyzing Li₂S oxidation to sulfur in the reverse process. The addition of Ni NPs improves the reaction kinetics and activity retention of the LSB.

Chapter 1

Introduction

1.1 High Surface Area Supports

Carbon allotropes, metalloids, metal, and metal oxides are used as support surfaces for a variety of applications, among them, elements of group IV (group 14, new IUPAC notation), especially carbon and silicon, have unprecedented advantages. C and Si are among the most abundant elements on the earth. Having four valence electrons induces a strong tendency for covalent bonding and the formation of extended networks. Their unique ability to bind to themselves and nearly all elements in wide varieties is made possible by the formation of a network consisting of sp^3 , sp^2 , and sp , hybridization states.¹ C and Si frameworks have a high specific surface area ($100\text{-}3000\text{ m}^2\text{ g}^{-1}$) and unique chemical and physical properties, such as chemical and thermal stability, and conductivity.^{2,3} These high surface area supports are considered as low-dimensional nanostructured materials, which their behavior is dominated by a surface phenomenon. Synthesis strategies can be used for modifying the surface of the nanostructured supports with atomic precision. Among the support surfaces, carbon nanostructured are the most versatile. Apart from the two natural carbon allotropes, diamond and graphite, many carbon allotropes are synthesized such as fullerenes, carbon nanotubes, carbon nanofibers,

graphene, amorphous carbon, and glassy carbon. Graphene is the youngest synthesized carbon allotropes, the extended aromatic carbon sheets are extensively studied as a theoretical material, and much later after its discovery was produced through mechanical exfoliation of graphite.⁴ Applicability of carbon nanostructures was vastly expanded by the introduction of amorphous carbon materials in which the structures entails all hybridization states of carbon in different ratios controlled by synthesis, yielding different chemical and physical properties.⁵

Incorporation of heteroatoms and metals on the supports is a practical approach for modifying their various physical and chemical properties and can be achieved by simultaneous or stepwise fashions. In general, the introduction of heteroatoms (N, B, P, S, O) generates defects on the aromatic structure, often increasing the reactivity of the surface of nanostructures.^{6,7} The presence of heteroatoms in the carbon framework induces many changes such as the d-spacing, pore structure, and a more pronounced acidic or basic character than parent materials.⁸ The heteroatom generated functional groups can act as anchoring sites promoting the nucleation of metal nanostructures and their uniform dispersion on the support in both solid-solid or solid-liquid reaction media.^{9,10} The metal and heteroatom can also be simultaneously introduced into the carbon framework through many synthetic methods such as carbonization and chemical activation.^{11,12} Alternatively, nanostructured metals can also be synthesized ex-situ and then deposited on the support surface.¹³

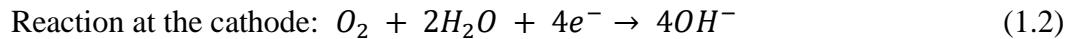
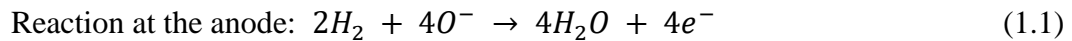
Metal and heteroatom functionalized carbon materials are used in a wide range of applications, such as electronics, optics, environmental protection, energy conversion,

energy storage, catalysis, and chemical synthesis.¹⁴⁻¹⁶ We will discuss the synthesis of iron and phosphorus-doped porous carbon support as a cathode catalyst for oxygen reduction reaction in fuel cells, palladium and transition metal alloyed nanoparticles deposited on high surface area silica support as a heterogeneous catalyst for Suzuki-Miyaura reactions, and nickel nanoparticles supported on a nitrogen-doped porous carbon as a cathode material for lithium-sulfur batteries.

1.2 Fuel Cells

The U.S. Energy Information Administration (EIA) has projected an 11% growth in energy consumption across all energy provider sectors by the year 2050, with petroleum and natural gas supplying 48% of the demand.¹⁷ The continuous increase in energy demands worldwide and the environmental concerns that are reaching a critical level have required the development of clean and sustainable energy conversion devices to be prioritized. Fuel cells and batteries with high efficiency and low-cost become the prime candidates. In the case of fuel cells, having high efficiency, minimal harmful environmental impact, and an unlimited source of reactants, they can also produce electricity, water, and heat. Their widespread use is expected in stationary and portable power generation devices and transportation. Among fuel cells, the proton exchange membrane fuel cell (PEMFC) is most exploited, its operation requires H₂ fuel and ambient air as the oxidant. Even with low Pt catalyst loading of 0.125 mg_{Pt} cm⁻² it has shown high peak power density of 1.24 W c⁻².¹⁸ The current state of the art PEMFCs has been modestly adapted in the commercial sectors, but it is not able to match the long-term goals set by the U.S. Department of Energy (DOE) for light-duty vehicle fuel cells.¹⁹ The main drawback of PEMFC is the use of an

acidic membrane and consequential corrosion of fuel cell components under the acidic environment. This drawback has led to the transition to alkaline membranes and gain in the popularity for anion exchange membrane fuel cells (AEMFC). The prime advantage of AEMFCs is that they operate at higher pH, which in turn provides a less corrosive environment (Fig. 1.1). The main challenge associated with AEMFCs is the more complex water dynamic. The water produced at the anode as the result of hydrogen oxidation reaction (HOR) (Eq. 1.1), diffuses through the membrane in order to participate in oxygen reduction reaction (ORR, Eq 1.2). Diffusion deficiencies and changes in volume are the reasons behind the water dynamic induced complexities.²⁰



Another challenge with AEMFCs is the ability of CO₂ to dissolve in aqueous solutions which leads to deteriorating impacts on the overall efficiency of the fuel cell.²¹ The two pathways that can introduce CO₂ into the system are related to the use of non-purified air tanks and CO₂ as the byproduct of organic fuels oxidation such as oxidation of methanol. The first harmful impact of CO₂ is that the dissolved CO₂ can react with alkaline electrolyte (KOH) and produce potassium carbonate and water. The unencountered produced water by this undesired side reaction contributes to the water dynamics complexities mentioned earlier. The other byproduct, potassium carbonate, has its challenges; it has low solubility at low temperatures which leads to its gradual precipitation in the pores of the membrane and eventually blocks the pores. This phenomenon is only reversible at high temperatures, which are desirable for AEMFC. A rapid solution for the

pore blockage problem is changing the KOH electrolyte. The second harmful impact of the presence of CO_2 in AEMFCs is its reaction with the hydroxide ions produced by the ORR reaction at the cathode and the production of the carbonate ion and water. The production of carbonate ions is known as the “cell carbonation” which can lead to voltage losses of 100-400 mV.^{22,23} Removal of CO_2 remains as one of the main challenges for the development of AEMFCs. To meet DOE long-term cost goals for commercial availability of fuel cells, replacing noble metal catalysts in the cathode is required.¹⁸

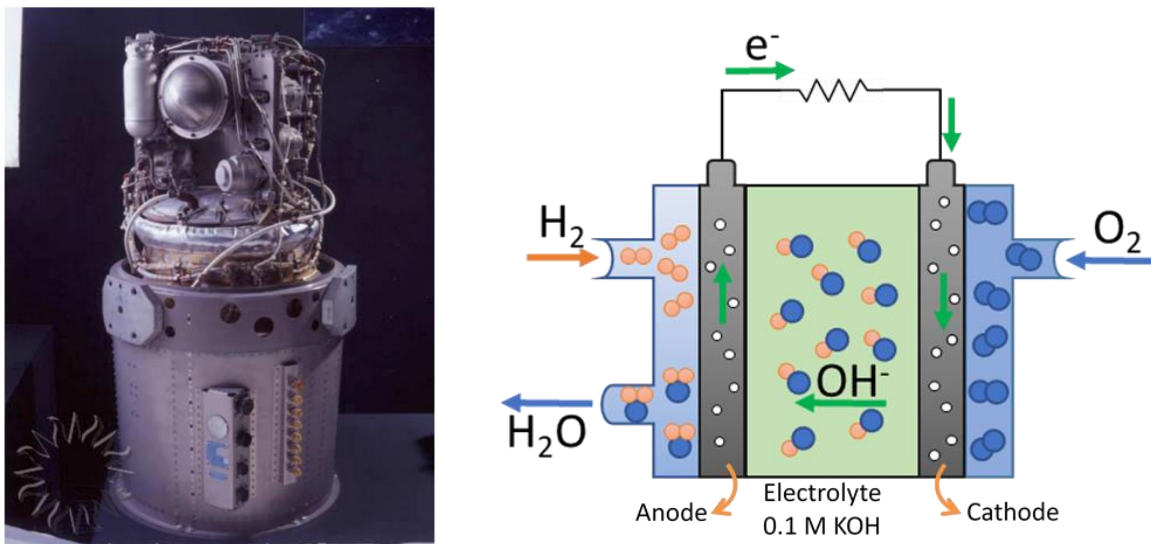
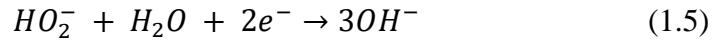
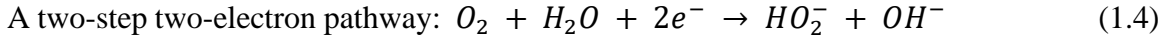
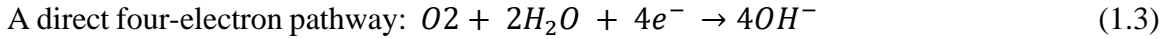


Figure 1.1 (a) Alkaline fuel cell with platinum loaded carbon catalyst, Apollo lunar mission, NASA space program. (b) a schematic of an alkaline fuel cell.

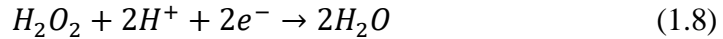
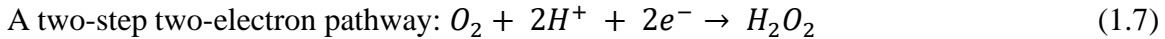
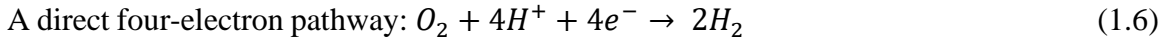
1.2.1 ORR Reaction in Fuel Cells

From here on, we will be focusing on the ORR reaction that takes place at the cathode in both alkaline and acidic electrolytes. ORR is expected to proceed via a

combination of two reaction pathways; a two-step $2e^-$ and a single-step $4e^-$ reaction. (Eqs. 1.3-1.9)



The first reaction pathway (Eq. 1.3) is kinetically fast and ensures higher efficiency as appose to the two-step two-electron reaction pathway (Eqs. 1.4 and 1.5). ORR in acidic electrolyte proceeds via the combination of two reaction pathways as well, a single-step $4e^-$ reaction (Eq. 1.6) and a two-step $2e^-$ (Eqs. 1.7-1.9), as shown below:



1.2.2 Pt Loaded Carbon and Platinum Group Metal Catalysts

In fuel cells, Pt/C and platinum group metal (PGM) are the catalysts of choice for the anodic oxidation of H_2 and the cathodic reduction of O_2 . The electrocatalysis process for the reduction of oxygen is initiated by the adsorption of the oxygen molecule on the surface of Pt catalyst and a simultaneous transfer of an electron and formation of superoxide radical anion. The anion is dissolved and subsequently adsorbed on the oxide Pt surface and followed by proton transfer to form adsorbed hydroperoxyl radical (Fig. 1.2).²⁴

The large-scale commercial production of such fuel cells is restricted by their prohibitive cost, limited supply, and weak durability.²⁵ The vulnerability of PGM to potential drift over time, sluggish reduction reaction in the cathode, and decline of activity through methanol poisoning undermine its competitive catalytic activity. Therefore, the development of electrocatalysts that have facile synthesis and low cost are based on earth-abundant elements that are in high demand.

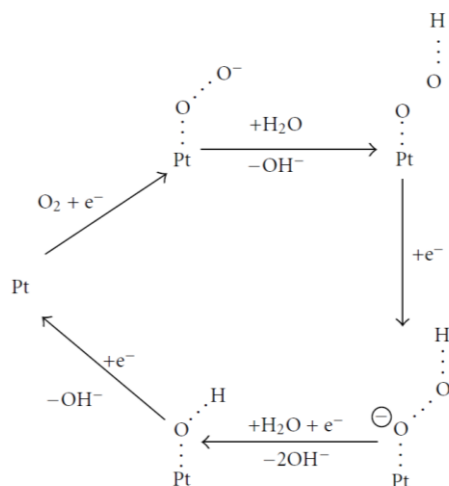


Figure 1.2 ORR electron transfer mechanism on the Pt catalyst in alkaline medium. (Copyright 2012 Advances in Physical Chemistry).

1.2.3 Heteroatom and Transition Metal Dopants

The first non-platinum catalyst was introduced by Jasinski, in 1964.²⁶ Following the use of metal phthalocyanines as catalysts for the oxidation of organic molecules, he investigated the use of transition metal phthalocyanines as the fuel cell cathode catalysts. It was reported that cobalt phthalocyanines activate oxygen in fuel cells even at room

temperature (Fig. 1.3). Transition metal especially iron coordinated with four nitrogen atoms has become one of the most investigated and best catalysts for the replacement of Pt in fuel cells, which will be discussed later in this chapter.

Table 2. LIFE-TEST OF A COBALT PHTHALOCYANINE CATHODE

Time (h)	Cathode voltage (V) (vs. SCE)	Current density (amp/sq.ft.)
0	-0.33	18
14	-0.33	18
20	-0.40	36
25	-0.47	54
51	-0.49	54
95	-0.56	54
96	-0.37	36
148	-0.41	36
245	-0.40	36
246	-0.49	54
289	-0.48	54
435	-0.47	54
461	-0.45	54
519	-0.45	54
591	-0.44	54
615	-0.45	54

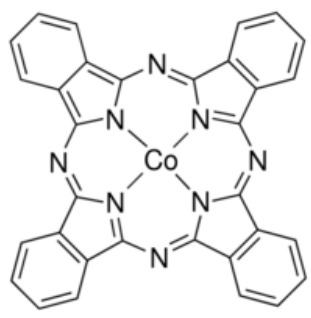


Figure 1.3 Cobalt phthalocyanines, as a catalyst for the ORR and the half-cell voltage and current density data, reported. (Copyright 1964 Nature)

A natural successor, heteroatom-doped porous carbon with a high specific surface area and tunable pore size coupled with suitable acceptor atoms such as nitrogen and phosphorus make porous carbon very effective electrocatalysts (Fig. 1.4).^{27,28} Also, dual-dopants combinations of heteroatom and transition metal doped, porous carbon materials are considered among the best candidates because of their high abundance and low cost. Electrocatalysts composed from transition metals and nitrogen-doped carbon materials or solely nitrogen-doped carbons have shown competitive performance toward the ORR.^{27,29,30} Their surface characteristics and active site components are thoroughly studied and relatively well understood.^{31,32} Fe-N₄/C is considered to be the most competitive ORR

active centers, in which the degree of π -electron delocalization on disordered graphitic carbon basal planes can sufficiently adsorb oxygen molecule and the reactions intermediates (Fig. 1.5).³³

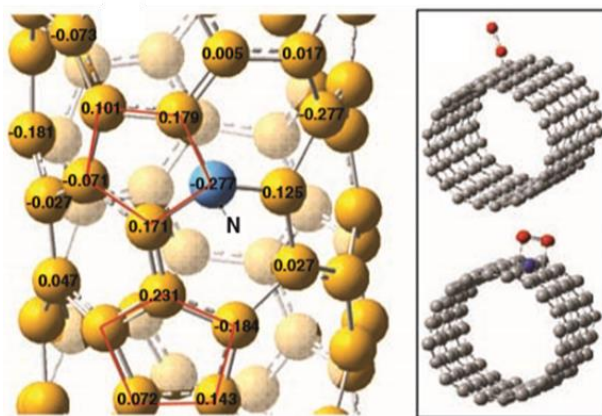


Figure 1.4 Heteroatom doping effects on surface charge distribution. (Copyright 2009 Science)

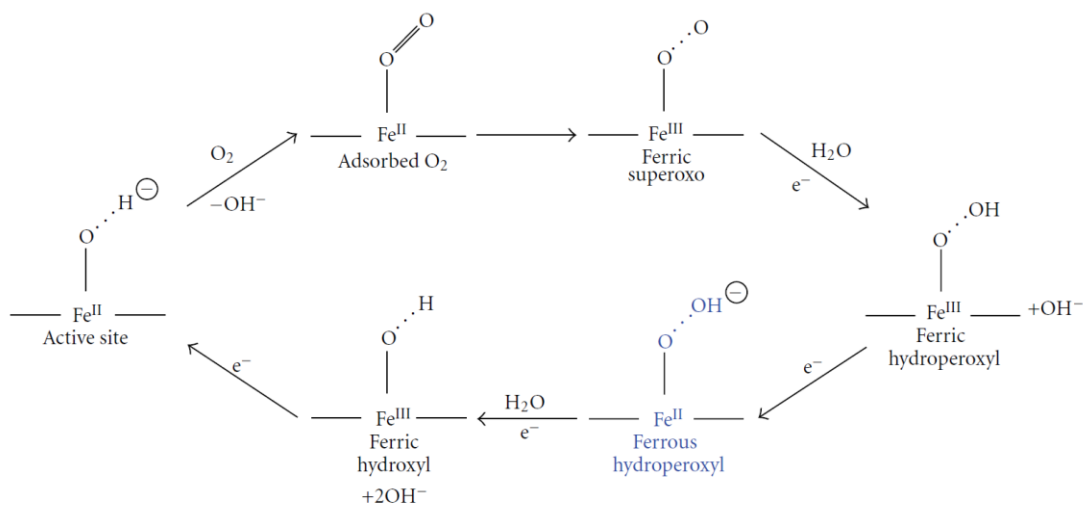


Figure 1.5 ORR mechanism catalyzed by FN₄ active centers in an alkaline electrolyte. (Copyright 2012 Advances in Physical Chemistry)

1.2.4 Iron and Phosphorus-doped Carbon as a New Class of Electrocatalysts

In addition to nitrogen doping, phosphorus-doped carbon has emerged as a potential electrocatalyst due to its long-term stability and high methanol crossover tolerance.^{34–36} Unlike nitrogen, phosphorus has a larger atomic radius and higher electron-donating ability which modifies the electron transport properties of the graphitized porous carbon. Furthermore, the lower electronegativity of phosphorus modifies the charge distribution and electronic properties of high surface area porous carbon. As a result, P-doped graphitized carbon has a higher affinity for O₂ (acceptor molecule), which enhances the overall electrocatalytic activity toward ORR.³⁷ On the other hand, DFT studies on P-doped graphene suggest that the formation of the ORR intermediate is favorable.³⁸ While non-noble metals typically lead to peroxide intermediates as the product of a two-step 2e⁻ transfer reduction reaction, DFT calculations indicated that O₂ and other ORR intermediates can stably adsorb on Fe sites.³⁹ Incorporation of iron into a phosphorus-doped carbon matrix through high-temperature carbonization has led to the formation of various Fe-P compounds giving rise to a series of ORR active electrocatalysts having enhanced kinetics in both alkaline and acidic electrolytes, highlighting the newly found synergistic effects between Fe and P, improving the reaction kinetics in acidic medium (Fig. 1.6).¹¹ Another method for catalyst design entails surface functionalization of graphene with P and Fe, which provides catalytic activity and an onset potential close to that of the commercially available Pt/C.⁴⁰ Also, FeP nanoparticles embedded in P and N-doped carbon nanosheets have been reported to enhance the electron transfer number towards a more selective 4e⁻ reduction reaction.⁴¹ More recently, Fe₂P nanoparticles

derived from a biogenic precursor, encapsulated in a heteroatom-doped graphene-like carbon, have shown promising activity towards ORR in both acidic and alkaline electrolytes.⁴² The advantages of a heteroatom-doped porous carbon are 2-fold: stabilization of the nonprecious metal in the alkaline and acidic solution and generation of active sites for facilitating the ORR. As transition metal phosphide catalysts are on the rise⁴³ and with recent literature reporting good electrocatalytic activity for Fe and P-doped carbon, developing new synthetic strategies to enhance ORR activities have the potential to transform the field. In general, reported electrocatalysts are synthesized via multistep reactions yielding a range of complexes that can be bonded to the carbon matrix, trapped inside the pores, or adsorbed on the surface. These catalysts are prone to leaching,¹¹ while surface treatment with Fe and P leads to catalysts lacking long-term stability.⁴⁰ Moreover, the exact role of P and Fe dopants and their deliberate and unavoidable surface adsorbed oxide species remain poorly understood. Despite competitive onset potentials, the negatively shifted half-wave potentials and sluggish kinetics of the two-step $2e^-$ reduction pathway still hamper the electrocatalytic activity of these catalysts.

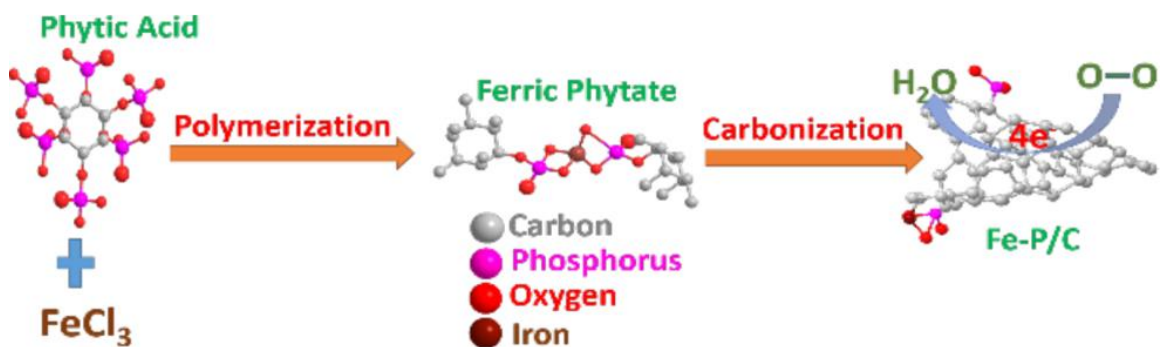


Figure 1.6 ORR catalyzed by Fe-P active centers in an alkaline electrolyte. (Copyright 2015 Journal of American Chemical Society)

1.3 Cross-coupling Reactions

Cross-coupling reactions are widely encountered in the synthesis of complex organic molecules including drugs and other advanced functional materials. Reactions such as, Heck, Kumada, Suzuki, Miyaura, Mizoroki, Negishi, Stille, and Sonogashira, named after predominant scientists who partake in the revolutionary, and scientific approach to cross-coupling reactions. They have set in stone the investigation into the cross-coupling reaction mechanisms, and product formation. The importance of a cross-coupling reaction was recognized by awarding the Nobel Prize in chemistry to professor Akira Suzuki, professor Heck, and professor Negishi in 2010. Homogeneous catalysis has been long utilized for cross-coupling reactions due to its effectiveness in achieving high activity and turnover in a wide variety of functional groups.⁴⁴ Homogenous catalysis is initiated by in situ activation of the Pd complex, in which Pd⁺² is reduced to Pd⁰. In the oxidative addition step the organic halide attacks the metal center, in this process both the oxidation state and the coordination number of the metal center increase. The base dissociation in the reaction solution will detach the halide ion from the Pd complex. The catalytic cycle proceeds to the transmetallation step in which aryl boronic acid and the base form a chemical bond and the aryl group attaches to the Pd metal center. The catalytic cycle continues by reductive elimination Pd complex and the biphenyl is produced. The presence of an oxidant in the system returns the Pd center to its original Pd⁺² oxidation state (Fig. 1.7). In homogenous cross-coupling ligands play an important role. The effects of the ligands on the electronic structure of the Pd metal center directly influence the oxidative addition and reductive elimination steps in the catalytic cycle. Oxidative addition is considered as the rate-limiting

step,^{45,46} to facilitate this step, the effects of various ligands have been studied. It should also be mentioned that in many catalytic systems, the activity and selectivity of the catalyst are controlled by the characteristic of the ligand.⁴⁷ It is well understood that electron-rich ligands are more compatible with aryl chlorides.⁴⁸ As expected, the oxidative addition rate decreases in the order I > Br > Cl. While homogeneous catalysts can achieve the high activity, there are problems associated with them such as low recoverability, high cost, and poor recyclability of the catalyst reduce the usefulness of such catalysts.^{49–51}

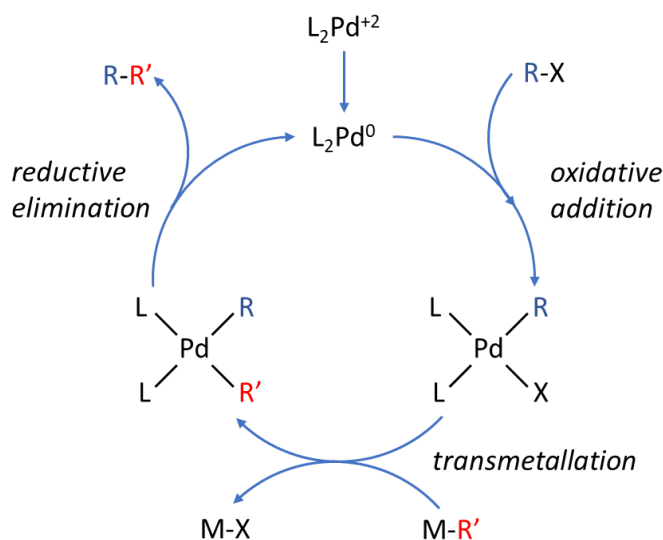


Figure 1.7 Cross-coupling catalytic cycle for Pd catalyzed reactions.

1.3.1 Heterogeneous Catalysts for Cross-coupling Reactions

To address these challenges, there has been great interest in designing cost-effective heterogeneous catalysts to allow for catalyst isolation and recycling without compromising catalytic activity.^{49–51} The study of heterogeneous catalysts dates back to the 1800s when

Faraday examined the ability of platinum to facilitate an oxidation reaction since then many other catalytic processes have been developed. Heterogeneous catalysts for Suzuki cross-coupling reactions have garnered much interest in the last few decades. They have the advantage of good recoverability, and good recyclability, which brings down the cost. One of the most pursued approaches has been the synthesis of highly dispersed and supported metal nanoparticles (NPs) featuring controlled size, morphology, and composition (Fig 1.8).¹³ By controlling these parameters and careful selection of the support, such catalysts have the potential to rival their homogeneous counterparts in terms of stability and activity.

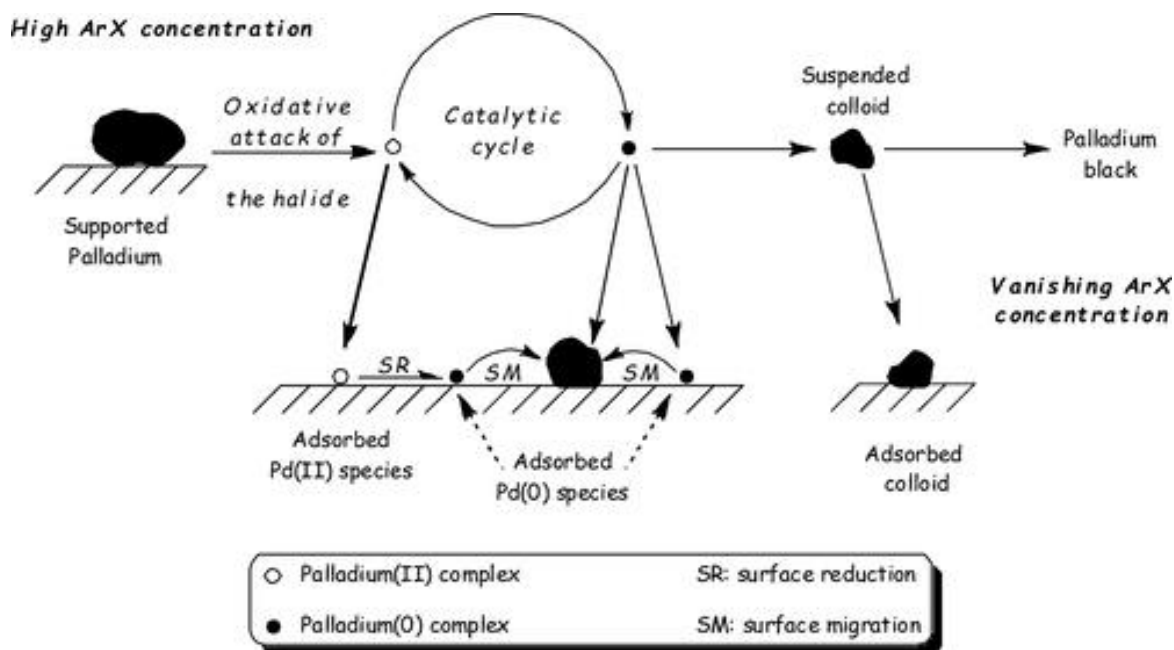


Figure 1.8 Different catalytically active species of a heterogeneous catalyst in the Suzuki cross-coupling reaction. (Copyright 2017 American Chemical Society)

1.3.2 Palladium Metal as an Active center in Cross-coupling Reactions

The use of Pd metal dates back to the origin of these reactions, with the very first use documented for Heck reaction in the 1970s.⁵²⁻⁵⁴ The first application of supported Pd metal on carbon support dates back to the 70s reported by Julia et al., in which under elevated temperatures (120 °C), applied pressure, and methanol, stilbene was obtained through a cross-coupling reaction between styrene and chlorobenzene were performed.^{55,56} Since then, the use of Pd metal in various nanosized forms with emphasis on the metal dispersity has been researched.^{57,58}

1.3.2.1 Supported Palladium for Cross-coupling Reactions

Supported Pd metal catalysts have achieved great success as stated in a few examples above, but their exact systematic mechanism of cross-coupling is still debated. It is hypothesized that molecular Pd species, may leach from the metallic Pd into the reaction solution, these species are catalytically competent hence the cross-coupling reaction proceeds through in a homogeneous reaction environment.⁵⁹⁻⁶³ In general, supported Pd metal can be introduced into the reaction media through catalytically competent species in various forms such as leached Pd species, exposed surface metal atoms, defect/edge sites, and surface PdO, emphasizing the influence of Pd metal morphology, composition and its relationship with the support. A very recent study has been able to demonstrate a heterogeneous catalysis mechanism taking place at the Pd metal surface, in specific defect/edge sites of Pd nanoparticles have found to partake in certain cross-coupling reactions.⁶⁴ To date the answer to the question, “where does the catalytic event takes place?” instill debated.⁶⁵ It is reported that catalytically competent Pd species leached into

the solution can also reprecipitate over the support, while this reprecipitation is affected by various factors such as temperature, nature of the support, and the nature of the base.^{66–68} It was observed that in a comparison between 10% Pd/C and 1% Pd/SiO₂, more precipitation occurred on the surface of carbon than of silica. The precipitation phenomena can result in larger colloidal particles and extensively restructure the nanoparticles.^{68,69} It should be noted that precipitation occurrence results were collected under elevated temperatures ranging from 80–140 °C. It has also been hypothesized that the dissolution and reformation of Pd metal induces a steady-state and it may still preserve the Pd nanoparticles and such samples remain active throughout the catalytic event. The dissolution mechanism by itself can proceed through small Pd (0) clusters⁶⁸ or surface detachment induced by the oxidative addition of aryl halide. The latter usually results in Pd(II) complexes, which further undergo an in situ reductions forming the catalytically active Pd(0) species.^{70,71}

1.3.3 Suzuki-Miyaura Reaction

Suzuki-Miyaura cross-coupling reaction, from now on termed SCC for short, is most intensively investigated cross-coupling reaction.^{72,73} Given the indispensable role of SCC reaction in organic synthesis and because of its simplicity and effectiveness, intense efforts have been directed toward the development of cost-effective heterogeneous catalysts.⁷⁴ In SCC reaction, the C–C bond is formed by coupling an organoboron reagent with an organic halide in the presence of a Pd catalyst and a base. SCC reaction offers many advantages when it is compared to other cross-coupling reactions. The availability of reagents in specific organoboron derivatives, with 1800 compounds being commercially

available, facilitates the study of SCC reactions. These compounds are known to be thermally stable and inert towards moisture and oxygen. Also, SCC reaction can utilize a wide range of functional groups.⁷⁵ Overall, SCC reaction is employed for its simplicity and cost-effectiveness and it is positioned as a benchmark for validating new catalysts.⁷⁶ The formation of a C-C bond is also among the most significant reaction due to its wide applicability. C-C cross-coupling reactions, which can also be differentiated by the hybridization state of carbon, are popular for synthesizing a wide range of functionalized substituents.^{77,78} There are few important areas identified by researchers, where improvements will have the utmost benefits such as the development of ligand-free Pd active sites, minimizing the content of Pd by achieving higher active surface to volume ratio, modifications of reaction parameters, and use of more environmentally friendly solvents. While considerable advances have been made in this area, only very few catalysts have comparable activity compared to established homogeneous catalysts.^{47,75,79,80} Thus, there is an urgent need for highly active heterogeneous catalysts for C-C cross-coupling reactions.

1.3.4 Characteristics of an Outstanding Heterogeneous Catalysts

1.3.4.1 Metal Nanoparticle Centers

The requirements for a superior catalyst are having the high activity of a ligated homogeneous catalyst with the recyclability of a heterogeneous catalyst. Employing metal nanoparticles (NPs) has emerged as a fundamental design criterion in the development of heterogeneous catalysts.⁸¹⁻⁸³ Various synthetic methodologies have enabled control over the composition, shape, and size of NPs, as well as methods for the preparation of supported

NPs. Most of those methodologies fall under the ‘bottom-up’ technique for the synthesis of NPs, where atomic-level precursors are used to synthesizing nanosized materials. Methods such as wet and dry impregnation,^{84,85} in which a required amount of metal precursor solution or freshly prepared NPs are introduced to fill the pore volume of the support. While impregnation is a simple and quick synthesis technique, it generally yields NPs with large average size, broad size distributions, and, inhomogeneous alloying, in the case of multiple metals. It has also been reported that morphology-controlled NP can be synthesized separately and deposited on the support in another step. One example of this method is the formation of monodispersed ultra-small bimetallic NPs (1.9-4.5 nm) synthesized by a one-step multiphase ethylene glycol using oleyl-amine and oleic acid as the capping ligands, where, as-synthesized NPs were later loaded on carbon support with atomic composition of bimetallic NPs, the crystallinity and electronic structure plays an important role in the catalytic activity.⁸⁶ Other methods such as microwave radiation, chemical vapor deposition (CVD), atomic layer deposition (ALD) have been used for the production of NPs.^{16,87} NPs ability to donate and accept charge effectively is of the utmost importance in their catalytic activity while the support can facilitate charge transport, catalytic activity, and also stabilize the recyclable catalyst.⁸⁸

To alleviate reaction conditions, a variety of synthetic strategies such as decreasing Pd NPs size, use of unique supports, and chemical and electronic modification of Pd NPs by other metals were targeted. Although base metals, mainly nickel, copper and iron have been reported to catalyze various steps of the cross-coupling reaction, these catalysts are deemed inferior to Pd NPs.⁸⁹⁻⁹² Very interestingly, alloying these metals with Pd affords

bimetallic nanoparticles with superior catalytic properties compared to their monometallic counterparts because of the ability of base metals to donate charge to the Pd atoms.⁹³⁻⁹⁵ Base metals increase the electron density on Pd and thus lower the activation energy of the rate-limiting step of SCC. This process not only enhances the catalytic activity of Pd catalysts but also makes them more cost-effective because the Pd content is significantly reduced. To further advance these bimetallic systems and make them viable, several issues need to be addressed; precise control over NPs size and dispersity, tunable chemical composition, and strong interaction with the support to prevent metal leaching and NPs sintering. In this regard, strong electrostatic adsorption (SEA) is uniquely suited for addressing all these desirable features.^{9,10,96} Recently, Wong et al. demonstrated the use of co-strong electrostatic adsorption (co-SEA) in the synthesis of ultra-small, highly dispersed, and well-alloyed bimetallic nanoparticles involving noble metals (Pt and Pd) and base metals (Cu, Ni, and Co). The NPs were synthesized with average particle sizes from 0.9 to 1.4 nm, with narrow size distributions using porous silica support (Fig. 1.9).⁹ In general, to achieve the highest possible metal utilization in a catalyst, all the metal atoms should be accessible in the gas or liquid phase, and it is understood that such optimization is achieved when particle size is about 1 nm.^{97,98}

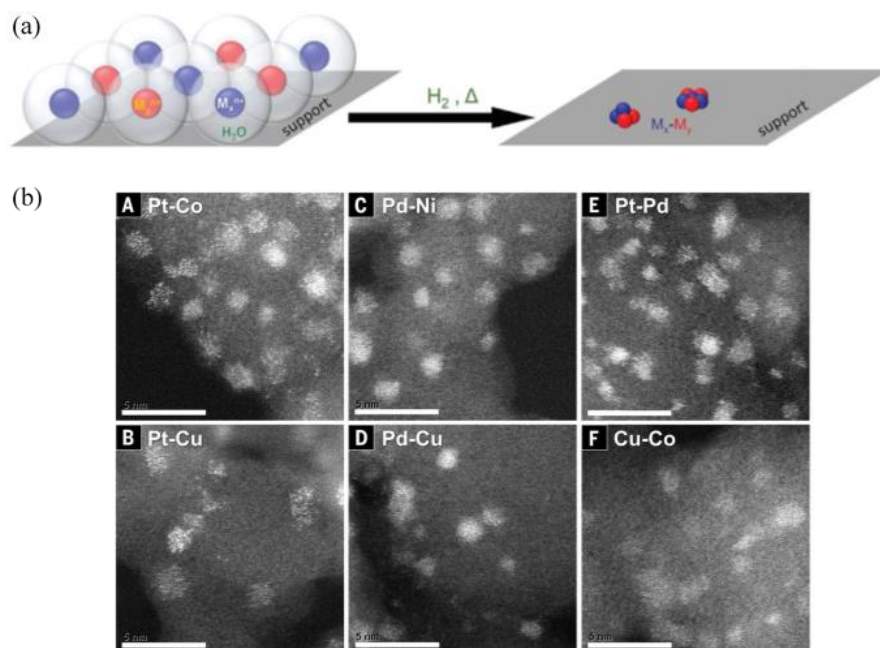


Figure 1.9 (a) Schematic of the SEA synthesis technique: Electrostatic adsorption of the mixed monolayer of charged precursors on the Silica support, and formation of the alloyed nanoparticles upon reduction with hydrogen at elevated temperatures. (b) ultrasmall bimetallic nanoparticles deposited on the surface of silica. (Copyright 2017 Science)

1.3.4.2 Catalysts Supports

Catalyst supports and their surface characterization play an important role in the immobilization and distribution of Pd nanoparticles to be used in cross-coupling reactions. Activate carbon⁹⁹, graphene oxide¹⁰⁰, functionalized graphene¹⁰¹, polymers¹⁰², metal organic frameworks¹⁰³, and silica^{104–106} are among the most investigated catalysts supports. Some support features have been proven to be more advantageous than others. It has been reported that anionic inorganic support, prevents leaching, and promotes high-yield Suzuki reaction.¹⁰⁷ Utilizing silica support has various advantages such as low-cost, tunable

porosity. Similar to other oxides, silica has unsaturated surface valences that can be saturated by the chemisorption of water, leading to the formation of covalently bonded surface hydroxyl groups (silanol).¹⁰⁸ This surface feature enables the immobilization of both the adsorbed metal complexes and the generated metal NPs.¹⁰⁹ Other surface features such as high surface area and large pore size also have been reported to be beneficial, and such features are also available in silica.¹¹⁰

In conclusion, many parameters are taken into account when it comes to synthesizing heterogeneous catalysts for SCC reactions and investigating the catalytic activity of the as synthesized catalysts. Nanoparticles which include Pd metal active centers have proven to perform the catalysis more effectively. Facile synthesis of such nanoparticles is highly demanded. Among various heterogeneous catalysts, features such as high metal active center to volume ratio seem to facilitate the SCC reaction the most. In general, it is highly desirable for catalysts to carry the lowest content of active metal while maintaining high activity. The stability of the nanoparticle also plays an important role, firstly, in understanding the catalytic mechanism as active metal centers can be more accurately identified. Especially if the stability can be correlated with minimal leaching of the Pd metal active centers. Secondly, high stability for a catalyst that has shown good catalytic performance may lead to good recyclability as well. Recyclability of the cross-coupling catalysts remains one of the main challenges that this field of research faces. Many catalyst supports have been investigated for heterogeneous catalysis, superior catalyst support can help with nanoparticle formation, size control, distribution, and stability. Some features of the support such as well distribution of surface functionality,

high surface area, and pore size are all considered to contribute to the required role of the support. Overall, achieving high catalytic activity in a mild reaction condition is only possible by tailoring the features of the catalysts to each step of the catalytic reaction, starting by the first step, which is also the rate-limiting step, oxidative reduction of the aryl halide. Beside high catalytic activity, other outcomes can attest to the superiority of a catalyst. High stability, good recyclability, and high TOF number are investigated for validation of the performance of the catalysts.

1.4 Lithium Sulfur Batteries

1.4.1 Lithium Ion and Lithium Sulfur Batteries

As energy demands continue to grow, fossil fuels have been the dominant source of energy and the consequential harmful environmental effects of consuming fossil fuel have also been growing. Transitioning from fossil fuels to renewable energy sources has gained a lot of attention. With the scientific advancements, the feasibility and utility of alternative energy sources are increasing. Many industry sectors are seeking alternative energy sources not only to minimize the negative impacts of burning fossil fuels but also for the long-term financial benefits. Among sustainable energy sources, lithium ion batteries (LIBs) have revolutionized the portable energy demanding devices, whether they are mobile phones or cars. The significance of LIBs on our lives has been recognized by Nobel academy, Dr. Goodenough, Dr. Whittingham, and Dr. Yoshino were awarded the Nobel prize in chemistry in 2019. Vast research and investment on LIBs facilitated the commercialization of these batteries, but their shortcomings such as low energy-to-weight ratios ($140\text{--}260\text{ Whkg}^{-1}$) and high production costs ($>\$300$ per kWh for battery packs)¹¹¹ has hampered their application in devices with greater energy demands such as electronic vehicles (EVs) and energy storage systems (ESSs). The most promising candidate to answer the shortcomings of LIBs are lithium-sulfur batteries (LSBs). LSBs are composed of a lithium metal anode and a sulfur cathode with a high theoretical capacity (sulfur: 1672 mAh g^{-1} , lithium metal: 3860 mAh g^{-1}).¹¹² The production cost for LSBs is projected at <125 per kWh, which is a more suitable price-to-energy ratio for EVs industry.¹¹¹

To compete with LIBs, there are few practical requirements that LSBs should have: 1) sufficient sulfur content (> 70 wt.%), 2) high areal sulfur loading (> 5 mg cm⁻¹), and 3) low electrolyte to sulfur ratios (< 4 μL mg⁻¹). LSBs have a few intrinsic challenges impeding their large-scale production, such as the poor electrical conductivities of sulfur (5×10^{-30} S cm⁻¹) and Li₂S (10^{-13} S cm⁻¹), and the large volume change between S₈ and Li₂S (180%) during charge/discharge cycle. Furthermore, the loss of active material in between battery components leads to the overall loss of activity. The loss of active materials can take place via diffusion of lithium polysulfides (LiPS) from cathode to anode resulting in poor cycle stability, also with an applied electric field, LiPS can move from anode to cathode, a phenomenon also known as shuttle effect resulting in lowering of the coulombic efficiency. The efforts to address these problems can be focused on the development of a conductive framework that is also sulfur adsorbent.¹¹³

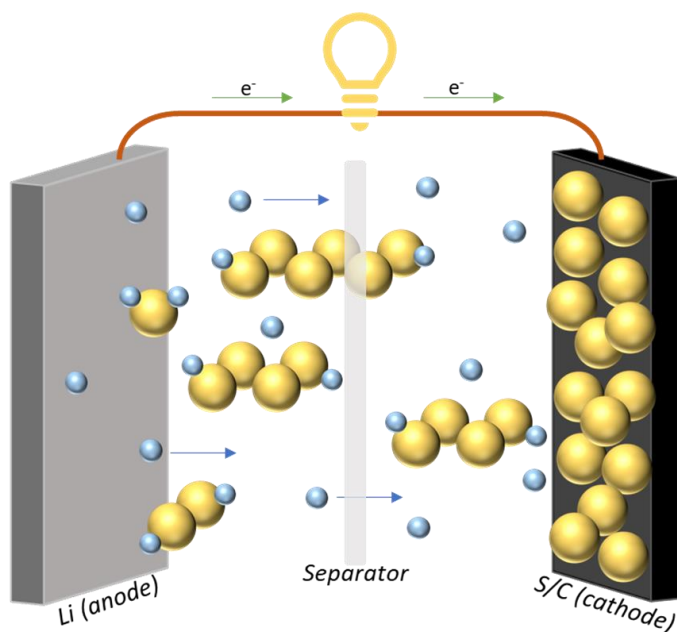


Figure 1.10 Schematic of lithium sulfur batteries.

1.4.2 Lithium-sulfur Batteries Operating Principles

Cumulatively, one S atom can react with two lithium ions (Li^+) by transferring two electrons. During discharge, sulfur in the form of S_8 is reduced to Li_2S in a stepwise manner (Fig. 1.11). Step I: the first plateau, at approximately 2.4 V, which corresponds to the two-phase reduction of solid S_8 to liquid long-chain lithium polysulfides, LiPS, (Li_2S_x , $4 < x \leq 8$). Step II: the slope corresponds to the reduction of long-chain LiPS to liquid short-chain LiPS (Li_2S_x , $2 < x \leq 4$). In this step, the transition of a high quantity of bulky sulfur results in the decrease in the reaction kinetic, and increase in the LiPS detention time, which in turn hampers the dissolution LiPS that takes place in this step. Step III: the second plateau phase at approximately 2.1 V, which corresponds to another two-phase reaction in which liquid short-chain LiPS is reduced to solid Li_2S_2 . The shuttle effect in LSBs is mainly caused by the dissolution of polysulfide in an organic liquid-based electrolyte. Step IV: the final slope in the discharge cycle, corresponds to the reduction of solid Li_2S_2 to solid Li_2S . The charge process is initiated by the phase nucleation of $\text{Li}_2\text{S}_2/\text{Li}_2\text{S}$. The charge process begins with the phase transformation of $\text{Li}_2\text{S}_2/\text{Li}_2\text{S}$ to soluble LiPS requires an overpotential to overcome the ionically/electrically insulating nature of $\text{Li}_2\text{S}_2/\text{Li}_2\text{S}$ and limited solubility in an aprotic electrolyte.¹¹⁴ This step is the major contributor to the sluggish oxidation kinetic of $\text{Li}_2\text{S}_2/\text{Li}_2\text{S}$ and low sulfur utilization.¹¹³ The single plateau step in the charge half-cycle from 2.3 to 2.4 corresponds to the reverse reaction of step I-III in which LiPS oxidize to S_8 .

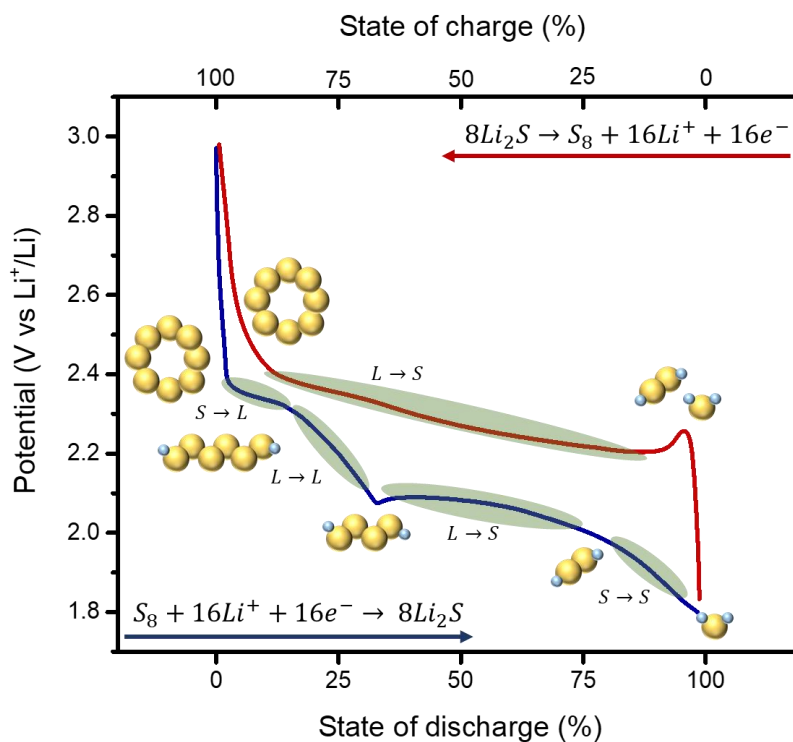


Figure 1.11 Operating principle of LSBs.

1.4.3 Optimization of Cathode for Lithium-sulfur Batteries

The electrochemical performance of the Li-S batteries can be improved mainly by the efficient reversible conversion of Li polysulfides to Li₂S during discharge, and to elemental S during charge. The efficiency of this conversion is enhanced by limiting the mobility of the soluble polysulfides.¹¹⁵ The mobility limitation is induced by bond formation between S_x²⁻ and active centers on the surface of the carbon framework. If the bonding has low free energy and decomposition energy barriers, the efficiency of the discharge cycle is increased. Also, trapping the insoluble Li₂S₂ and Li₂S by the active centers will prevent their precipitation on the surface of the Li foil. One of the pioneering

works in the advancement of LSBs cathode materials was developed by Nazar et al., in which porous carbon was used as a conductive framework and a sulfur host, they were able to demonstrate that porous carbon not only facilitates the electron transfer but also participate in the confinement of soluble LiPS.¹¹⁶ They concluded that the weak van der Waals interactions between polar LiPS and the nonpolar carbon surface do not prevent the shuttle effect during long-term stability tests.

1.4.3.1 Nitrogen-doped Carbon Cathode for LSBs

Incorporation of nitrogen in carbon framework has been shown both experimentally and through quantum-mechanical calculation with B3LYP hybrid density functional theory (Gaussian 03) indicates that carbon atoms adjacent to nitrogen dopants possess a significantly high positive charge density to counterbalance the strong electronic affinity of the nitrogen atom.²⁷ Nitrogen doping can enhance the electron-donor property of the carbon matrix because of its higher electron affinity than carbon, resulting in an improvement of the interaction between carbon and guest molecules. Experimentally the presence of structural nitrogen can be confirmed by x-ray photoelectron spectroscopic (XPS) measurements, which quantifies the various positioning of the nitrogen atom in the carbon framework. Nitrogen carrying different bonding energies, such as pyridinic-nitrogen (399 eV), pyrrolic-nitrogen (400 eV), and quaternary nitrogen (401 eV), nitrogen atoms within carbon graphitic sheets can be differentiated using XPS.^{117,118} It has been reported that incorporation of heteroatom functionalities in carbon matrix result in higher surface adsorption.¹¹⁹

1.4.3.2 Metal Nanoparticles Active Centers for Cathodes in LSBs

Transition metal NPs can act as a catalyst that adsorbs the polysulfides during the discharge process and rapidly convert them to Li_2S while catalyzing Li_2S oxidation to sulfur in the reverse process. Hence, the polysulfide redox process can be catalyzed in the battery, which mitigates the shuttle effect of LPS.

There are various synthesis methods for the formation of active centers on the surface of materials with a high specific surface area. First, active centers can be synthesized ex-situ and deposited on the surface of the support in a different step.¹⁶ Second, active centers, typically in the form of nanoparticles can be synthesized in situ on the surface of the support.^{9,85} Third, the active centers and support can be synthesized together, in this method the active center and carbon support precursors are mixed and their synthesis proceeds through chemical activation and carbonized.¹²⁰ The product of the carbonization may yield metal nanoparticles or single atoms in the carbon framework.²⁴ The adsorption of noble metal complexes onto common oxide supports is coulombic in nature.¹⁰⁹ It has been shown that non-noble metals and bimetallic alloys can be deposited on oxide and carbon supports relative to the supports point of zero charge (PZC).^{84,121} This deposition method termed strong electrostatic adsorption (SEA) yields ultra-small and highly dispersed nanoparticles. Recently Wong et al. demonstrated the use of strong electrostatic adsorption (SEA) in the synthesis of ultra-small and highly dispersed metallic nanoparticles involving base metals (copper, nickel, and cobalt). The NPs were synthesized with average particle sizes from 0.9 to 1.4 nanometers, with narrow size distributions.⁹ Incorporation of single atoms of transition metals in the doped-carbon framework is another viable approach

for creating localized centers. Ultra-small NPs and single atoms positioned on or inside the carbon framework are both capable of facilitating the Li-S redox reaction and prevent the shuttle effects and ultimately increasing the efficiency of Li-S batteries.

1.5 Thesis Statement

This thesis proposes the synthesis and development of metal nanoparticles supported on heteroatom-doped high surface area supports based on carbon and silicon for energy conversion, energy storage, and heterogeneous catalytic processes. The underlying thought process behind the development of the materials discussed here is cost-effectiveness and high efficiency. These materials can directly contribute to the development of the components that are part of the energy production and storage cycle. Fuel cells and batteries are among the highly investigated areas of research, gaining increasing attention in correspondence to increasing energy demands. As for heterogeneous catalysis, cost-effectiveness and high efficiency are also the top priorities when it comes to designing a catalyst. Facile and scalable synthesis techniques used here can fine-tune the size, composition, and dispersity of the nanoparticles that are considered the active centers that are incorporated on high surface area materials. The physical and chemical properties of the high surface area support can also be tailored, by utilizing abundant heteroatoms-doped carbon and silica to carry specific functionalities toward different applications as well as supporting the nanoparticles and maintaining their characteristics. Here, each of the contributing features on metal nanoparticles and supports is discussed for their irrespective applications.

Chapter two discusses the various instrumentation such as experimental techniques such as Brunauer–Emmett–Teller (BET) surface area measurement, thermogravimetric analysis (TGA), scanning electron microscopy (SEM), energy-dispersive X-ray spectroscopy (EDX), high-resolution transmission electron microscopy (HR-TEM), X-ray photoelectron spectroscopy (XPS), Powder X-ray diffraction (P-XRD), Raman spectrometry, and inductively coupled plasma optical emission spectrometry (ICP-OES) have been used for studying the physical and chemical characteristic of the synthesized materials.

Chapter three discusses the facile synthesis route to prepare iron phosphide doped porous carbon support as a cathode catalyst for oxygen reduction reaction (ORR) in alkaline and acidic fuel cells. The electrocatalytic performance of the synthesized catalyst is evaluated by different techniques such as cyclic voltammetry, linear sweep voltammetry, and chronoamperometric. The electrocatalytic performance of the catalyst is compared with the current commercially available catalyst which is 20 wt% Pt on carbon. Platinum is a scarce metal, with a high cost of production and great catalytic activity, used in fuel cells for the oxidation of hydrogen in anode and reduction of oxygen in the cathode. Besides the high cost of Pt, this catalyst is also prone to sluggish ORR reaction and degradation of activity over long-term and Methanol poisoning. The synthesis of a cost-effective, highly efficient catalysts composed of inexpensive and earth-abundant elements is highly sought after. In this chapter, the contribution of each component of the iron phosphide doped porous carbon such as surface area, pore size distribution, metal NPs composition dispersity toward ORR is discussed.

Chapter four, the synthesis of ultrasmall, well-alloyed bimetallic NPs are deposited on high surface area silica support through the facile synthesis technique of strong electrostatic adsorption (SEA) is reported. The synthesized catalysts are used as for Suzuki-Miyaura cross-coupling (SCC) reactions. Current catalysts used for cross-coupling reactions are categorized into two main groups, homogeneous and heterogeneous catalysts. Homogeneous catalysis has been long utilized for cross-coupling reactions for their effectiveness in achieving high activity and turnover in a wide variety of functional groups, but there are problems associated with them, such as low recoverability, high cost, and poor recyclability of the catalyst reduce the usefulness of such catalysts. On the other hand, heterogeneous catalysts suffer from low activity and turn over frequency. Here, active metal Pd and base metals (Cu, Ni, and Co) cations are deposited on the silica support vis SEA synthesis method. After reduction with 5% H₂ (in Argon) it yields homogeneously alloyed nanoparticles with an average size of 1.3 nm. All bimetallic catalysts were found to be highly active toward SCC surpassing the activity of monometallic Pd/SiO₂; the catalyst consists of Cu and Pd, CuPd/SiO₂, were able to perform the SCC with a turn over frequency of 248000.

Chapter 5, a catalytically active material consists of small Ni NPs supported on high surface area nitrogen-doped porous carbon is used as a cathode in lithium-sulfur batteries (LSB). Increasing energy demands requires batteries with high theoretical capacity and a more suitable price-to-energy ratio than the current state of the are lithium-ion batteries. LSBs have a few intrinsic challenges impeding their large-scale production, such as the poor electrical conductivities of sulfur and Li₂S, and the large volume change

between S_8 and Li_2S during the charge/discharge cycle. A phenomenon known as shuttle effect, which leads to loss of active materials and lowering the coulombic efficiency of these batteries, is another reason that hampers the large-scale production of LSBs. The transformation of carbon electrodes into a catalytic electrode has shown the capability to enhance the overall activity of LSB. Here, Ni NPs act as active centers for the adsorption of polysulfides during the discharge process and rapidly convert them to Li_2S while catalyzing Li_2S oxidation to sulfur in the reverse process. The addition of Ni NPs improves the reaction kinetics and activity retention of the Li-S coin cells.

Lastly, in chapter six, conclusions and outlook are provided and the results of each project are summarized.

References

- (1) Karfunkel, H. R.; Dressler, T. New Hypothetical Carbon Allotropes of Remarkable Stability Estimated by MNDO Solid-State SCF Computations. *J. Am. Chem. Soc.* **1992**, *114* (7), 2285–2288.
- (2) Takahashi, R.; Sato, S.; Sodesawa, T.; Kawakita, M.; Ogura, K. High Surface-Area Silica with Controlled Pore Size Prepared from Nanocomposite of Silica and Citric Acid. *J. Phys. Chem. B* **2000**, *104* (51), 12184–12191.
- (3) Zhang, L.; Zhang, F.; Yang, X.; Long, G.; Wu, Y.; Zhang, T.; Leng, K.; Huang, Y.; Ma, Y.; Yu, A.; Chen, Y. Porous 3D Graphene-Based Bulk Materials with Exceptional High Surface Area and Excellent Conductivity for Supercapacitors. *Sci. Rep.* **2013**, *3* (1), 1408.
- (4) Novoselov, K. S.; Geim, A. K.; Morozov, S. V.; Jiang, D.; Zhang, Y.; Dubonos, S. V.; Grigorieva, I. V.; Firsov, A. A. Electric Field Effect in Atomically Thin Carbon Films. *Science* **2004**, *306* (5696), 666–669.
- (5) Robertson, J. Amorphous Carbon. *Curr. Opin. Solid State Mater. Sci.* **1996**, *1* (4), 557–561.
- (6) Shen, W.; Fan, W. Nitrogen-Containing Porous Carbons: Synthesis and Application. *J. Mater. Chem. A* **2013**, *1* (4), 999–1013.
- (7) Kiciński, W.; Szala, M.; Bystrzejewski, M. Sulfur-Doped Porous Carbons: Synthesis and Applications. *Carbon N. Y.* **2014**, *68*, 1–32.
- (8) Qiang, Z.; Xia, Y.; Xia, X.; Vogt, B. D. Generalized Synthesis of a Family of Highly Heteroatom-Doped Ordered Mesoporous Carbons. *Chem. Mater.* **2017**, *29* (23), 10178–10186.
- (9) Wong, A.; Liu, Q.; Griffin, S.; Nicholls, A.; Regalbuto, J. R. Synthesis of Ultrasmall, Homogeneously Alloyed, Bimetallic Nanoparticles on Silica Supports. *Science* **2017**, *358* (6369), 1427–1430.
- (10) Ding, K.; Cullen, D. A.; Zhang, L.; Cao, Z.; Roy, A. D.; Ivanov, I. N.; Cao, D. A General Synthesis Approach for Supported Bimetallic Nanoparticles via Surface Inorganometallic Chemistry. *Science* **2018**, *362* (6414), 560–564.
- (11) Singh, K. P.; Bae, E. J.; Yu, J. S. Fe-P: A New Class of Electroactive Catalyst for Oxygen Reduction Reaction. *J. Am. Chem. Soc.* **2015**, *137* (9), 3165–3168.
- (12) Norouzi, N.; Choudhury, F.; El-Kaderi, H. M. Iron Phosphide Doped-Porous Carbon as an Efficient Electrocatalyst for Oxygen Reduction Reaction. *ACS Appl. Energy Mater.* **2020**, *3* (3), 2537–2546.
- (13) Rai, R. K.; Gupta, K.; Tyagi, D.; Mahata, A.; Behrens, S.; Yang, X.; Xu, Q.; Pathak,

- B.; Singh, S. K. Access to Highly Active Ni-Pd Bimetallic Nanoparticle Catalysts for C-C Coupling Reactions. *Catal. Sci. Technol.* **2016**, *6* (14), 5567–5579.
- (14) Gewirth, A. A.; Varnell, J. A.; Diascro, A. M. Nonprecious Metal Catalysts for Oxygen Reduction in Heterogeneous Aqueous Systems. *Chem. Rev.* **2018**, *118* (5), 2313–2339.
- (15) Noori, A.; El-Kady, M. F.; Rahmanifar, M. S.; Kaner, R. B.; Mousavi, M. F. Towards Establishing Standard Performance Metrics for Batteries, Supercapacitors and Beyond. *Chem. Soc. Rev.* **2019**, *48* (5), 1272–1341.
- (16) Gilroy, K. D.; Ruditskiy, A.; Peng, H. C.; Qin, D.; Xia, Y. Bimetallic Nanocrystals: Syntheses, Properties, and Applications. *Chem. Rev.* **2016**, *116* (18), 10414–10472.
- (17) U.S. Energy Information Administration. Annual Energy Outlook 2019 with Projection to 2050, 2019, 1–83.
- (18) Firouzjaie, H. A.; Mustain, W. E. Catalytic Advantages, Challenges, and Priorities in Alkaline Membrane Fuel Cells. *ACS Catal.* **2020**, *10* (1), 225–234.
- (19) U.S. Department of Energy. Fuel Cell Technical Team Roadmap. *Office of Energy Efficiency & Renewable Energy: Washington, DC*. 2013, pp 1–26.
- (20) Mustain, W. E. Understanding How High-Performance Anion Exchange Membrane Fuel Cells Were Achieved: Component, Interfacial, and Cell-Level Factors. *Curr. Opin. Electrochem.* **2018**, *12*, 233–239.
- (21) Zhong, H.; Fujii, K.; Nakano, Y.; Jin, F. Effect of CO₂ Bubbling into Aqueous Solutions Used for Electrochemical Reduction of CO₂ for Energy Conversion and Storage. *J. Phys. Chem. C* **2015**, *119* (1), 55–61.
- (22) Ziv, N.; Mustain, W. E.; Dekel, D. R. The Effect of Ambient Carbon Dioxide on Anion-Exchange Membrane Fuel Cells. *ChemSusChem* **2018**, *11* (7), 1136–1150.
- (23) Gerhardt, M. R.; Pant, L. M.; Weber, A. Z. Along-the-Channel Impacts of Water Management and Carbon-Dioxide Contamination in Hydroxide-Exchange-Membrane Fuel Cells: A Modeling Study. *J. Electrochem. Soc.* **2019**, *166* (7), F3180–F3192.
- (24) Ramaswamy, N.; Mukerjee, S. Fundamental Mechanistic Understanding of Electrocatalysis of Oxygen Reduction on Pt and Non-Pt Surfaces: Acid versus Alkaline Media. *Adv. Phys. Chem.* **2012**, *2012*, 1–17.
- (25) Steele, B. C. H.; Heinzl, A. Materials for Fuel-Cell Technologies. *Nature* **2001**, *414*, 345–352.
- (26) Jasinski, R. A New Fuel Cell Cathode Catalyst. *Nature* **1964**, *201* (1964), 1212–1213.
- (27) Gong, K.; Du, F.; Xia, Z.; Durstock, M.; Dai, L. Nitrogen-Doped Carbon Nanotube Arrays with High Electrolytic Activity for Oxygen Reduction. *Science* **2009**, *323* (5915), 760–764.
- (28) Oberlin, A. Carbonization and Graphitization. *Carbon N. Y.* **1984**, *22* (6), 521–541.
- (29) Lin, L.; Zhu, Q.; Xu, A. W. Noble-Metal-Free Fe-N/C Catalyst for Highly Efficient Oxygen Reduction Reaction under Both Alkaline and Acidic Conditions. *J. Am. Chem. Soc.* **2014**, *136* (31), 11027–11033.
- (30) Zheng, Y.; Jiao, Y.; Chen, J.; Liu, J.; Liang, J.; Du, A.; Zhang, W.; Zhu, Z.; Smith, S. C.; Jaroniec, M.; Lu, G. Q. (Max); Qiao, S. Z. Nanoporous Graphitic-C₃N₄@

- Carbon Metal-Free Electrocatalysts for Highly Efficient Oxygen Reduction. *J. Am. Chem. Soc.* **2011**, *133* (50), 20116–20119.
- (31) Guo, D.; Shibuya, R.; Akiba, C.; Saji, S.; Kondo, T.; Nakamura, J. Active Sites of Nitrogen-Doped Carbon Materials for Oxygen Reduction Reaction Clarified Using Model Catalysts. *Science* **2016**, *351* (6271), 361–365.
- (32) Zhang, L.; Xia, Z. Mechanisms of Oxygen Reduction Reaction on Nitrogen-Doped Graphene for Fuel Cells. *J. Phys. Chem. C* **2011**, *115* (22), 11170–11176.
- (33) Ramaswamy, N.; Tylus, U.; Jia, Q.; Mukerjee, S. Activity Descriptor Identification for Oxygen Reduction on Nonprecious Electrocatalysts: Linking Surface Science to Coordination Chemistry. *J. Am. Chem. Soc.* **2013**, *135* (41), 15443–15449.
- (34) Liu, Z. W.; Peng, F.; Wang, H. J.; Yu, H.; Zheng, W. X.; Yang, J. Phosphorus-Doped Graphite Layers with High Electrocatalytic Activity for the O₂ Reduction in an Alkaline Medium. *Angew. Chemie- Int. Ed.* **2011**, *50* (14), 3257–3261.
- (35) Wu, J.; Jin, C.; Yang, Z.; Tian, J.; Yang, R. Synthesis of Phosphorus-Doped Carbon Hollow Spheres as Efficient Metal-Free Electrocatalysts for Oxygen Reduction. *Carbon N. Y.* **2015**, *82*, 562–571.
- (36) Yang, D. S.; Bhattacharjya, D.; Inamdar, S.; Park, J.; Yu, J. S. Phosphorus-Doped Ordered Mesoporous Carbons with Different Lengths as Efficient Metal-Free Electrocatalysts for Oxygen Reduction Reaction in Alkaline Media. *J. Am. Chem. Soc.* **2012**, *134* (39), 16127–16130.
- (37) Cruz-Silva, E.; Lopez-Urias, F.; Munoz-Sandoval, E.; Sumpter, B. G.; Terrones, H.; Charlier, J. C.; Meunier, V.; Terrones, M. Phosphorus and Phosphorus-Nitrogen Doped Carbon Nanotubes for Ultrasensitive and Selective Molecular Detection. *Nanoscale* **2011**, *3* (3), 1008–1013.
- (38) Zhang, X.; Lu, Z.; Fu, Z.; Tang, Y.; Ma, D.; Yang, Z. The Mechanisms of Oxygen Reduction Reaction on Phosphorus Doped Graphene: A First-Principle Study. *J. Power Sources* **2015**, *276*, 222–229.
- (39) Lee, D. H.; Lee, W. J. J.; Lee, W. J. J.; Kim, S. O.; Kim, Y. H. Theory, Synthesis, and Oxygen Reduction Catalysis of Fe-Porphyrin-like Carbon Nanotube. *Phys. Rev. Lett.* **2011**, *106* (17), 175502.
- (40) Razmjooei, F.; Singh, K. P.; Bae, E. J.; Yu, J.-S. A New Class of Electroactive Fe- and P-Functionalized Graphene for Oxygen Reduction. *J. Mater. Chem. A* **2015**, *3* (20), 11031–11039.
- (41) Zhang, R.; Zhang, C.; Chen, W. FeP Embedded in N, P Dual-Doped Porous Carbon Nanosheets: An Efficient and Durable Bifunctional Catalyst for Oxygen Reduction and Evolution Reactions. *J. Mater. Chem. A* **2016**, *4* (48), 18723–18729.
- (42) Ye, Y.; Duan, W.; Yi, X.; Lei, Z.; Li, G.; Feng, C. Biogenic Precursor to Size-Controlled Synthesis of Fe₂P Nanoparticles in Heteroatom-Doped Graphene-like Carbons and Their Electrocatalytic Reduction of Oxygen. *J. Power Sources* **2019**, *435*, 226770.
- (43) Pei, Y.; Cheng, Y.; Chen, J.; Smith, W.; Dong, P.; Ajayan, P. M.; Ye, M.; Shen, J. Recent Developments of Transition Metal Phosphides as Catalysts in the Energy Conversion Field. *J. Mater. Chem. A* **2018**, *6* (46), 23220–23243.
- (44) Tasker, S. Z.; Standley, E. A.; Jamison, T. F. Recent Advances in Homogeneous

- Nickel Catalysis. *Nature* **2014**, *509*, 299–309.
- (45) Sperger, T.; Le, C. M.; Lautens, M.; Schoenebeck, F. Mechanistic Insights on the Pd-Catalyzed Addition of C–X Bonds across Alkynes – a Combined Experimental and Computational Study. *Chem. Sci.* **2017**, *8* (4), 2914–2922.
- (46) Alvaro, E.; Hartwig, J. F. Resting State and Elementary Steps of the Coupling of Aryl Halides with Thiols Catalyzed by Alkylbisphosphine Complexes of Palladium. *J. Am. Chem. Soc.* **2009**, *131* (22), 7858–7868.
- (47) Das, P.; Linert, W. Schiff Base-Derived Homogeneous and Heterogeneous Palladium Catalysts for the Suzuki – Miyaura Reaction. *Coord. Chem. Rev.* **2016**, *311*, 1–23.
- (48) Fu, G. C. The Development of Versatile Methods for Palladium-Catalyzed Coupling Reactions of Aryl Electrophiles through the Use of P(t-Bu)₃ and PCy₃ as Ligands. *Acc. Chem. Res.* **2008**, *41* (11), 1555–1564.
- (49) Li, Y.; Dong, Y.; Wei, Y.; Jv, J.; Chen, Y.; Ma, J.; Yao, J.; Dong, Y. Reusable Palladium N-Heterocyclic Tetracarbene for Aqueous Suzuki–Miyaura Cross-Coupling Reaction: Homogeneous Catalysis and Heterogeneous Recovery. *Organometallics* **2018**, *37* (11), 1645–1648.
- (50) Pagliaro, M.; Pandarus, V.; Ciriminna, R.; Bøland, F.; Cara, P. D.; Béland, F.; Demma Carà, P. Heterogeneous versus Homogeneous Palladium Catalysts for Cross-Coupling Reactions. *ChemCatChem* **2012**, *4*, 432.
- (51) Chen, Z.; Vorobyeva, E.; Mitchell, S.; Fako, E.; Ortuño, M. A.; López, N.; Collins, S. M.; Midgley, P. A.; Richard, S.; Vilé, G.; Pérez-Ramírez, J. A Heterogeneous Single-Atom Palladium Catalyst Surpassing Homogeneous Systems for Suzuki Coupling. *Nat. Nanotechnol.* **2018**, *13* (8), 702–707.
- (52) Mizoroki, T.; Mori, K.; Ozaki, A. Arylation of Olefin with Aryl Iodide Catalyzed by Palladium. *Bull. Chem. Soc. Jpn.* **1971**, *44* (2), 581.
- (53) Heck, R. F.; Nolley, J. P. Palladium-Catalyzed Vinylic Hydrogen Substitution Reactions with Aryl, Benzyl, and Styryl Halides. *J. Org. Chem.* **1972**, *37* (14), 2320–2322.
- (54) Mori, K.; Mizoroki, T.; Ozaki, A. Arylation of Olefin with Iodobenzene Catalyzed by Palladium. *Bull. Chem. Soc. Jpn.* **1973**, *46* (5), 1505–1508.
- (55) Julia, M.; Duteil, M. Condensation Des Halogénures Aromatiques Avec Les Oléfine Catalysées Par Le Palladium. *Bull. Soc. Chim. Fr* **1973**, 2790, 2790.
- (56) Julia, M.; Duteil, M.; Grard, C. K. E.; Kunz, E. Etude de La Condesation de Chlorures Aromatiques Aves Les Olefines Catalisee Par Le Palladium. *Bull. Soc. Chim. Fr.* **1973**, No. 9–10, 2791–2794.
- (57) Christoffel, F.; Ward, T. R. Palladium-Catalyzed Heck Cross-Coupling Reactions in Water: A Comprehensive Review. *Catal. Letters* **2018**, *148* (2), 489–511.
- (58) Pagliaro, M.; Sels, B. F. Supported Molecular Catalysts. *ChemCatChem* **2018**, *10* (8), 1663–1665.
- (59) Biffis, A.; Zecca, M.; Basato, M. Palladium Metal Catalysts in Heck C-C Coupling Reactions. *J. Mol. Catal. A Chem.* **2001**, *173* (1), 249–274.
- (60) Phan, N. T. S.; Van Der Sluys, M.; Jones, C. W. On the Nature of the Active Species in Palladium Catalyzed Mizoroki–Heck and Suzuki–Miyaura Couplings –

- Homogeneous or Heterogeneous Catalysis, A Critical Review. *Adv. Synth. Catal.* **2006**, *348* (6), 609–679.
- (61) Astruc, D. Palladium Nanoparticles as Efficient Green Homogeneous and Heterogeneous Carbon–Carbon Coupling Precatalysts: A Unifying View. *Inorg. Chem.* **2007**, *46*, 1884.
- (62) Köhler, K.; Kleist, W.; Pröckl, S. S. Genesis of Coordinatively Unsaturated Palladium Complexes Dissolved from Solid Precursors during Heck Coupling Reactions and Their Role as Catalytically Active Species. *Inorg. Chem.* **2007**, *46*, 1876.
- (63) Deraedt, C.; Astruc, D. Homeopathic” Palladium Nanoparticle Catalysis of Cross Carbon–Carbon Coupling Reactions. *Acc. Chem. Res.* **2014**, *47*, 494.
- (64) Bej, A.; Ghosh, K.; Sarkar, A.; Knight, D. W. Palladium Nanoparticles in the Catalysis of Coupling Reactions. *RSC Adv.* **2016**, *6*, 11446.
- (65) Eremin, D. B.; Ananikov, V. P. Understanding Active Species in Catalytic Transformations: From Molecular Catalysis to Nanoparticles, Leaching, “Cocktails” of Catalysts and Dynamic Systems. *Coord. Chem. Rev.* **2017**, *346*, 2.
- (66) Zhao, F.; Bhanage, B. M.; Shirai, M.; Arai, M. Heck Reactions of Iodobenzene and Methyl Acrylate with Conventional Supported Palladium Catalysts in the Presence of Organic and/or Inorganic Bases without Ligands. *Chem. - Eur. J.* **2000**, *6*, 843.
- (67) Zhao, F.; Murakami, K.; Shirai, M.; Arai, M. Recyclable Homogeneous/Heterogeneous Catalytic Systems for Heck Reaction through Reversible Transfer of Palladium Species between Solvent and Support. *J. Catal.* **2000**, *194*, 479.
- (68) Zhao, F.; Shirai, M.; Arai, M. Palladium-Catalyzed Homogeneous and Heterogeneous Heck Reactions in NMP and Water-Mixed Solvents Using Organic, Inorganic and Mixed Bases. *J. Mol. Catal. A Chem.* **2000**, *154*, 39.
- (69) Köhler, K.; Heidenreich, R. G.; Krauter, J. G. E.; Pietsch, J. Highly Active Palladium/Activated Carbon Catalysts for Heck Reactions: Correlation of Activity, Catalyst Properties, and Pd Leaching. *Chem. - Eur. J.* **2002**, *8*, 622.
- (70) Biffis, A.; Zecca, M.; Basato, M. Metallic Palladium in the Heck Reaction: Active Catalyst or Convenient Precursor? *Eur. J. Inorg. Chem.* **2001**, *2001*, 1131.
- (71) Reetz, M. T.; Westermann, E. Phosphane-Free Palladium-Catalyzed Coupling Reactions: The Decisive Role of Pd Nanoparticles. *Angew. Chem., Int. Ed.* **2000**, *39*, 165.
- (72) Suzuki, A. Cross-Coupling Reactions Of Organoboranes: An Easy Way To Construct C-C Bonds (Nobel Lecture). *Angew. Chem., Int. Ed.* **2011**, *50*, 6722.
- (73) Maluenda, I.; Navarro, O. Recent Developments in the Suzuki-Miyaura Reaction: 2010–2014. *Molecules* **2015**, *20*, 7528.
- (74) Johansson Seechurn, C. C. C.; Kitching, M. O.; Colacot, T. J.; Snieckus, V. Palladium-Catalyzed Cross-Coupling: A Historical Contextual Perspective to the 2010 Nobel Prize. *Angew. Chem., Int. Ed.* **2012**, *51*, 5062.
- (75) Hussain, I.; Capricho, J.; Yawer, M. A. Synthesis of Biaryls via Ligand-Free Suzuki–Miyaura Cross-Coupling Reactions A Review of Homogeneous and Heterogeneous Catalytic Developments.Pdf. *Adv. Synth. Catal.* **2016**, *385* (21),

- 3320–3349.
- (76) Bi, A.; Centomo, P.; Zotto, A. Del; Zecca, M.; Chimiche, S.; Padova, U.; Padova, I.; Agroalimentari, S.; Sezone, A.; Udine, U.; et al. Pd Metal Catalysts for Cross-Couplings and Related Reactions in the 21st Century: A Critical Review. *Chem. Rev.* **2018**, *118* (4), 2249–2295.
- (77) Varun, B. V.; Dhineshkumar, J.; Bettadapur, K. R.; Siddaraju, Y.; Alagiri, K.; Ramaiah, K. Recent Advancements in Dehydrogenative Cross Coupling Reactions for C-C Bond Formation. *Tetrahedron Lett.* **2017**, *58* (9), 803–824.
- (78) Rai, R. K.; Tyagi, D.; Gupta, K.; Singh, S. K. Activated Nanostructured Bimetallic Catalysts for C-C Coupling Reactions: Recent Progress. *Catal. Sci. Technol.* **2016**, *6* (10), 3341–3361.
- (79) Lamei, K.; Eshghi, H.; Bakavoli, M.; Rounaghi, S. A.; Esmaeili, E. Carbon Coated Copper Nanostructures as a Green and Ligand Free Nanocatalyst for Suzuki Cross-Coupling Reaction. *Catal. Commun.* **2017**, *92*, 40–45.
- (80) Yang, J.; Wu, Y.; Wu, X.; Liu, W.; Wang, Y.; Wang, J. An N-Heterocyclic Carbene-Functionalised Covalent Organic Framework with Atomically Dispersed Palladium for Coupling Reactions under Mild Conditions. *Green Chem.* **2019**, *21* (19), 5267–5273.
- (81) Trzeciak, A. M.; Augustyniak, A. W. The Role of Palladium Nanoparticles in Catalytic C–C Cross-Coupling Reactions. *Coord. Chem. Rev.* **2019**, *384*, 1–20.
- (82) Rafiee, F.; Khavari, P.; Payami, Z.; Ansari, N. Palladium Nanoparticles Immobilized on the Magnetic Few Layer Graphene Support as a Highly Efficient Catalyst for Ligand Free Suzuki Cross Coupling and Homo Coupling Reactions. *J. Organomet. Chem.* **2019**, *883*, 78–85.
- (83) Bao, G.; Bai, J.; Li, C.; Yu, D. Carbon Nanofibers Supported Ultra-Small Palladium Oxide Nanoclusters as an Efficient and Continuable Catalyst for Suzuki Coupling Reaction. *Catal. Letters* **2018**, *148* (11), 3389–3401.
- (84) Spieker, W. A.; Regalbuto, J. R. A Fundamental Model of Platinum Impregnation onto Alumina. *Chem. Eng. Sci.* **2001**, *56* (11), 3491–3504.
- (85) Cho, H. R.; Regalbuto, J. R. The Rational Synthesis of Pt-Pd Bimetallic Catalysts by Electrostatic Adsorption. *Catal. Today* **2015**, *246*, 143–153.
- (86) Yin, Z.; Zhou, W.; Gao, Y.; Ma, D.; Kiely, C. J.; Bao, X. Supported Pd-Cu Bimetallic Nanoparticles That Have High Activity for the Electrochemical Oxidation of Methanol. *Chem. - A Eur. J.* **2012**, *18* (16), 4887–4893.
- (87) Lu, J.; Low, K. Bin; Lei, Y.; Libera, J. A.; Nicholls, A.; Stair, P. C.; Elam, J. W. Toward Atomically-Precise Synthesis of Supported Bimetallic Nanoparticles Using Atomic Layer Deposition. *Nat. Commun.* **2014**, *5*, 1–9.
- (88) Yang, Y.; Castano, C. E.; Gupton, B. F.; Reber, A. C.; Khanna, S. N. A Fundamental Analysis of Enhanced Cross-Coupling Catalytic Activity for Palladium Clusters on Graphene Supports. *Nanoscale* **2016**, *8* (47), 19564–19572.
- (89) Handa, S.; Jin, B.; Bora, P. P.; Wang, Y.; Zhang, X.; Gallou, F.; Reilly, J.; Lipshutz, B. H. Sonogashira Couplings Catalyzed by Fe Nanoparticles Containing Ppm Levels of Reusable Pd, under Mild Aqueous Micellar Conditions. *ACS Catal.* **2019**, *9* (3), 2423–2431.

- (90) Pan, K.; Ming, H.; Yu, H.; Huang, H.; Liu, Y.; Kang, Z. Copper Nanoparticles Modified Silicon Nanowires with Enhanced Cross-Coupling Catalytic Ability. *Dalt. Trans.* **2012**, 41 (9), 2564–2566.
- (91) Malapit, C. A.; Bour, J. R.; Brigham, C. E.; Sanford, M. S. Base-Free Nickel-Catalysed Decarbonylative Suzuki–Miyaura Coupling of Acid Fluorides. *Nature* **2018**, 563 (7729), 100–104.
- (92) Jiao, L.; Regalbuto, J. R. The Synthesis of Highly Dispersed Noble and Base Metals on Silica via Strong Electrostatic Adsorption: I. Amorphous Silica. *J. Catal.* **2008**, 260 (2), 329–341.
- (93) Yang, Y.; Reber, A. C.; Gilliland, S. E.; Castano, C. E.; Gupton, B. F.; Khanna, S. N. Donor/Acceptor Concepts for Developing Efficient Suzuki Cross-Coupling Catalysts Using Graphene-Supported Ni, Cu, Fe, Pd, and Bimetallic Pd/Ni Clusters. *J. Phys. Chem. C* **2018**, 122 (44), 25396–25403.
- (94) Smith, S. E.; Siamaki, A. R.; Gupton, B. F.; Carpenter, E. E. CuPd Nanoparticles as a Catalyst in Carbon–Carbon Cross-Coupling Reactions by a Facile Oleylamine Synthesis. *RSC Adv.* **2016**, 6 (94), 91541–91545.
- (95) Rai, R. K.; Gupta, K.; Behrens, S.; Li, J.; Xu, Q.; Singh, S. K. Highly Active Bimetallic Nickel–Palladium Alloy Nanoparticle Catalyzed Suzuki–Miyaura Reactions. *ChemCatChem* **2015**, 7 (12), 1806–1812.
- (96) Schreier, M.; Regalbuto, J. R. A Fundamental Study of Pt Tetraammine Impregnation of Silica: 1. The Electrostatic Nature of Platinum Adsorption. *J. Catal.* **2004**, 225 (1), 190–202.
- (97) Zhou, B.; Hermans, S.; Somorjai, G. A. *Nanotechnology in Catalysis*; New York: Kluwer Academic/Plenum Publishers: New York, 2004.
- (98) Regalbuto, J. R. (John R. *Handbook of Catalyst Preparation*; 2007.
- (99) Kurokhtina, A. A.; Larina, E. V.; Schmidt, A. F.; Malaika, A.; Krzyżyńska, B.; Rechnia, P.; Kozłowski, M. Mechanistic Studies of the Suzuki–Miyaura Reaction with Aryl Bromides Using Pd Supported on Micro- and Mesoporous Activated Carbons. *J. Mol. Catal. A Chem.* **2013**, 379, 327.
- (100) Diyarbakir, S.; Can, H.; Metin, Ö. Reduced Graphene Oxide-Supported Cupd Alloy Nanoparticles as Efficient Catalysts for the Sonogashira Cross-Coupling Reactions. *ACS Appl. Mater. Interfaces* **2015**, 7 (5), 3199–3206.
- (101) Fareghi-Alamdari, R.; Haqiqi, M. G.; Zekri, N. Immobilized Pd(0) Nanoparticles on Phosphine-Functionalized Graphene as a Highly Active Catalyst for Heck, Suzuki and N -Arylation Reactions. *New J. Chem.* **2016**, 40, 1287.
- (102) Yamada, Y. M. A.; Sarkar, S. M.; Uozumi, Y. Self-Assembled Poly(Imidazole-Palladium): Highly Active, Reusable Catalyst at Parts per Million to Parts per Billion Levels. *J. Am. Chem. Soc.* **2012**, 134, 3190.
- (103) Yuan, B.; Pan, Y.; Li, Y.; Yin, B.; Jiang, H. A Highly Active Heterogeneous Palladium Catalyst for the Suzuki–Miyaura and Ullmann Coupling Reactions of Aryl Chlorides in Aqueous Media. *Angew. Chemie - Int. Ed.* **2010**, 49 (24), 4054–4058.
- (104) Jana, S.; Dutta, B.; Bera, R.; Koner, S. Immobilization of Palladium in Mesoporous Silica Matrix: Preparation, Characterization, and Its Catalytic Efficacy in Carbon–

- Carbon Coupling Reactions. *Inorg. Chem.* **2008**, *47*, 5512.
- (105) Wan, Y.; Wang, H.; Zhao, Q.; Klingstedt, M.; Terasaki, O.; Zhao, D. Ordered Mesoporous Pd/Silica–Carbon as a Highly Active Heterogeneous Catalyst for Coupling Reaction of Chlorobenzene in Aqueous Media. *J. Am. Chem. Soc.* **2009**, *131*, 4541.
- (106) Soled, B. S. Silica-Supported Catalysts Get a New Breath of Life. *Science* **2015**, *350* (6265), 1171–1172.
- (107) Choudary, B. M.; Madhi, S.; Chowdari, N. S.; Kantam, M. L.; Sreedhar, B. Layered Double Hydroxide Supported Nanopalladium Catalyst for Heck-, Suzuki-, Sonogashira-, and Stille-Type Coupling Reactions of Chloroarenes. *J. Am. Chem. Soc.* **2002**, *124* (47), 14127.
- (108) Zhuravlev, L. T. Concentration of Hydroxyl Groups on the Surface of Amorphous Silicas. *Langmuir* **1987**, *3* (3), 316–318.
- (109) Brunelle, J. P. Preparation of Catalysts by Metallic Complex Adsorption on Mineral Oxides. *Pure Appl. Chem.* **1978**, *50* (9–10), 1211–1229.
- (110) Dhankhar, A.; Rai, R. K.; Tyagi, D.; Yao, X.; Singh, S. K. Synergistic Catalysis with MIL-101: Stabilized Highly Active Bimetallic NiPd and CuPd Alloy Nanoparticle Catalysts for C – C Coupling Reactions. *Chem. Sel.* **2016**, *1* (12), 3223–3227.
- (111) Ding, Y.; Cano, Z. P.; Yu, A.; Lu, J.; Chen, Z. Automotive Li-Ion Batteries: Current Status and Future Perspectives. *Electrochem. Energy Rev.* **2019**, *2* (1), 1–28.
- (112) Yin, Y. X.; Xin, S.; Guo, Y. G.; Wan, L. J. Lithium-Sulfur Batteries: Electrochemistry, Materials, and Prospects. *Angew. Chemie - Int. Ed.* **2013**, *52* (50), 13186–13200.
- (113) Lim, W. G.; Kim, S.; Jo, C.; Lee, J. A Comprehensive Review of Materials with Catalytic Effects in Li–S Batteries: Enhanced Redox Kinetics. *Angew. Chemie - Int. Ed.* **2019**, *58* (52), 18746–18757.
- (114) Waluś, S.; Barchasz, C.; Bouchet, R.; Martin, J.-F.; Leprêtre, J.-C.; Alloin, F. Non-Woven Carbon Paper as Current Collector for Li-Ion/Li₂S System: Understanding of the First Charge Mechanism. *Electrochim. Acta* **2015**, *180*, 178–186.
- (115) Shaibani, M.; Mirshekarloo, M. S.; Singh, R.; Easton, C. D.; Cooray, M. C. D.; Eshraghi, N.; Abendroth, T.; Dörfler, S.; Althues, H.; Kaskel, S.; Hollenkamp, A. F.; Hill, M. R.; Majumder, M. Expansion-Tolerant Architectures for Stable Cycling of Ultrahigh-Loading Sulfur Cathodes in Lithium-Sulfur Batteries. *Sci. Adv.* **2020**, *6* (1), 1–11.
- (116) Ji, X.; Lee, K. T.; Nazar, L. F. A Highly Ordered Nanostructured Carbon-Sulphur Cathode for Lithium-Sulphur Batteries. *Nat. Mater.* **2009**, *8* (6), 500–506.
- (117) Abdelmoaty, Y. H.; Tessema, T.-D. D.; Norouzi, N.; El-Kadri, O. M.; Turner, J. B. M. G. M.; El-Kaderi, H. M. Effective Approach for Increasing the Heteroatom Doping Levels of Porous Carbons for Superior CO₂ Capture and Separation Performance. *ACS Appl. Mater. Interfaces* **2017**, *9* (41), 35802–35810.
- (118) Ashourirad, B.; Arab, P.; Islamoglu, T.; Cychosz, K. A.; Thommes, M.; El-Kaderi, H. M. A Cost-Effective Synthesis of Heteroatom-Doped Porous Carbons as Efficient CO₂ Sorbents. *J. Mater. Chem. A* **2016**, *4* (38), 14693–14702.

- (119) Jia, Y. F.; Xiao, B.; Thomas, K. M. Adsorption of Metal Ions on Nitrogen Surface Functional Groups in Activated Carbons. *Langmuir* **2002**, *18* (2), 470–478.
- (120) Zhang, L.; Liu, D.; Muhammad, Z.; Wan, F.; Xie, W.; Wang, Y.; Song, L.; Niu, Z.; Chen, J. Single Nickel Atoms on Nitrogen-Doped Graphene Enabling Enhanced Kinetics of Lithium–Sulfur Batteries. *Advanced Materials*. 2019, p 1903955.
- (121) Santhanam, N.; Conforti, T. A.; Spieker, W.; Regalbuto, J. R. Nature of Metal Catalyst Precursors Adsorbed onto Oxide Supports. *Catalysis today*. Amsterdam 1994, pp 141–156.

Chapter 2

Characterization Techniques and Instrumentations

2.1 Introduction

In this chapter, we discuss different instrumentation and characterization techniques used for investigating the physical and chemical properties of the synthesized materials. Characterizations techniques such as surface area measurement and Inductively coupled plasma (ICP) measure the bulk properties of the samples, whereas, X-ray diffraction (XRD), Raman spectroscopy, X-ray photoelectron spectroscopy (XPS), scanning electron microscopy (SEM), and high Resolution Transmission Electron Microscopy (HR-TEM), are surface analysis technique, each having their merit.

Various electrochemical techniques are used for the study of the synthesized electrodes. Here, the preparation of the catalyst for oxygen reduction reaction (ORR) and the instrumentation used for studying the electrochemical activity of the catalysts is discussed. The preparation of electrode used as a cathode for lithium-sulfur batteries and assembly of coin cells is discussed. For the study of cross-coupling reactions, instrumentations used to investigate the catalytic activity are introduced and reaction conditions are discussed.

2.2 Characterization techniques

Textural properties of the samples were investigated using nitrogen adsorption/desorption isotherms collected by Quantachrome Autosorb-iQ at 77 K based on the Brunauer–Emmett–Teller (BET) equation (Eq. 2.1) where n is the specific amount adsorbed at the relative pressure p/p_0 , n_m is the specific monolayer capacity and C is exponentially related to the energy of monolayer adsorption.¹

$$\frac{p/p_0}{n(1-\frac{p}{p_0})} = \frac{1}{n_m C} + \frac{C-1}{n_m C} \left(\frac{p}{p_0}\right) \quad (2.1)$$

Pore size distribution (PSD) analysis based on the N₂ isotherm was investigated via a nonlocal density functional theory (NLDFT) model or quenched solid density functional theory (QSDFT), model. The ratio of the micropore volume to the total pore volume (V_{mic}/V_{total}) was calculated from the cumulative pore volume branch of PSD curves.

X-ray diffraction (XRD) is one of the fundamental characterization techniques and is the foundation of solid-state science and our understating of chemical bonding. For many materials that are not in the single-crystal state or are composed of polycrystalline materials powder X-ray diffraction (P-XRD) is used. In P-XRD, x-ray photons are scattered by the atoms in the lattice. Here, patterns collected at room temperature using a Panalytical X'Pert Pro Multipurpose Diffractometer (MPD). The samples were mounted on a zero-background sample holder measured in transmission mode using Cu K α radiation (operated at 40 kV, 45 mA; $\lambda=0.15418$ nm), the diffraction angle ranging from 10° to 70° with a step size of 0.02° and a rate of 1.2° min⁻¹. Lattice spacing can be calculated by x-ray are diffracted by crystal planes using Bragg's law (Eq. 2.2) in which where n is an integer called the order of reflection, λ is the wavelength of x-rays, d is the characteristic spacing

between the crystal planes of a given specimen and θ is the angle between the incident beam and the normal to the reflecting lattice plane. In the presence of adequate long-range order, clear and very narrow diffraction peaks are formed. Using the line width and via Scherrer equation, crystallite sizes can be calculated (Eq. 2.3), where Scherrer constant k is 0.9, λ is 0.15418 nm.²

$$n\lambda = 2d\sin\theta \quad (2.2)$$

$$B(2\theta) = \frac{k\lambda}{L \cos \theta} \quad (2.3)$$

Raman spectroscopy is a qualitative and quantitative characterization technique, in which functional group interactions, chain orientation, structural defects, and interfacial properties are studied.³ Raman spectroscopy was performed using a Thermo Scientific DXR Smart Raman spectrometer with a 523 nm excitation laser at a power of around 1 mW. For high specific surface area materials such as porous carbon, two distinct peaks are identified, a peak at $\sim 1341 \text{ cm}^{-1}$ corresponds to the D band associated with the vibrational mode of the defects and the edges of the carbon structure and the second peak at $\sim 1595 \text{ cm}^{-1}$ corresponds to sp^2 -hybridized carbon vibration known as the G band was observed. Ratio I_D/I_G was used to measure the level of disorder in the high surface area porous carbon materials.

X-ray photoelectron spectroscopy (XPS) is a characterization technique that determines the kinetic energy spectrum of photoelectrons ejected from the surface of the sample by the irradiating X-ray having a constant energy $h\nu$. The equation between $h\nu$ and E_K is shown in equation 2.4, where E_B is the binding energy of the electron to the nucleus relative to the Fermi level and ϕ a work function of the sample. The value of E_B and

chemical shift (difference from the elemental state) are utilized for identification of an element and estimation of its chemical bonding state in the sample.⁴ XPS analysis was performed on a Thermo Fisher Scientific ESCALAB 250 spectrometer employing an Al K α (1486.68 eV) X-ray source equipped with a hemispherical analyzer and XR5 Gun 500 μm (15 kV). Samples for XPS measurements were prepared by pressing the carbon specimen into a piece of indium foil, which was then mounted onto the sample holder using double-sided tape. During XPS analysis, the combination of a low-energy electron flood gun and an argon ion flood gun was utilized for charge compensation. The binding energy scale was calibrated by setting the C 1s peak at 284.8 eV or Si 2p at 103.5 eV. The XPS results were analyzed with the CasaXPS software (v4.84).

$$h\nu = E_K + E_B + \phi \quad (2.4)$$

Inductively coupled plasma – optical emission spectrometry (ICP-OES) is used for measuring the bulk composition of the metal in the samples studied here. Digestion of carbonaceous material was performed in aqua regia solution at 60 °C for at least 24 h. For each ICP-OES measurement, 4-5 standard solution and a black solution were prepared. In here, Varian Vista-MPX instrument with Ar⁺-ion plasma gas equipped with a charge-coupled detector (CCD) for simultaneous detection was used for ICP-OES measurements.

Scanning electron microscopy (SEM) utilizes a high-energy electron beam, in which the beam is scanned over the surface, and the backscattering of the electrons is observed as images. SEM was obtained using a Hitachi SU-70 scanning electron microscope. Samples were prepared by placing each specimen onto the surface of a sticky carbon tape attached to a flat aluminum sample holder. Then the samples were sputter-

coated with platinum at a pressure of 10^{-5} mbar in an N_2 atmosphere for 60 s before SEM imaging. Elemental mapping was obtained using energy-dispersive X-ray spectroscopy (EDX) attached to the SEM.

High Resolution Transmission Electron Microscopy (HR-TEM) is used for structural characterization of samples, TEM is unique in identifying and quantifying the chemical and electronic structures of individual nanocrystals. HR-TEM was performed using an FEI Titan 300 kV equipped with a Gatan 794 Multi-Scan Camera, a HAADF-STEM detector. Samples were drop-casted on carbon-coated grids (Ted Pella, Inc.) and left to dry overnight at room temperature. Captured images were processed using ImageJ software.

Gas chromatography - flame ionization detector (GC-FID) has been used to analyze the cross-coupling reactants and products of chapter 4. An Agilent 6890N GC equipped with an Agilent J&W GC HP-5MS capillary column was used in conjunction with an FID detector. An aliquot from the reaction (0.1 mL) is taken and transferred into a microfuge and ethyl acetate (0.4 mL) is added to the reaction aliquot. The mixture is centrifuged and the cross-coupling product which only dissolves in ethyl acetate is separated from the mixture. 4 μ l of the ethyl acetate layer is injected with a microsyringe in the GC-FID. From the chromatograph, the conversion of the cross-coupling product percentage and the reaction progression is calculated.

2.3 Oxygen Reduction Reaction

2.3.1 Electrochemical Measurements Instrumentation

The electrocatalytic activity for oxygen reduction reaction (ORR) was studied using a rotating ring-disk electrode (RRDE; glassy carbon disk and Pt ring) technique and rotating disk electrode (RDE; glassy carbon disk) connected to a modulated speed rotator (Pine Research) and CHI 600E potentiostat. Doped-carbon samples were deposited on a glassy carbon as the working electrode, graphite rod (6 mm diameter) as the counter electrode, and Ag/AgCl (3 M KCl) as the reference electrode were used (Fig. 2.1). The use of a graphite rod as a counter electrode is highly encouraged; it has been reported that Pt can dissolve from the counter electrode and deposit on the working electrode, resulting in an inaccurate electrochemical activity.⁵ All electrochemical measurements, including cyclic voltammograms (CVs), RRDE and RDE voltammograms, and chronoamperometry, were performed at room temperature using the mentioned three-electrode system in 0.1 M KOH solution for alkaline and 0.5 M H₂SO₄ for acidic half cells, which was purged with high-purity nitrogen or oxygen for at least 30 min before each measurement. To obtain stable CVs, the catalysts were cycled for 40 cycles between 0.2 and 1.2 V (vs RHE) in N₂ saturated solution. CVs were collected at a scan rate of 50 mV s⁻¹ and linear sweep voltammetry (LSV) at a scan rate of 10 mV s⁻¹. Ahead of each measurement, the working electrode was kept at the starting potential for 4 s. LSVs were corrected for the double-layer capacity by subtracting the LSV obtained in the N₂-saturated solution. The disk currents are normalized on the geometric area of the glassy carbon.

In the RRDE, the collection efficiency of the disk was measured to be $N=0.38$, the calculation for collection efficiency is discussed in section 2.2.2.1, during the RRDE measurement, the ring current is kept at 1.2 V vs RHE to oxidize the formed H_2O^- . The yield of H_2O^- (%) and the electron transfer number (n) can be calculated with equations 2.5 and 2.6, where i_D and i_R are the disk currents and ring currents, respectively.

$$H_2O^-(\%) = 200 \left(\frac{\frac{i_R}{N}}{\frac{i_R}{N} + i_D} \right) \quad (2.5)$$

$$n = 4 \left(\frac{i_D}{\frac{i_R}{N} + i_D} \right) \quad (2.6)$$

Tafel plots are reported using the following equation 2.7, with the kinetic current which is calculated from the mass transport correction of LSV and in which J , J_L , and J_K are the measured current density, diffusion limiting current density, and kinetic current density, respectively.

$$J_K = \frac{J \times J_L}{(J_L - J)} \quad (2.7)$$

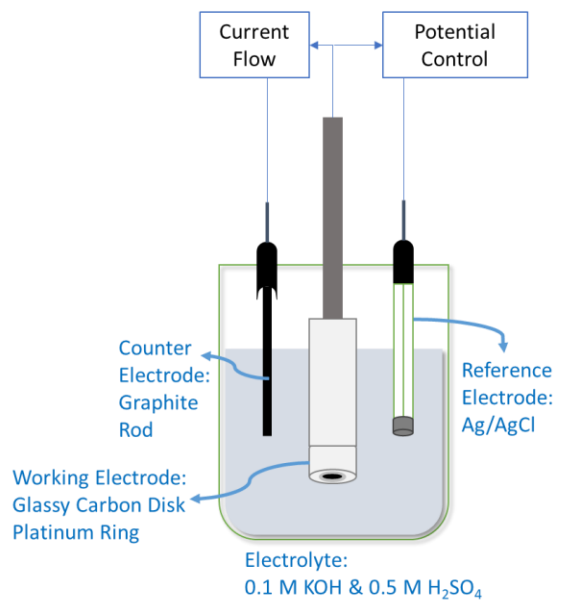


Figure 2.1 Schematic of an alkaline and acidic half-cell electrochemistry setup.

2.3.1.1 Rotating ring disk electrode

The idea of adding a ring around the disk electrode came soon after the development of a rotating ring disk electrode.⁶ In a rotating ring disk electrode (RRDE) the axial flow brings molecules and ions to the disk electrode, reduction takes place on the surface of the catalyst and the outward radial flow carries a fraction of these molecules and ions and the product generated via reduction reaction away from the disk and they will be detected brush past the surface of the ring electrode. One of the parameters in the ring disk electrode experiment is the collection efficiency (N), which is a fraction of the material from the disk that shortly later flows past the ring electrode, and can be expressed as a fraction of a percentage. The other parameter is the transit time, which is the indication of the average time required for material at the disk electrode to travel across the gap between the disk and the ring electrode. Transit time is a function of both the gap distance and rotation rate.

Collection efficiency can be collected through a series of redox reactions. The reference redox reaction typically used is the ferrocyanide/ferricyanide couple which is a simple, single-electron, reversible half-reaction. A small concentration (~10 mM) of potassium ferricyanide, $\text{K}_3\text{Fe}(\text{CN})_6$, in a suitable aqueous electrolyte solution (such as 1.0 M potassium nitrate, KNO_3) is used. The collection efficiency is determined by running RRDE at different rotation rates (400-2500 RPM) initially held at the sufficiently positive potential so no reaction will occur, then the potential is reduced toward the more negative

potentials so that the cathodic current corresponding to the reduction of ferricyanide to ferrocyanide at the disk is observed. (Eq. 2.8)



The ferrocyanide generated by the reduction reaction is carried toward the ring electrode by the means of radial flow. The ring electrode is held constant at a positive (oxidizing) potential throughout the experiment. A small amount of ferrocyanide gets oxidized (Eq. 2.9) at the ring, so the corresponding anodic current is observed at the ring.



The measured ratio of the anodic limiting current to (ring electrode) to cathodic limiting current (disk electrode) is the collection efficiency. Similar Polarization curves as the rotation rate increase from 400 RPM to 2500 RPM the limiting current of both ring and disk will increase as well. Both limiting currents are linearly proportional to the square root of the rotation rate, making collection efficiency independent of the rotation rate so, it's established empirically and can be treated as a property of that particular RRDE (Eq. 2.10).

$$N_{empirical} = \frac{-i_{limiting\ ring\ current}}{i_{limiting\ disk\ current}} \quad (2.10)$$

Once the collection efficiency is calculated, during the RRDE measurement, the ring current is kept at 1.2 V (vs RHE) to oxidize the formed H_2O_2 .⁷ The yield of hydrogen peroxide (H_2O_2 (%)) and the transfer electron number (n) can be calculated with Equations 2.11 and 2.12, where i_D and i_R are the disk currents and ring currents respectively.

$$H_2O_2(\%) = 200 \left(\frac{i_R}{\frac{i_R}{N} + i_D} \right) \quad (2.11)$$

$$n = 4 \frac{i_D}{\left(\frac{i_R}{N} + i_D \right)} \quad (2.12)$$

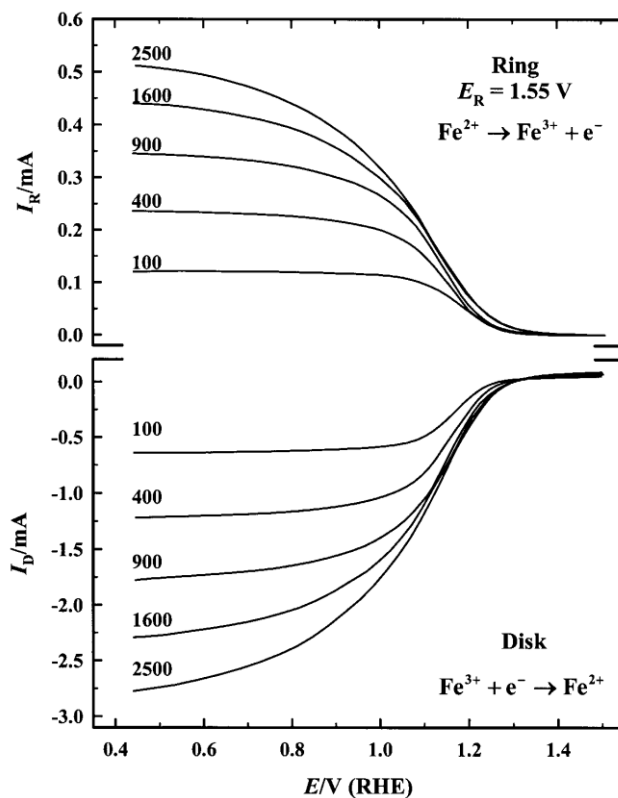


Figure 2.2 Ring and disk currents at 60°C for the determination of the collection efficiency on a Pt/C thin-film RRDE in 0.1 M NaOH supporting electrolyte with 10 mM $K_3Fe(CN)_6$. Positive sweeps at 20 $mV s^{-1}$; $E_{Ring}=1.55 V$. (Copyright 2001 Journal of the Electrochemical Chemistry)

2.3.2 Catalyst Preparation

The catalyst inks for electrochemical measurements were prepared by taking 12 mg of the PFeC and PC samples and ultrasonicated them for 30 minutes in a mixture of 0.9 mL of ethanol solution and Nafion solution binder (50 μL , 5wt. % in aliphatic alcohols, Aldrich). Catalyst solution (6 μL) was cast onto the glassy carbon working electrode via controlled drops. The RRDE and RDE have areas of 0.237 cm^2 and 0.196 cm^2 , yielding loadings of 320 $\mu\text{g cm}^{-2}$ and 387 $\mu\text{g cm}^{-2}$, respectively. Following solvent evaporation, a thin layer of catalyst is left deposited on the surface of the working electrode. Commercially available 20 wt% Pt/C catalyst was prepared similarly to the other catalysts, while only 3 μL is drop casted on the glassy carbon achieving 20 $\mu\text{g}_{\text{Pt}} \text{cm}^{-2}$ loading.

2.4 Lithium-sulfur Batteries

2.4.1 Electrode and coin cell Preparation

For the preparation of the electrode, a slurry containing an active material, carbon black additives, and polyvinylidene fluoride (PVDF) binder were combined at a weight ratio of 8:1:1. Initially, PVDF pellets were dissolved in N-methyl-2-pyrrolidinone (NMP) being used as a solvent to form a homogeneous solution, by heating it at 60 $^{\circ}\text{C}$. The mixtures were then pasted onto battery-grade aluminum foil current collectors utilizing a doctor blading technique. The paste was dried under vacuum at 50 $^{\circ}\text{C}$ overnight to remove all solvents and moisture. The resulting foil was rolled, pressed, and cut into 13 mm diameter discs. Lithium foil was used as the anode, and Celgard 2400 was employed as the separator. The electrolyte was 1M LiTFSI (lithium bis trifluoromethane sulfonyl imide) in DME/DOL (v/v = 1:1) containing 0.5 M LiNO₃. The assembly of all Li-S coin cells were

carried out inside an argon-filled glovebox (Mbraun UNIlab 2000 Plus Glove Box) with \leq 1 ppm concentration for both H₂O and O₂. The cathode disc was placed on the bottom cap of the coin cell, and the electrolyte was pipetted on the cathode at 1 mg of active materials to 30 μ L of the electrolyte ratio. Two layers of the separator were placed on top of the cathode, separators were soaked in the electrolyte before being used. The lithium was cut into 13 mm disks and gently rolled to obtain a shiny surface, then placed on top of the separator with the shiny side facing the cathode. A spacer and a spring were placed on top of the lithium disk to create a space between the top cap and bottom cap and to take the load off of the cell component respectively. Finally, the top cap was placed and the components of the coin cell were pressed together (Fig. 2.3). The cell rested overnight inside the glove box before conducting any electrochemistry measurements.

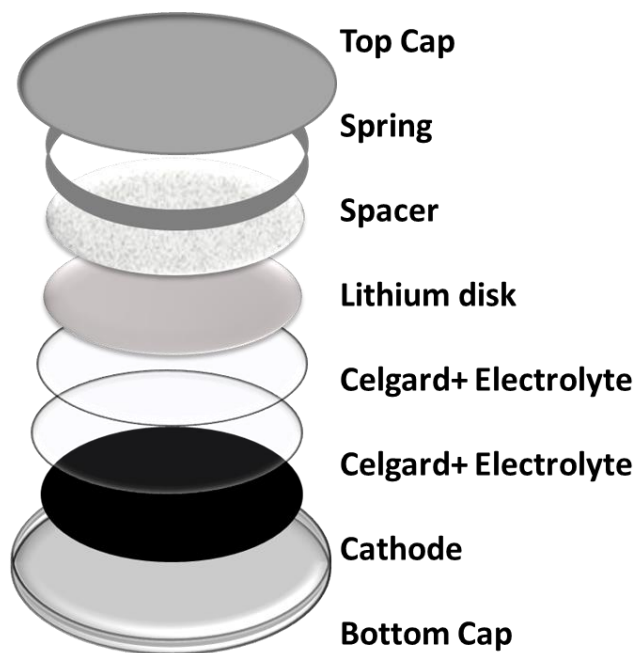


Figure 2.3 The order of the coin cell components.

The galvanostatic charge/discharge tests were carried out in a voltage range of 1.7–3 V. The sulfur loading was is calculated for each cell separately. All capacity values were calculated based on sulfur mass only. Cyclic voltammetry (CV) tests were conducted with a CHI 660D electrochemical measurement system. The CV tests were performed at the scan rate of 0.1 mV s^{-1} in the voltage range of 1.7–3 V.

References

- (1) Thommes, M.; Kaneko, K.; Neimark, A. V.; Olivier, J. P.; Rodriguez-Reinoso, F.; Rouquerol, J.; Sing, K. S. W. Physisorption of Gases, with Special Reference to the Evaluation of Surface Area and Pore Size Distribution (IUPAC Technical Report). *Pure Appl. Chem.* **2015**, *87* (9–10), 1052–1070.
- (2) Grattan-Bellew, P. E. 2- Petrographic and Technological Methods for Evaluation of Concrete Aggregates; Ramachandran, V. S., Beaudoin, J. J. B. T.-H. of A. T. in C. S. and T., Eds.; William Andrew Publishing: Norwich, NY, 2001; pp 63–104.
- (3) Goh, P. S.; Ismail, A. F.; Ng, B. C. Chapter 2 - Raman Spectroscopy; Hilal, N., Ismail, A. F., Matsuura, T., Oatley-Radcliffe, D. B. T.-M. C., Eds.; Elsevier, 2017; pp 31–46.
- (4) Konno, H. Chapter 8 - X-Ray Photoelectron Spectroscopy; Inagaki, M., Kang, F. B. T.-M. S. and E. of C., Eds.; Butterworth-Heinemann, 2016; pp 153–171.
- (5) Gewirth, A. A.; Varnell, J. A.; Diascro, A. M. Nonprecious Metal Catalysts for Oxygen Reduction in Heterogeneous Aqueous Systems. *Chem. Rev.* **2018**, *118* (5), 2313–2339.
- (6) Albery, W. J.; Hitchman, M. L. *Ring-Disc Electrodes*; Clarendon Press, 1971.
- (7) Paulus, U. A.; Schmidt, T. J.; Gasteiger, H. A.; Behm, R. J. Oxygen Reduction on a High-Surface Area Pt/Vulcan Carbon Catalyst: A Thin-Film Rotating Ring-Disk Electrode Study. *J. Electroanal. Chem.* **2001**, *495* (2), 134–145.

Chapter 3

Iron Phosphide Doped Porous Carbon as an Efficient Electrocatalyst for Oxygen Reduction Reaction

This chapter is mainly taken from my recent article. Adapted with permission from *Applied Energy Materials*, **2020**, *3*, 2537-2546. Copyright (2020) American Chemical Society.

3.1 Introduction

The development of sustainable and clean energy storage and conversion technologies is a highly viable approach to meet the increasing energy demands. Energy conversion systems such as alkaline fuel cells have gained interest due to superior features. They operate on a wide temperature range, with a maximum energy efficiency of at least 65%, and demonstrate high durability.¹

Pt/C and platinum group metal (PGM) are the catalysts used in all the fuel cells currently in production for the anodic oxidation of H₂ and the cathodic reduction of O₂. Platinum is an extremely rare and expensive metal and large-scale commercial production of such fuel cells are restricted by their prohibitive cost, limited supply, and weak

durability.² The use of the Platinum catalyst in fuel cells raises other operational deficiencies such as the vulnerability of PGM to potential drift over time, sluggish reduction reaction in the cathode, and decline of activity through methanol poisoning undermine its competitive catalytic activity. Among the investigated options for replacement of Pt, heteroatom -doped, porous carbon with a high specific surface area and tunable pore size coupled with suitable acceptor atoms such as nitrogen and phosphorus carry the viable characteristics for performing ORR.^{3,4} Also, dual-dopants combinations of heteroatom and transition metal doped, porous carbon materials are considered among the best candidates because of their high abundance and low cost. Most studies on this class of materials have focused on the optimal synthesis conditions and structure necessary for maximum activity.

Incorporation of iron into a phosphorus-doped carbon matrix through high-temperature carbonization has led to the formation of various Fe-P compounds giving rise to a series of ORR active electrocatalysts having enhanced kinetics in both alkaline and acidic electrolytes, highlighting the newly found synergistic effects between Fe and P, improving the reaction kinetics in acidic medium.⁵ More recently, Fe₂P nanoparticles derived from a biogenic precursor, encapsulated in a heteroatom-doped graphene-like carbon, have shown promising activity towards ORR in both acidic and alkaline electrolytes.⁶ The advantages of a heteroatom -doped porous carbon are 2-fold: stabilization of the nonprecious metal in the alkaline and acidic solution and generation of active sites for facilitating the ORR.

In this chapter, we report a viable synthesis of P and Fe-doped porous carbon (PFeC) using triphenylphosphine as a single-source precursor for both carbon and phosphorus through a simple one-step carbonization chemical activation route using anhydrous ZnCl_2 and FeCl_2 . With the high surface area and porosity of PFeC ($967 \text{ m}^2 \text{ g}^{-1}$) with well-defined and distributed, active centers, Fe_2P particles confined in a conjugated P-doped porous carbon framework exhibit high catalytic activity toward ORR with a comparable onset potential and a small negative shift in the half-wave potential to those of commercially available Pt/C (20 wt%) in acidic and alkaline electrolytes. Our results indicate that PFeC selectively performs ORR via a direct four-electron pathway and remains inert toward alcohol oxidation. PFeC has superior long-term stability compared to that of Pt/C.

3.2 Experimental Section

3.2.1 Sample Preparation

Triphenylphosphine (TCI, 99%), ZnCl_2 (Alfa Aesar, anhydrous, 98+%), and anhydrous FeCl_2 (Acros Organics, anhydrous, 98+%) were used as purchased. Triphenylphosphine flakes and the chemical activation agents, ZnCl_2 and FeCl_2 , were ground and mixed in the weight ratios of 1:1.5:1.5, respectively, inside an argon filled glovebox using a mortar and pestle. The light-yellow powder mixture was transferred to a Carbolite temperature-programmed tube furnace under a steady flow of argon. The temperature was increased at a ramp rate of $3\text{ }^\circ\text{C min}^{-1}$ and a hold time of 1 hour and then cooled to room temperature under a steady flow of argon. The triphenylphosphine derived carbon was given the name of PFeC-X, where P and Fe are the initials of the dopant elements and X indicates the activation temperature. Samples were prepared at 800, 900, and 1000 $^\circ\text{C}$, and the effects of carbonization temperature on the morphology and the electrocatalytic activity were studied. Triphenylphosphine was also carbonized with solely ZnCl_2 , solely FeCl_2 , and a eutectic mixture of the two, to achieve the highest miscibility between the salts and the organic precursor, to confirm that sufficient salt templating for the formation of a high surface area has occurred and an optimized product has been synthesized.⁷ Activation by ZnCl_2 and FeCl_2 yielded a nominal amount of product, ~1% yield. While activation by a eutectic mixture of ZnCl_2 and FeCl_2 , in which triphenylphosphine flakes, ZnCl_2 and FeCl_2 were mixed in a weight ratio of 1:2.5:0.5, respectively, yielding a type I nitrogen uptake isotherm with low pore volume and fewer mesopores. As such, these samples were excluded from ORR studies. The carbonized

products (PFeC-X) were purified by soaking in 4.0 M HCl to remove residual salts, metallic zinc, and excess metallic iron and then washed with 1.0 L of distilled water followed by ethanol for solvent-exchange to avoid capillary force driven pore collapse upon activation.⁸ To further understand the role of Fe in the structure, attempts were made to achieve complete leaching of Fe from the structure. The soaking step was replaced with acid leaching, where PFeC is stirred in 4 M HCl at 60 °C for an hour, followed by washing with DI water and ethanol. Further characterization shows that 99% of the original iron has been leached out, producing phosphorus-doped carbon termed PC. All samples were degassed for 12 h at 150 °C in a Quantachrome Autosorb-iQ before gas adsorption measurements. The product yields for PFeC-800, PFeC-900, and PFeC-1000 are 12%, 10%, and 7%, respectively, and the yield decreases with increasing temperature.

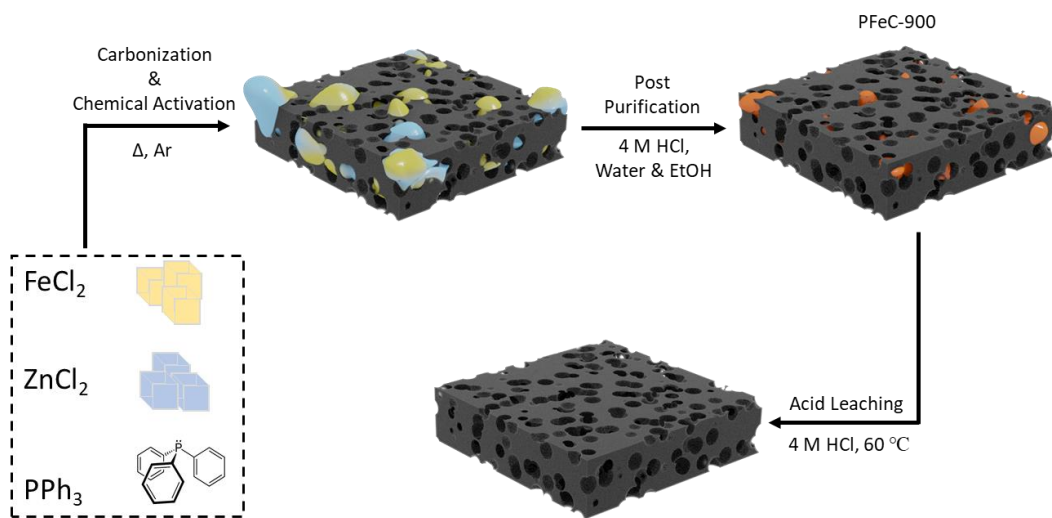


Figure 3.1 Reaction schematic of PFeC-900 and PC-900.

3.2.2 Electrochemical Measurements

The electrocatalytic activity for ORR was studied using a rotating ring-disk electrode (RRDE; glassy carbon disk and Pt ring) technique and rotating disk electrode (RDE; glassy carbon disk) connected to a modulated speed rotator (Pine Research) and CHI 600E potentiostat. The catalyst inks for electrochemical measurements were prepared by taking 12 mg of the PFeC and PC samples and ultrasonically dispersing them for 30 minutes in a mixture of 0.9 mL of ethanol solution and Nafion solution binder (50 μL , 5wt. % in aliphatic alcohols, Aldrich). Catalyst solution (6 μL) was cast onto the glassy carbon working electrode via controlled drops. The RRDE and RDE have areas of 0.237 cm^2 and 0.196 cm^2 , yielding loadings of 320 $\mu\text{g cm}^{-2}$ and 387 $\mu\text{g cm}^{-2}$, respectively. Following solvent evaporation, a thin layer of catalyst is left deposited on the surface of the working electrode. Commercially available 20 wt% Pt/C catalyst was prepared similarly to the other catalysts, while only 3 μL is drop casted on the glassy carbon achieving 20 $\mu\text{g}_{\text{Pt}} \text{cm}^{-2}$ loading. Doped-carbon samples were deposited on a glassy carbon as the working electrode, graphite rod (6 mm diameter) as the counter electrode, and Ag/AgCl (3 M KCl) as the reference electrode were used. Use of graphite rod as a counter electrode is highly encouraged; it has been reported that Pt can dissolve from the counter electrode and deposit on the working electrode, resulting in inaccurate electrochemical activity.⁹ All electrochemical measurements, including cyclic voltammograms (CVs), RRDE and RDE voltammograms, and chronoamperometry, were performed at room temperature using the mentioned three-electrode system in 0.1 M KOH solution for alkaline and 0.5 M H_2SO_4 for acidic half cells, which was purged with high-purity nitrogen or oxygen for at least 30

min before each measurement. To obtain stable CVs, the catalysts were cycled for 40 cycles between 0.2 and 1.2 V (vs RHE) in N₂ saturated solution. CVs were collected at a scan rate of 50 mV s⁻¹ and linear sweep voltammetry (LSV) at a scan rate of 10 mV s⁻¹. Ahead of each measurement, the working electrode was kept at the starting potential for 4 s. LSVs were corrected for the double-layer capacity by subtracting the LSV obtained in the N₂-saturated solution. The disk currents are normalized on the geometric area of the glassy carbon.

In the RRDE, the collection efficiency of the disk was measured to be N=0.38, during the RRDE measurement, the ring current is kept at 1.2 V vs RHE to oxidize the formed H₂O⁻. The yield of H₂O⁻ (%) and the electron transfer number (n) were calculated.

Tafel plots are reported, with the kinetic current which is calculated from the mass transport correction of LSV and in which J, J_L, and J_K are the measured current density, diffusion limiting current density, and kinetic current density, respectively.

3.2.3 Physical Characterization

Textural properties of doped porous carbon samples were investigated using nitrogen adsorption/desorption isotherms collected by Quantachrome Autosorb-iQ at 77 K based on the Brunauer–Emmett–Teller (BET) equation. Pore size distribution (PSD) analysis based on the N₂ isotherm was investigated via the nonlocal density functional theory (NLDFT) model. The ratio of the micropore volume to the total pore volume ($V_{\text{mic}}/V_{\text{total}}$) was calculated from the cumulative pore volume branch of PSD curves. Powder X-ray diffraction was examined with X-ray diffraction (P-XRD) patterns collected at room temperature using a Panalytical X'Pert Pro Multipurpose Diffractometer (MPD).

The samples were mounted on a zero-background sample holder measured in transmission mode using Cu K α radiation (operated at 40 kV, 45 mA; $\lambda=0.15418$ nm), the diffraction angle ranging from 10° to 70° with a step size of 0.02° and a rate of 1.2° min⁻¹. Raman spectroscopy of the sample was performed using a Thermo Scientific DXR Smart Raman spectrometer with a 523 nm excitation laser at a power of around 1 mW. X-ray photoelectron spectroscopy (XPS) analysis was performed on a Thermo Fisher Scientific ESCALAB 250 spectrometer employing an Al K α (1486.68 eV) X-ray source equipped with a hemispherical analyzer and XR5 Gun 500 μ m (15 kV). Samples for XPS measurements were prepared by pressing the carbon specimen into a piece of indium foil, which was then mounted onto the sample holder using double-sided tape. During XPS analysis, the combination of a low-energy electron flood gun and an argon ion flood gun was utilized for charge compensation. The binding energy scale was calibrated by setting the C 1s peak at 284.8 eV. The XPS results were analyzed with the CasaXPS software (v4.84). Inductively coupled plasma – optical emission spectrometry (ICP-OES) was also conducted, measuring the bulk composition of the metal in the carbonaceous structure. Scanning electron microscopy (SEM) images were obtained using a Hitachi SU-70 scanning electron microscope. Samples were prepared by placing each specimen onto the surface of a sticky carbon tape attached to a flat aluminum sample holder. Then the samples were sputter-coated with platinum at a pressure of 10⁻⁵ mbar in an N₂ atmosphere for 60 s before SEM imaging. Elemental mapping was obtained using energy-dispersive X-ray spectroscopy (EDX) attached to the SEM.

3.3 Result and Discussion

3.3.1 Characterization

Investigation of the textural properties of PFeC samples by nitrogen isotherms shows the surface areas of PFeC-800, PFeC-900, PFeC-1000, and PC-900 to be 1083, 967, 843, and 1137 $\text{m}^2 \text{g}^{-1}$ with a total pore volume of 0.744, 0.760, 0.574, and 0.765 $\text{cm}^3 \text{g}^{-1}$, respectively (Figure 3.2 and Table 3.1). According to IUPAC classification, all four samples show a hybrid type I/IV isotherm with a sharp initial rise in the N_2 uptake at very low relative pressures, a distinct feature of type I isotherms consisting of micropores, followed by a gradual increase in the uptake for the remaining of the pressure range, indicating the presence of mesopores. In the case of a type IV isotherm, the hysteresis suggests the existence of pores wider than 4 nm (Figure 3.2a).¹⁰ Narrow mesopores were found to be positively contributing to the faster kinetics of PFeC-900, further discussed in the electrochemistry section.¹¹ It can be concluded from the desorption branch of the N_2 isotherms in Figure 3.2a that PFeC-800, PFeC-1000, and PC-900 contain bottleneck mesopores (inverse H2 hysteresis),¹⁰ which hinder the catalytic activity of the catalysts.¹² On the other hand, a continuous opening of the pore system for PFeC-900 leads to H3 hysteresis in the desorption branch.¹⁰ We also applied the BJH model (Barrett–Joyner–Halenda) to the desorption branch of the isotherms and the PSD data were consistent with the results obtained from NLDFT; however, large mesopores (>7 nm) were absent for all samples. Given the fact that triphenylphosphine has a much lower melting point than those of ZnCl_2 and FeCl_2 as well as that of their eutectic mixture,¹³ we anticipate these salts to facilitate pore formation during the initial carbonatization steps. We have

noticed that when our carbonization experiments were performed using solely ZnCl_2 and solely FeCl_2 , the product yield was nominal, indicating that both salts were necessary for the formation of the carbon matrix.

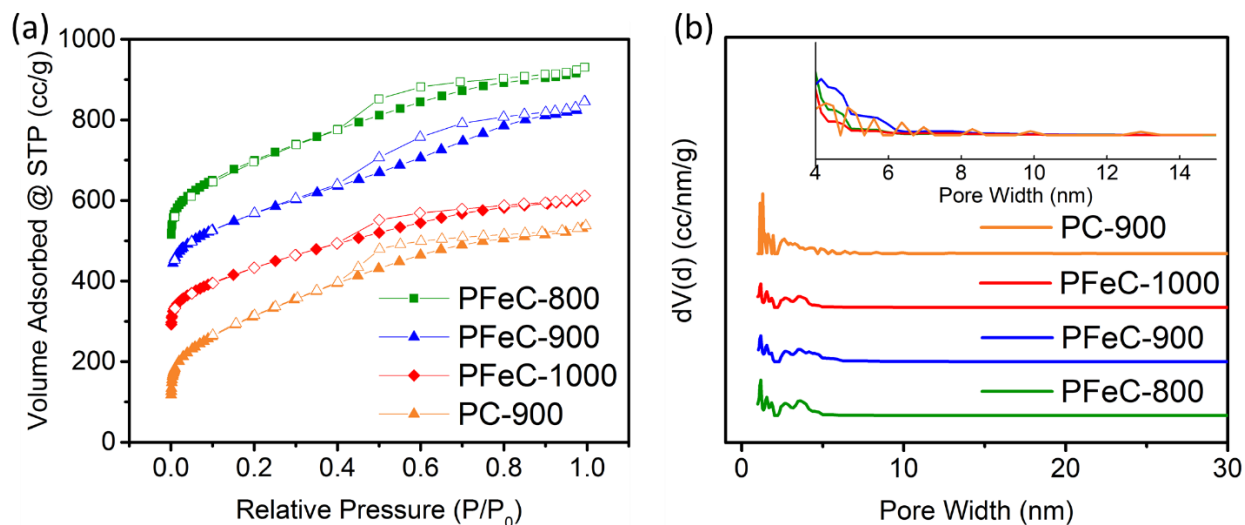


Figure 3.2 (a) N_2 sorption isotherm of PFeC-800, PFeC-900, PFeC-1000, and PC-900 at 77 K (solid symbols denote adsorption points, and hollow symbols denote desorption points; isotherms are offset in steps of 100). (b) Pore size distribution from NLDFT model using N_2 isotherms at 77 K (PSD curves are offset in steps of 1). The inset in panel b compares the pore size distribution in the range of 4–15 nm without an offset.

The presence of an open pore system for PFeC-900 is expected to enhance the ORR performance of the catalyst. Bottleneck pores hinder mass transport at low current densities, i.e., small O_2 concentration gradients, leading to poor kinetics and inefficient use of specific surface area active centers.^{12,14} Open pores, in contrast, result in faster kinetics and allow full employment of the specific surface area as an electrochemically active surface area. Pore tuning is a powerful tool to improve the catalytic performance, which

can be confirmed by N₂ isotherms, and accounts for the improved electrocatalytic activity of PFeC-900 in comparison to those of PFeC-800, PFeC-1000, and PC-900. PFeC-900 has a higher pore volume and a higher percentage of mesopores (Table 3.1), both contributing to the faster kinetics of this electrocatalyst.¹¹ Upon acid treatment for Fe-leaching, PC-900 exhibits a more featured pore size distribution curve (Figure 3.2 b, inset). It is presumed that acid treatment causes metal centers to vacate the carbon framework, leaving behind a wide range of pores ~ 5–15 nm, however, the overall pore volume of the mesopores is lower than the value obtained for PFeC-900, perhaps due to pore collapse or clogging.

Table 3.1 Textural Properties of PFeCs Determined by Nitrogen Porosity Measurements.

Sample	S _{BET} ^a (m ² g ⁻¹)	V _{TOT} ^b (cm ³ g ⁻¹)	V _{mic} ^c (cm ³ g ⁻¹)	V _{meso} ^c (cm ³ g ⁻¹)
PFeC-800	1083	0.744	0.262	0.482 (65%)
PFeC-900	967	0.760	0.228	0.532 (70%)
PFeC-1000	843	0.574	0.212	0.362 (63%)
PC-900	1137	0.765	0.310	0.455 (59%)

^a Brunauer–Emmett–Teller (BET) surface area. ^b Total pore volume at P/P₀ = 0.99. ^c Determined by PSD assuming slit-shaped pores and the NLDFT model from N₂ adsorption data at 77 K (the values in parentheses are the percentages of mesopore volume relative to total pore volume).

P-XRD patterns for the PFeCs and PC samples show broad peaks at ~23° correspond to the (002) planes of carbon sheets and more pronounced sharp peaks at 40° (111), 44° (201), 47° (210), 52° (002), and 54° (300) consistent with crystalline Fe₂P phase

(JCPDS NO. 51-0942) as depicted in Figure 3.3a.^{6,15} Using the Scherrer equation the particle size range is 12–350 nm. The disappearance of all of the Fe₂P characteristic peaks for PC-900 suggests Fe₂P leaching upon acid treatment. The remaining graphitic peak at 23° that corresponds to the (002) planes exhibits a small shift toward a lower 2θ from the typically expected 26° peak for graphitic structures. This observation is consistent with the presence of the large phosphorus atoms which increase the interlayer spacing between graphitic carbon sheets (Figure 3.3 a, inset).^{16,17} Raman spectroscopy was conducted on all samples, yielding two distinctive peaks as shown in Figure 3.3b. A peak at ~ 1341 cm⁻¹ corresponds to the D band associated with the vibrational mode of the defects and the edges of the carbon structure and the second peak at ~ 1595 cm⁻¹ corresponds to sp²-hybridized carbon vibration known as the G band were observed. Ratio I_D/I_G was used to measure the level of disorder in the high surface area doped carbon, and the values were calculated to be 1.04, 1.08, 1.09, and 1.07 for PFeC-800, PFeC-900, PFeC-1000, and PC-900, respectively. These results indicate a small increase in the I_D/I_G ratio with the increase in the carbonization temperature. The I_D/I_G ratios also confirm that, along with the presence of edges and active sites, lower concentrations of defects keep the integrity of the sp²-hybridized carbon that retains the carbon framework intact, enhancing the electron transfer properties and keeping the reduction potential positively shifted.¹⁸

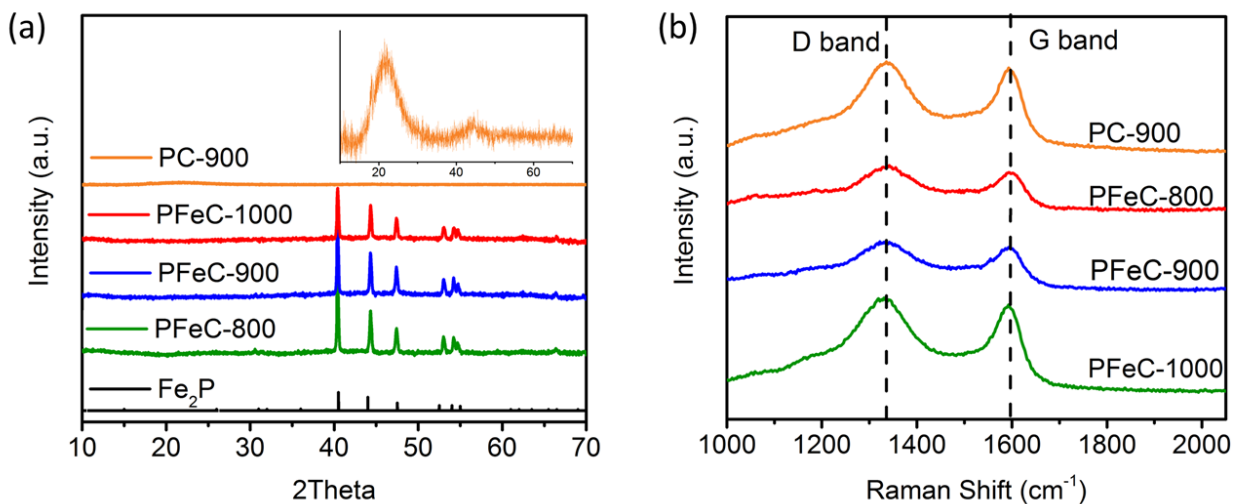


Figure 3.3 (a) P-XRD patterns for PFeCs and PC-900. The inset depicts the detailed pattern for PC-900. (b) Raman spectra with corresponding D and G bands.

To determine the bulk composition of Fe in all samples, ICP-OES was performed. Samples (5 mg) were digested in aqua regia overnight, and 5% nitric acid matrices were prepared using the entire digested samples. Iron contents were found to be 20 wt% (PFeC-800), 22 wt% (PFeC-900), and 30 wt% (PFeC-1000). The increase in iron weight percent in PFeC-1000 can be reasoned by the decomposition of the carbon matrix.¹⁹ This is in agreement with PFeC-1000 having a slightly higher I_D/I_G ratio than PFeC-900, suggesting an increase in defects and edge sites induced by the high content of iron and oxygen as well as a simultaneous loss of graphitic carbon matrix.

XPS survey and element spectra for all samples are reported in figures 3.4 - 3.7 and the surface elemental composition calculated using XPS survey spectra is reported in table

3.2. XPS survey spectra for PFeC-900 provides the surface chemical composition and confirms the presence of carbon, oxygen, phosphorus, and iron (Figure 3.5a). The C 1s spectra of PFeC-900 shows the dominant presence of sp^3 -hybridized carbon, suggested by a peak at 284.8 eV and an asymmetric tail towards higher binding energies.²⁰ Deconvolution of the C 1s spectrum shows peaks for the sp^2 -hybridized carbon-carbon double bond at 285.4 eV, C-P at 286.3 eV, and metal carbonate at 289.7 eV²¹ (Figure 3.5b). The two peaks at 129.6 and 130.3 eV in P 2p spectra have been assigned to phosphide (Fe_2P) in low binding energy, P $2p_{1/2}$, and high binding energy, P $2p_{3/2}$, respectively.²² A peak at 129.6 eV establishes the presence of anodic P species within the phosphide as it has lower binding energy than elemental P (129.9 eV) by 0.3 eV.²³ A peak at 132.0 eV can be assigned to P-C binding, which confirms the presence of the P atom in the doped carbon lattice.²⁴ As the surface oxidation of the Fe_2P particles is unavoidable, a peak at 133.3 eV has been observed for phosphorus in high oxidation state and refers to surface oxidized P species^{25,26} (Figure 3.5c). The deconvolution of the Fe 2p spectra agrees with a good correlation between iron and phosphorus. The presence of Fe in the form of iron phosphate is suggested with doublet peaks at Fe $2p_{3/2}$ and Fe $2p_{1/2}$ at 711.4 and 724.2 eV, respectively, caused by surface oxidation, and the set of peaks at 707.5 and 720.0 eV can be assigned to Fe in Fe_2P (Figure 3.5d).^{15,25} Detailed deconvolution of O 1s suggests C-O, an oxidized derivative of an aromatic compound with a peak at 533.3 eV.²⁷ A peak at 532.0 eV can be assigned to P-O-P and a smaller peak at 531.0 eV suggests the presence of Fe-O-P. A small metal oxide peak can be detected at 530.0 eV, confirming the above statement, the majority of iron is in the form of iron phosphide and not iron oxide.²⁸ A broad peak at 535.2

eV can be assigned to COOH, the carboxylic group²⁹ (Figure 3.5e). Surface oxidation is a common phenomenon for samples exposed to the atmosphere, especially those containing metals.

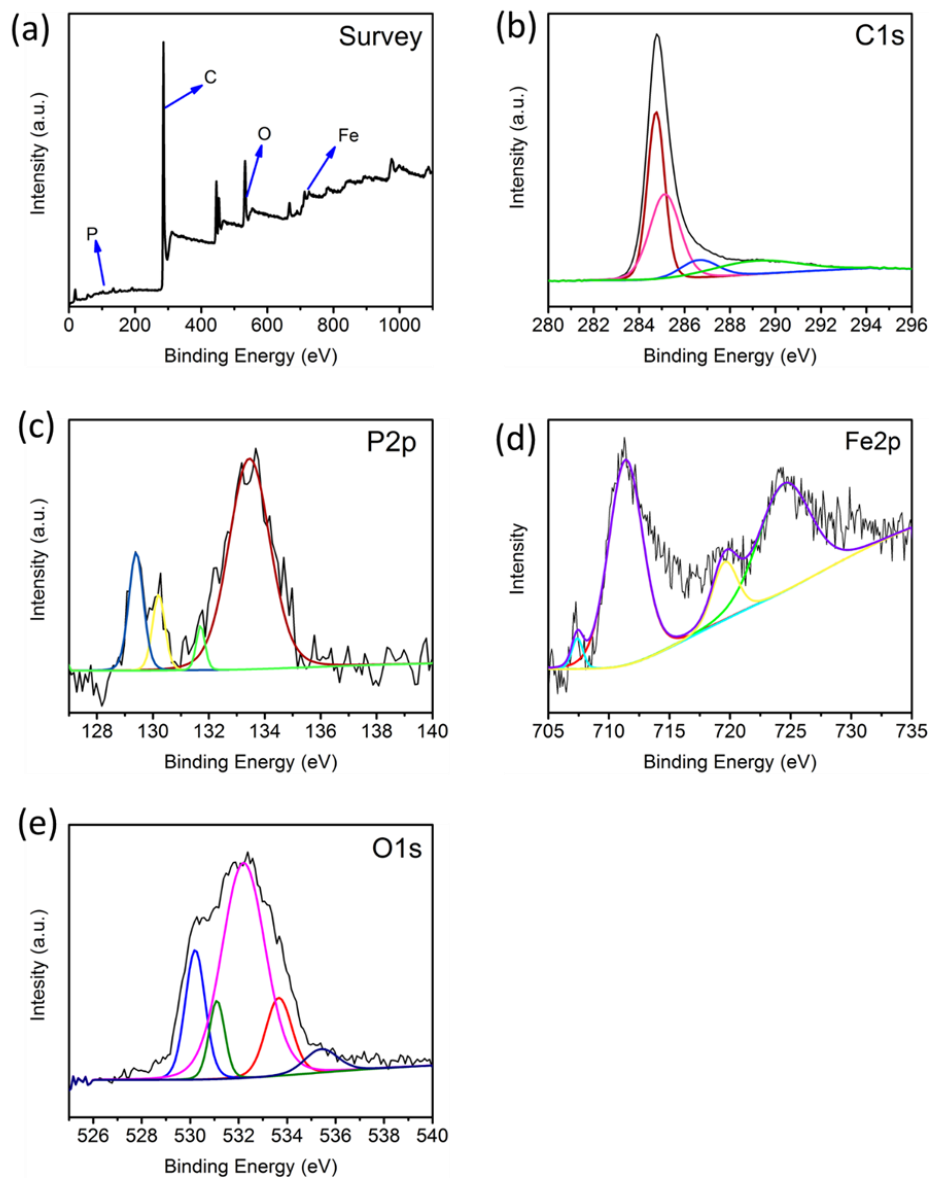


Figure 3.4 (a) Survey spectra of PFeC-800. (b) Deconvoluted C 1s spectra. (c) Deconvoluted P 2p spectra. (d) Deconvoluted Fe 2p spectra. (e) Deconvoluted O 2p spectra.

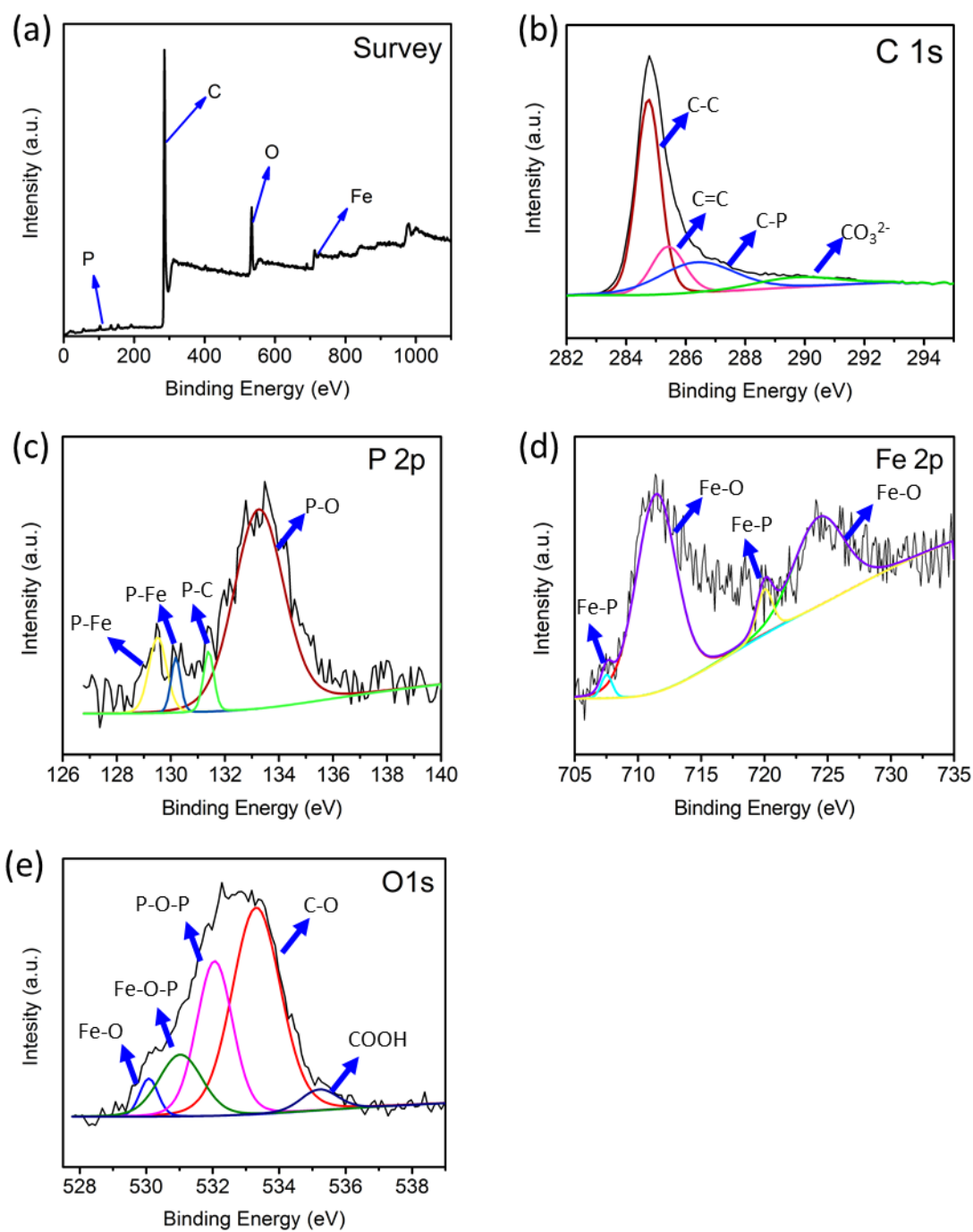


Figure 3.5 (a) Survey spectra of PFeC-900. (b) Deconvoluted C 1s spectra. (c) Deconvoluted P 2p spectra. (d) Deconvoluted Fe 2p spectra. (e) Deconvoluted O 2p spectra.

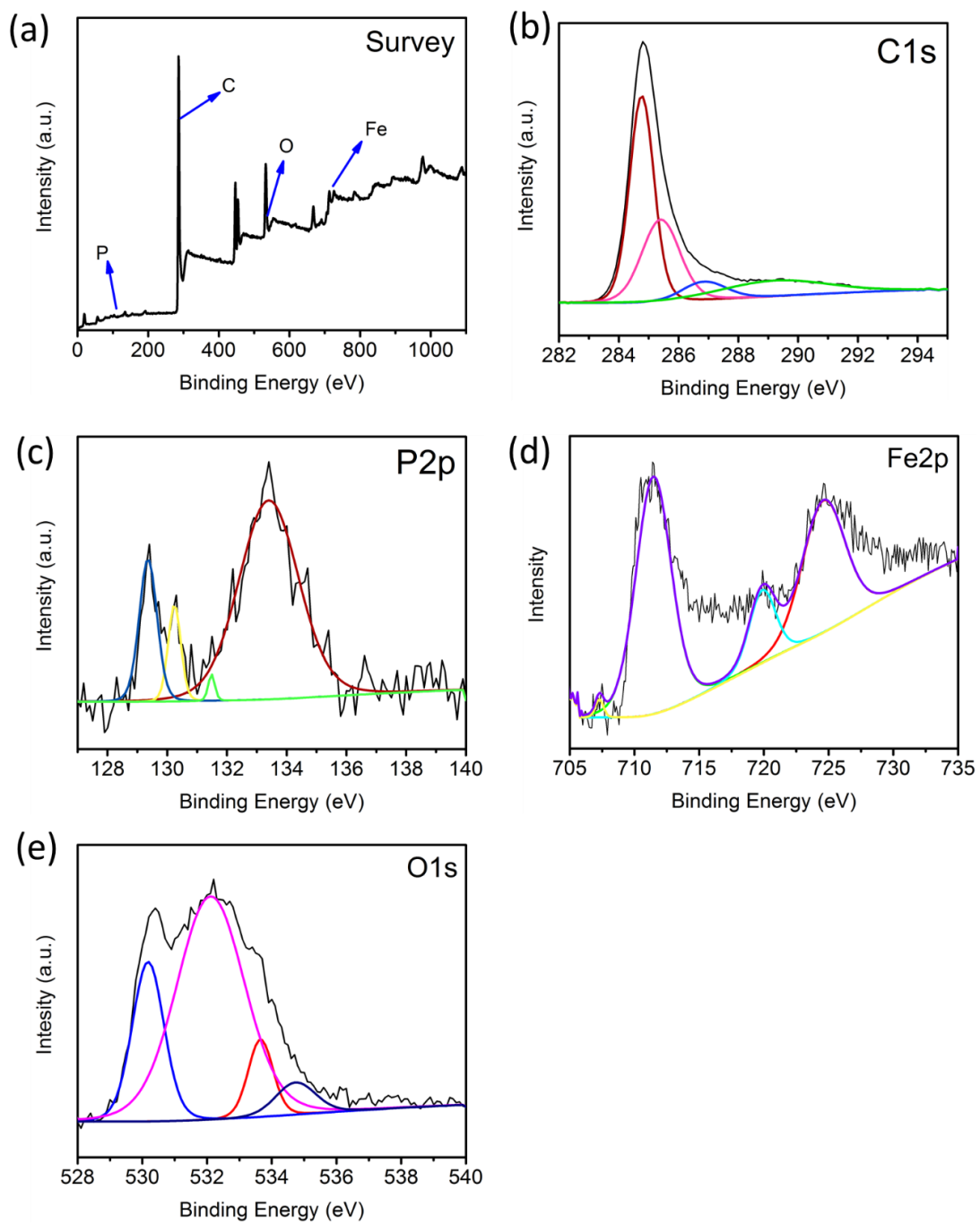


Figure 3.6 (a) Survey spectra of PFeC-1000 (b) Deconvoluted C 1s spectra (c) Deconvoluted P 2p spectra (d) Deconvoluted Fe 2p spectra (e) Deconvoluted O 1s spectra.

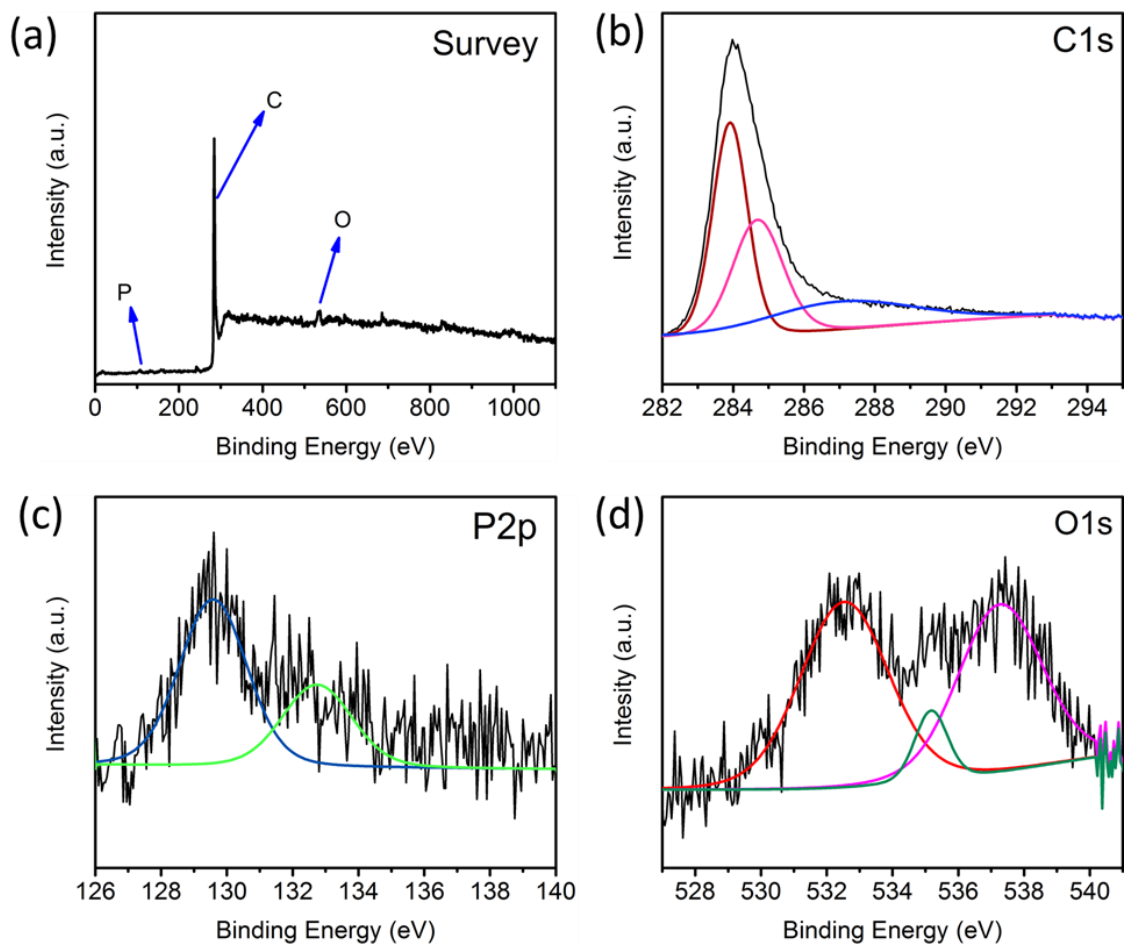


Figure 3.7 (a) Survey spectra of PC-900 (b) Deconvoluted C 1s spectra (c) Deconvoluted P 2p spectra (d) Deconvoluted O 1s spectra.

Table 3.2 Surface and bulk chemical composition of PFeC-800, 900, 1000 and PC-900 collected from XPS, EDX and the iron weight percent collected from ICP-OES.

Sample	C (At%) XPS/EDX	O (At%) XPS/EDX	P (At%) XPS/EDX	Fe (At%) XPS/EDX/ICP
PFeC-800	89.2/86.6	9.2/1	1.2/2.9	0.4/9.5/20(wt%)
PFeC-900	90.6/84	8/2.1	1.1/4.1	0.4/9.8/22(wt%)
PFeC-1000	88.9/88.4	9.5/1.9	1.1/3.1	0.5/6.6/30(wt%)
PC-900	95.4/92	3.6/7	1/1	0/0/0.5(wt%)

The morphology of the PFeCs was studied by SEM (Fig. 3.8 – 3.11). As expected for doped carbon frameworks, all samples show flakes with rough surfaces and edges.³⁰ The deformed spherical particles are found to be Fe₂P, distributed on the surface, and inside of all PFeC samples (Figure 3.9a–d). Additional imaging of the sample without platinum sputter coating reveals bright Fe₂P particles on the surface and others embedded inside the carbon matrix. These particles were missing from the imaged surface of the Fe-etched carbon, PC-900, leaving voids behind (Figure 3.11). EDX supports a uniform distribution of Fe₂P/Fe₂PO particles inside and on the carbon framework (Figures 3.8 – 3.11). Element percentages for all four samples are reported by XPS and EDX in Table 3.2. It is noticeable that the overall contents for each element are very similar; however, the XPS values for the heavier elements, phosphorus, and iron, are substantially lower than those obtained by EDX because of the limited depth of XPS. For iron content in the samples, the most effective method is ICP, which shows higher values than what is observed from both XPS and EDX. Since PFeC-900 contains a higher content of phosphorus and iron, it is

anticipated to exhibit a more competitive ORR electrocatalytic activity compared to other PFeC samples. According to surface chemical composition data collected for these catalysts using XPS and EDX, iron content for PFeC-1000 is almost identical when measured by XPS and 3.2 at. % lower than PFeC-900 based on EDX data. Since only the particles exposed on the surface participate in the catalytic activity, it is expected that PFeC-900 will have a better performance. The higher bulk iron content in PFeC-1000 collected by ICP-OES can be reasoned by the decomposition of the carbon matrix. The loss of graphitic carbon matrix correlates with the lower surface area of PFeC-1000, which can also affect the overall electrocatalytic activity. Since PFeC-900 contains a higher content of phosphorus and iron, it is anticipated to exhibit a more competitive ORR electrocatalytic activity compared to other PFeC samples.

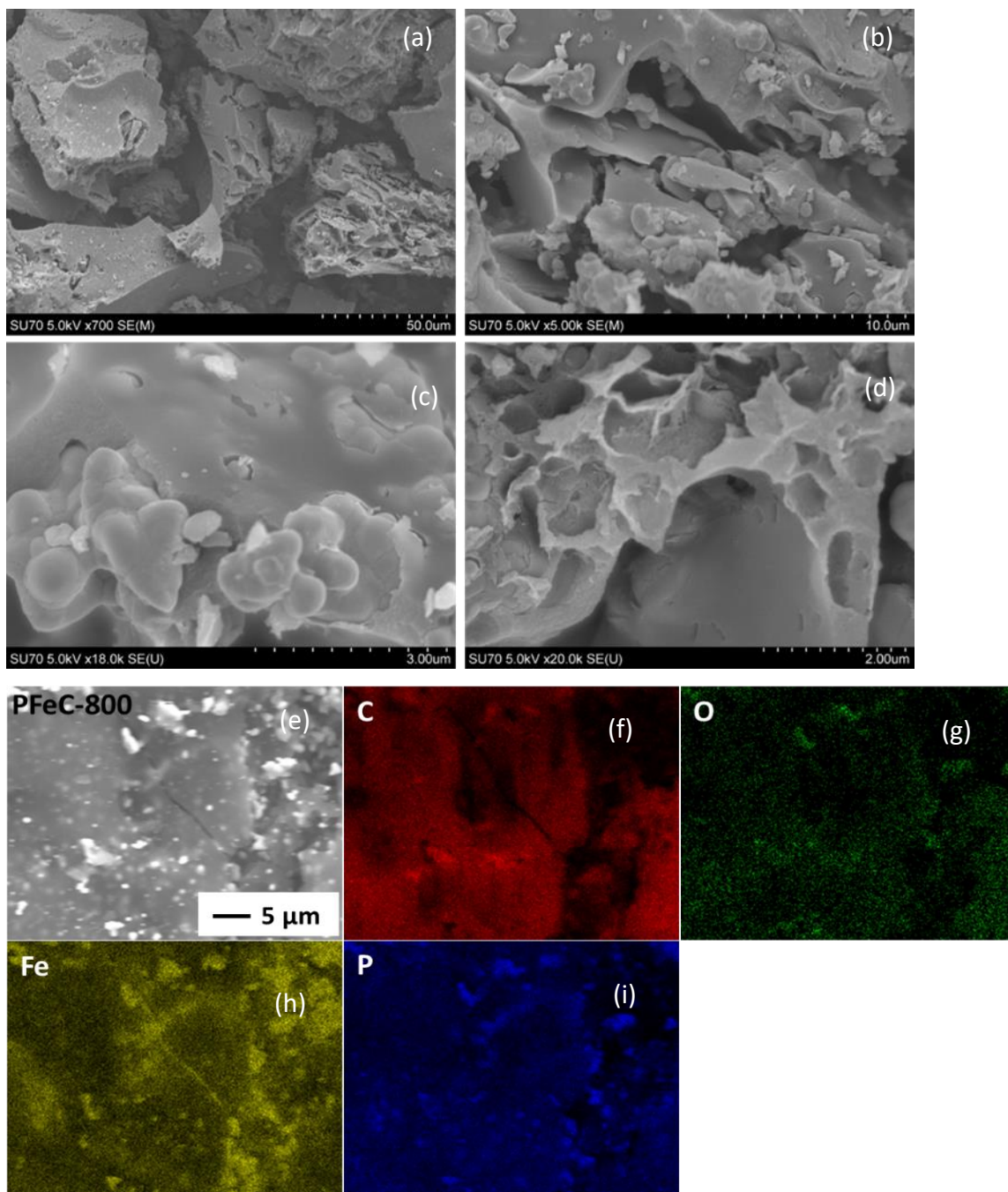


Figure 3.8 (a-d) SEM images of PFeC-800. (e-i) EDX elemental mapping displaying the distribution of elements in PFeC-800.

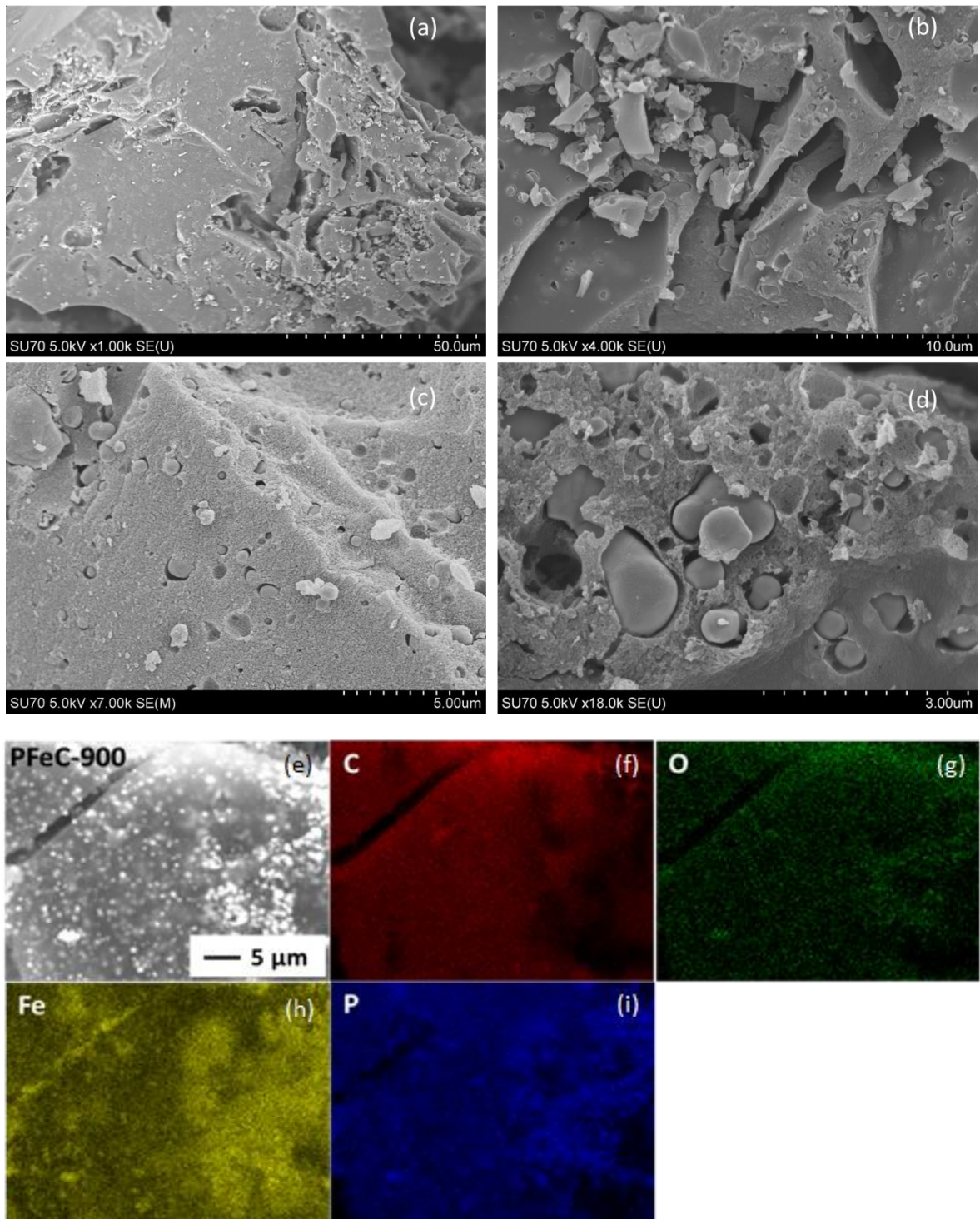


Figure 3.9 (a–d) SEM images of PFeC-900. (e–i) EDX elemental mapping displaying the distribution of elements in PFeC-900.

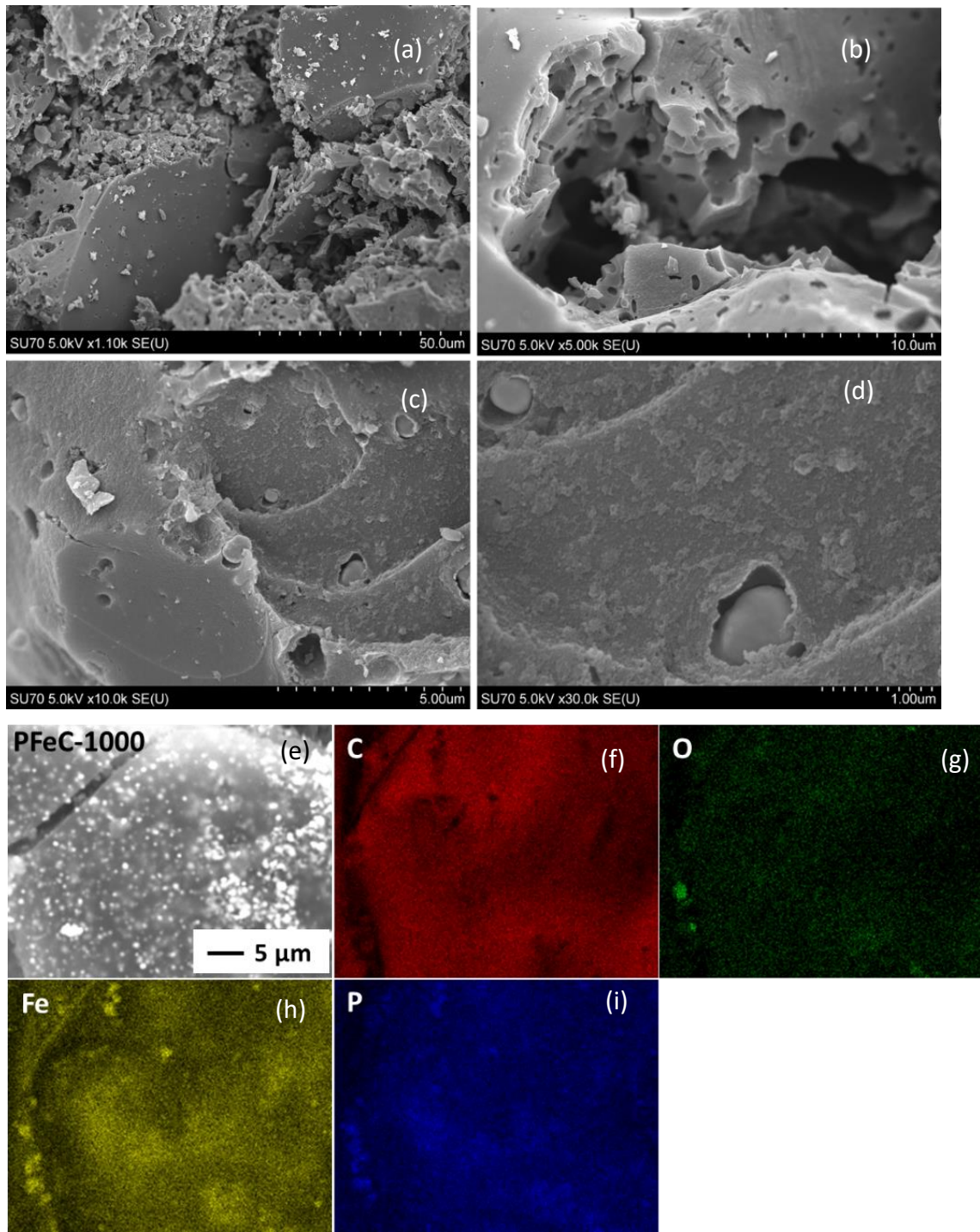


Figure 3.10 (a–d) SEM images of PFeC-1000. (e–i) EDX elemental mapping displaying

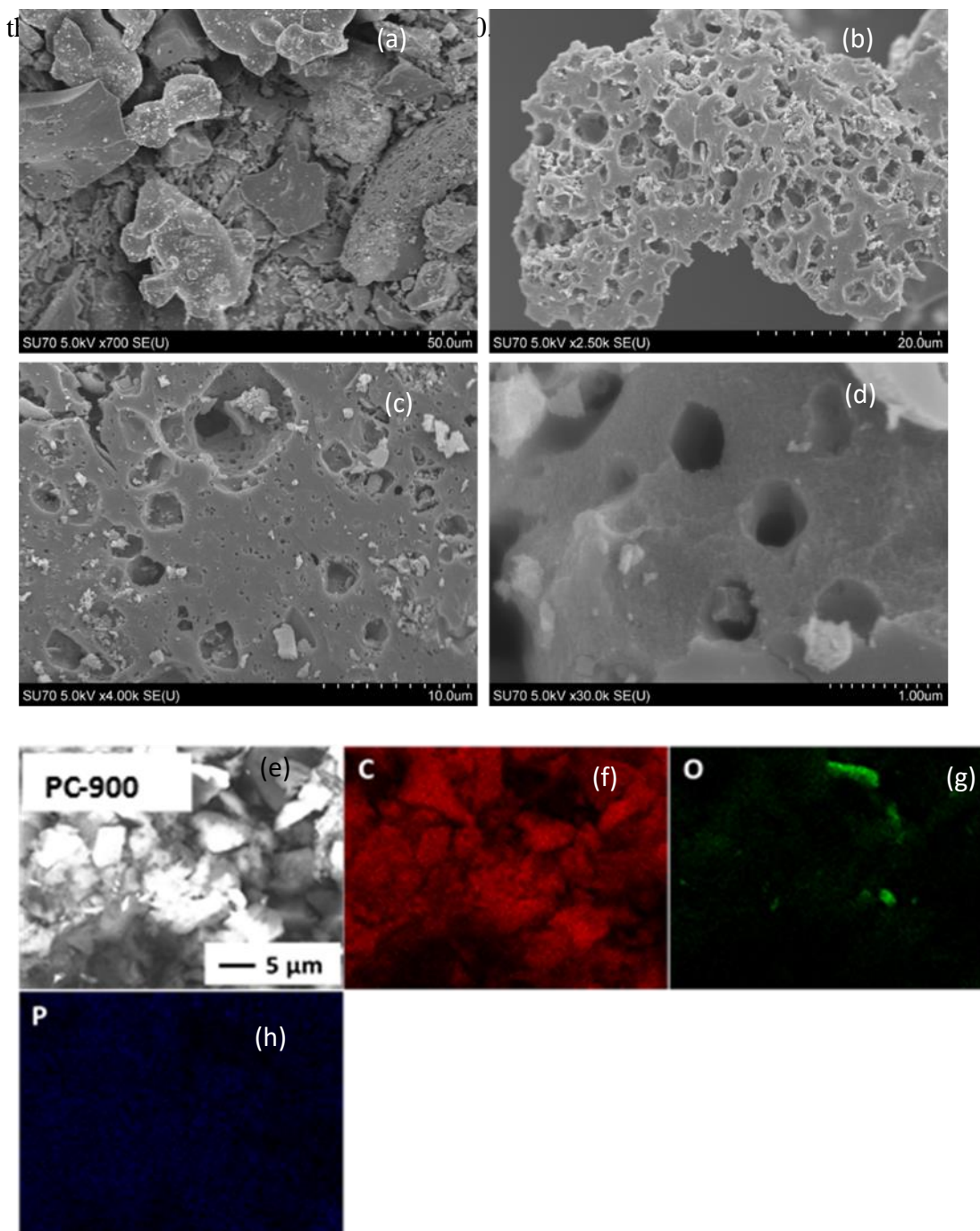


Figure 3.11 (a–d) SEM images of PC-900. (e–h) EDX elemental mapping displaying the distribution of elements in PC-900.

3.3.2 Electrochemical Measurements

The electrocatalytic activity of all of the catalysts toward ORR was studied with RRDE in 0.1 M KOH (Fig. 3.12). The LSVs of the prepared catalysts, PFeC-800, PFeC-900, PFeC-1000, and PC-900, and the commercially available 20 wt% Pt/C were collected in O₂-saturated electrolyte at a rotation rate of 1600 rpm (Fig. 3.12 a). All catalysts showed competitive onset potentials, half-wave potentials, and diffusion limiting currents, with PFeC-900 having superior electrocatalytic activity compared to the other four catalysts (Table 3.3). PFeC-900 shows a high onset potential of 1.01 V vs. RHE, half-wave potential of 0.88 V vs RHE, and high limiting current of -8.38 mV cm^{-2} . The half-wave potential of PFeC-1000 showed a shift toward higher potentials at 0.86 V while having a high limiting current at -7.92 mV cm^{-2} . PFeC-800 showed a half-wave potential of 0.84 V. The more positive potential is due to a tilted reduction wave in the mixed kinetic–diffusion control region $0.75 \text{ V} < E < 1.00 \text{ V}$, leading to a mixed diffusion-limited current density plateau (I_{lim}) in the potential region $0.20 \text{ V} < E < 0.70 \text{ V}$. When compared to the other two PFeC catalysts, it has a more negative onset potential and a lower diffusion limiting current. In contrast, the Fe₂P-etched sample PC-900 has the lowest onset potential at 0.95 V and has the largest negative shift for $E_{1/2}$ at 0.79 V vs RHE. This decline in activity is most likely due to the removal of Fe₂P through acid treatment, which highlights the importance of supported Fe₂P in ORR activity in an alkaline electrolyte. Figure 3.12 shows LSV at a rotating speed of 100–2500 rpm with a scan rate of 10 mV s^{-1} collected for PFeC-900.

Table 3.3 Electrocatalytic Activity, Onset Potential, Half Wave Potential and Limiting Current of PFeC-800, 900, 1000, PC-900 and Pt/C in O₂ Saturated 0.1 M KOH.

Sample	E _{Onset} (V vs. RHE)	E _{1/2} (V vs. RHE)	j _{lim} (mV cm ⁻²)
PFeC-800	0.98	0.84	-7.75
PFeC-900	1.01	0.88	-8.38
PFeC-1000	0.98	0.86	-7.92
PC-900	0.95	0.79	-9.01
Pt/C	1.04	0.90	-8.70

The competitive values collected for PFeC-900 can be traced back to a combination of chemical and physical properties as well as the surface morphology of the catalyst. PFeC-900 has the highest content of iron and phosphorus atoms and, hence the highest number of ORR active sites. It has a large total pore volume (0.76 cm³ g⁻¹) and mesoporous volume (0.53 cm³ g⁻¹), both contributing to the faster kinetics of ORR.¹¹ PFeC-800 has the second-highest content of Fe₂P active sites overall and higher surface area but lower pore volume than PFeC-900. These factors hinder the activity of PFeC-800 in comparison to PFeC-900. According to Yu et al., among samples synthesized at varying temperatures, the synergistic effect of Fe–P species along with mesopores content was found to be more effective in enhancing the ORR activity.⁵ Comparing PFeC-900, which has the most competitive catalytic activity toward ORR, with the commercially available 20 wt% Pt/C, it was found that PFeC-900 exhibits a 4% lower diffusion limiting current than Pt/C. The

LSVs at 1600 rpm showed a small negative shift of 30 mV s^{-1} and 20 mV s^{-1} for onset potential, and half-wave potential respectively (Figure 3.12a).

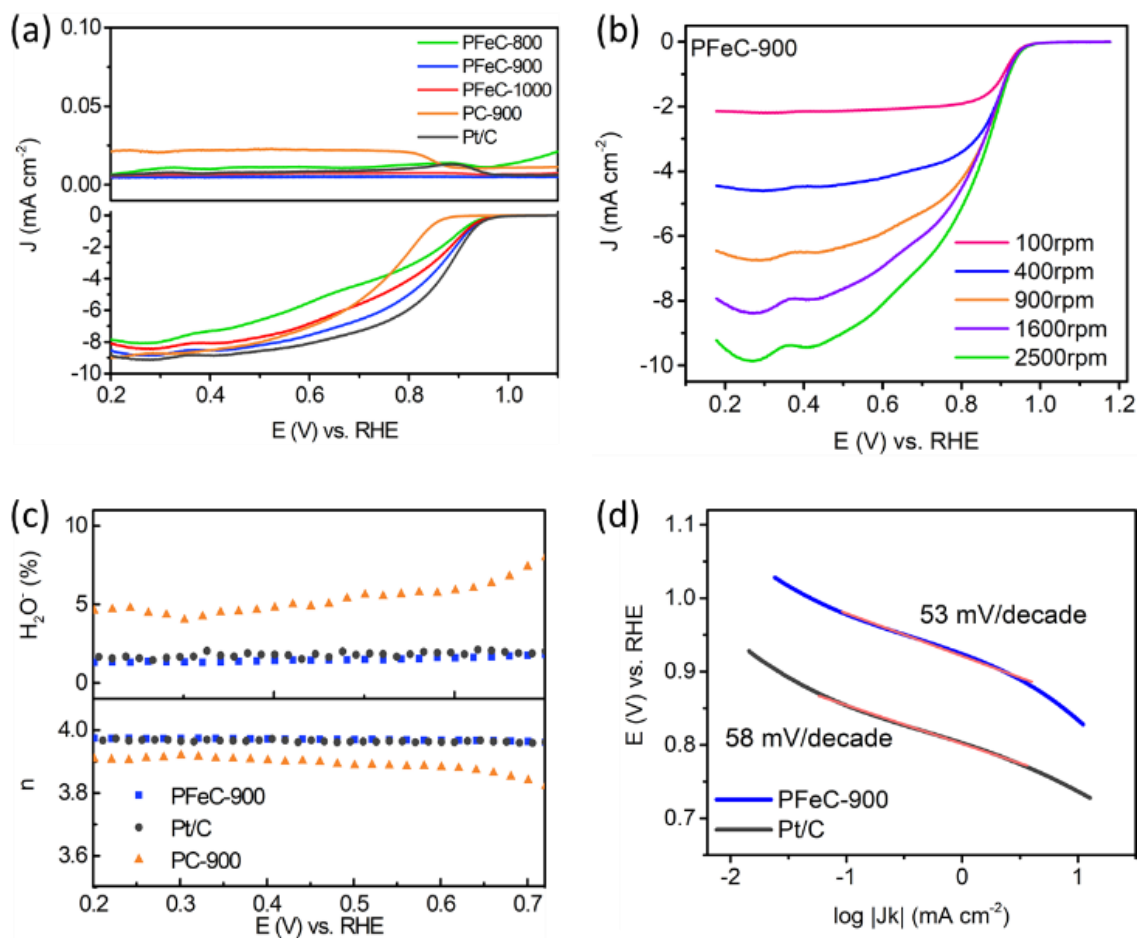


Figure 3.12 (a) LSV curves for PFeC-800, -900, and -1000, PC-900, and Pt/C in O_2 -saturated 0.1 M KOH using RRDE and the corresponding ring current densities. (b) Polarization curves for PFeC-900 in O_2 -saturated 0.1 M KOH at rotation rates 100–2500 rpm. (c) Top graph, H_2O^- % and bottom graph, electron transfer numbers for PFeC-900, PC-900, and Pt/C calculated from the LSV curves at 1600 rpm, and (d) Tafel slopes for PFeC-900 and Pt/C.

PFeC-900 has one of the most competitive onset and half-wave potentials in comparison with the catalysts reported entailing phosphorus and iron/phosphorus-doped

carbon, as summarized in Table 3.4. Unlike other catalysts, the ring current for PFeC-900 did not show the evolution of a current density wave (Figure 3.12a). The yield of hydrogen peroxide and the electron transfer number (n) can be calculated from the voltammograms of PFeC-900 and Pt/C at 1600 rpm using the currents collected by the ring and disk electrodes (Figure 3.12c). PFeC-900 shows competitive activity in comparison with Pt/C, and it favors the one-step ORR pathway with electron transfer $n = 3.97$, and a nominal amount of H_2O^- is detected by the ring. The mass transport corrected Tafel plot that compares the ORR mechanism at lower overpotentials is depicted in Figure 3.12d. The Tafel slope of 58 mV dec^{-1} was calculated for PFeC-900 which is close to 53 mV dec^{-1} for Pt/C, showing an ORR mechanism similar to that of commercial Pt/C.

CV studies of the catalysts in 0.1 M KOH were conducted using stationary RDE at a scan rate of 50 mV s^{-1} (Fig. 3.13). PFeC-900 performance in N_2 -saturated solution shows a featureless voltammogram and the electrochemical activity of the cathode in an O_2 -saturated electrolyte results in a peak appearing at 0.8 V. For comparison, when Pt/C was run under the same condition, it exhibited a single cathodic reduction peak at 0.85 V in the O_2 -saturated electrolyte. The area under the PFeC-900 CV curve is larger than that of Pt/C, suggesting a higher capacitive current as a result of a higher electroactive surface area (Figure 3.13a).³¹

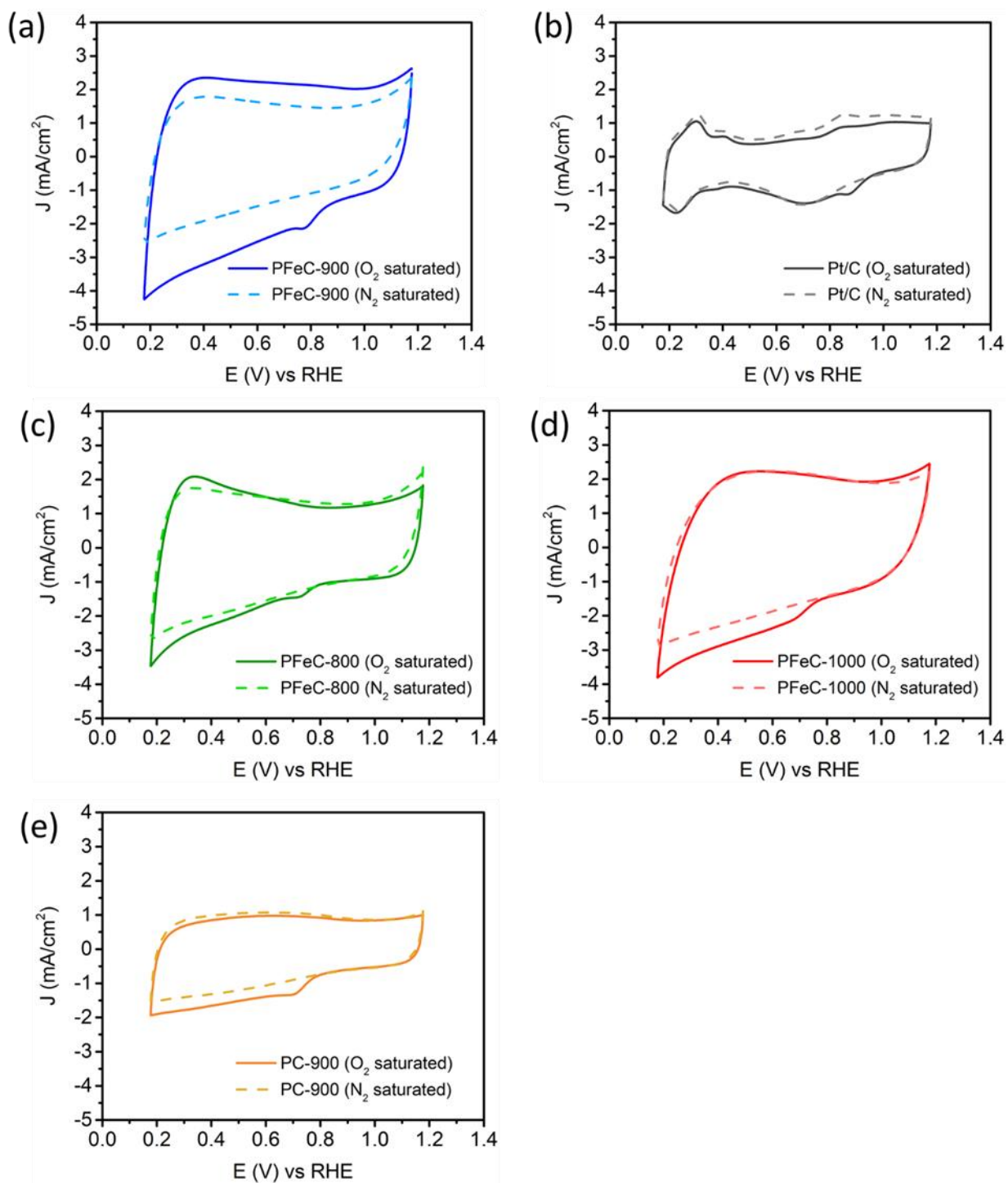


Figure 3.13 The CV of (a) PFeC-900 and (b) Pt/C (c) PFeC-800, (d) PFeC-1000 (e) PC-900 in N₂ and O₂ saturated 0.1 M KOH using RDE at scan rate of 50 mV s⁻¹.

The behavior of the electrocatalysts in acidic medium, 0.5 M H₂SO₄, was also studied (Fig. 3.14–3.16). Figure 3.14a shows the linear sweep voltammograms of prepared catalysts; PFeC-900, PC-900, and the commercially available 20 wt% Pt/C, collected in O₂-saturated electrolyte at a rotation rate of 1600 rpm (Fig. 3.14a). PFeC-900 shows a competitive onset potential of 0.95 V vs RHE, a half-wave potential of 0.71 V vs RHE, and a diffusion limiting current of -6.61 mA cm^{-2} . In comparison to the activity of Pt/C in acidic electrolyte, the catalytic activity of PFeC-900 was found to be very competitive. Also, PFeC-900 surpasses the activity of PC-900 ($E_{1/2}$ of 0.6 V and J_{lim} of -6.22 mA g^{-2}) as shown in Figure 3.14a. The presence of iron plays an important role in facilitating the adsorption of O₂ and its efficient reduction reaction. The catalyst containing iron phosphides yielded an electron transfer number of 3.9, with less than 2% hydrogen peroxide detected by the ring electrode, whereas the reduction reaction utilizing PC-900 yielded 12% hydrogen peroxide with and an electron transfer number of 3.5 at the diffusion-limited current density region of the LSV curve (Figure 3.14b).

PFeC-900 shows competitive activity in both alkaline and acidic electrolytes with the onset and half-wave potential values comparable to those of 20 wt% Pt/C. The activity recorded for PC-900 seems to be closer to PFeC-900 in the alkaline medium than acidic medium (Figure 3.17), which suggests that the presence of Fe and the synergistic effect between Fe and P play a more crucial role in alkaline medium.

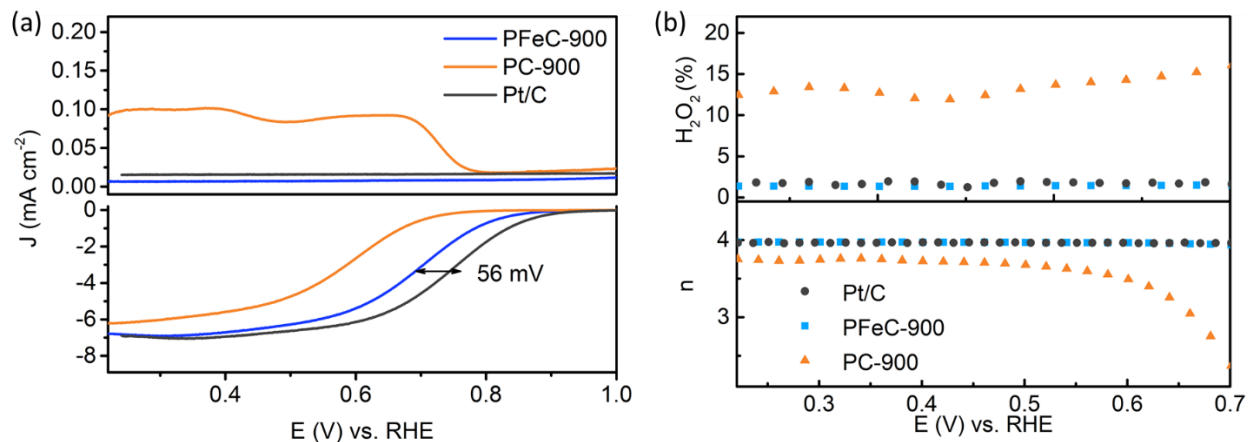


Figure 3.14 (a) LSV curves for PFeC-900, PC-900, and Pt/C in O₂-saturated 0.5 M H₂SO₄ using RRDE and their corresponding ring currents. (b) Top graph, H₂O₂ yielded % and bottom graph, electron transfer numbers for PFeC-900, PC-900, and Pt/C calculated from the LSV curves at 1600 rpm.

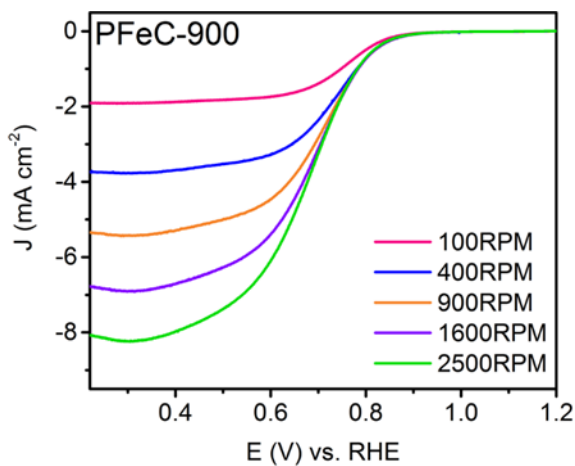


Figure 3.15 The polarization curves for PFeC-900 in O₂ saturated 0.5 M H₂SO₄ at rotation rates 100-2500 rpm

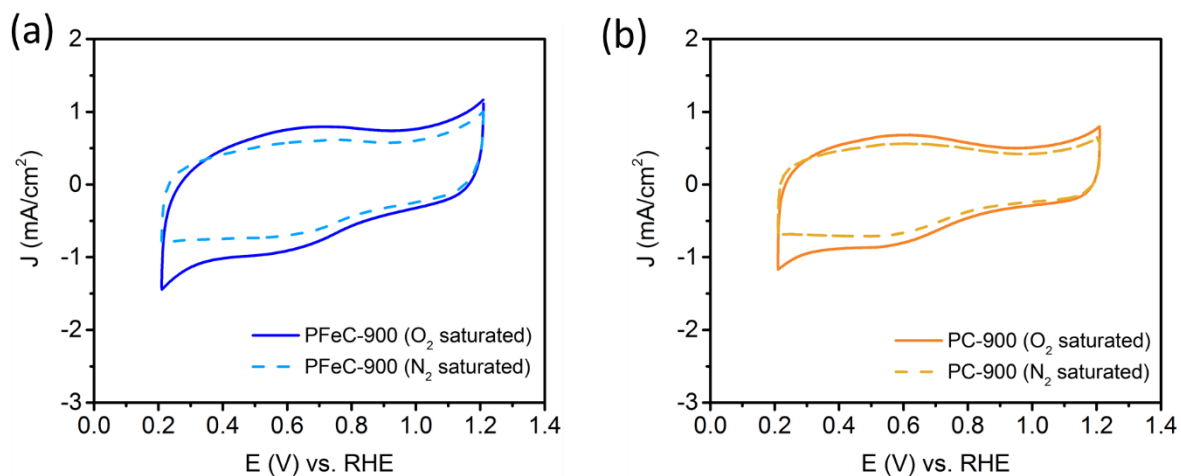


Figure 3.16 The CV of (a) PFeC-900. (b) Pt/C in N_2 and O_2 saturated $0.5 \text{ M H}_2\text{SO}_4$ using RDE at scan rate of 50 mV s^{-1} .

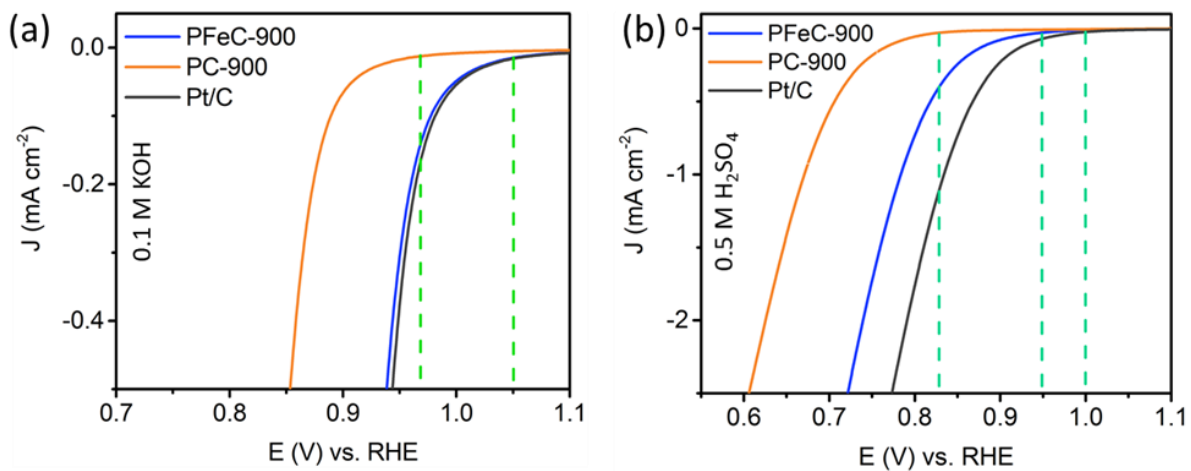


Figure 3.17 Comparison between onset potentials in O_2 saturated (a) 0.1 M KOH . (b) $0.5 \text{ M H}_2\text{SO}_4$ using RDDE at 1600 rpm and scan rate of 10 mV s^{-1} .

For practical application in fuel cells, the crossover effect of fuel should be considered because fuel molecules (e.g., methanol) may pass through the membrane from anode to cathode and poison the cathode catalyst. Therefore, developing fuel-tolerant catalysts is an important aspect of advancing the use of low-temperature fuel cells. In addition to the high activity and selectivity, PFeC-900 exhibits great durability. The chronoamperometric response of the PFeC-900 in 0.1 M KOH after 15 h shows only a 10% decay in comparison to 26% decay in the current for the commercially available Pt/C (Figure 3.18a). To study catalyst stability toward methanol oxidation, methanol (10 wt% 3 M) was injected into the electrolyte at 500 s, and its effect on the current was studied with $i-t$ chronoamperometry technique. Methanol gets oxidized instantly with Pt/C catalyst, but, in comparison, PFeC-900 shows a very good tolerance toward methanol oxidation (Figure 3.18b).

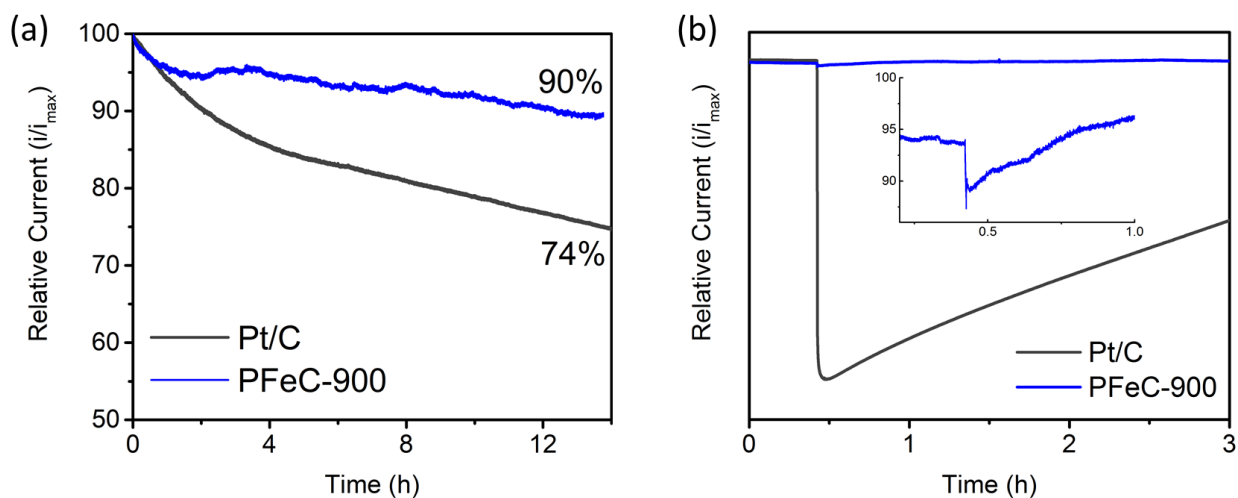


Figure 3.18 (a) Durability test. (b) Chronoamperometric response of PFeC-900 and Pt/C with the addition of 3 M methanol at 500 s at the rotation rate of 1600 rpm. The inset in panel b shows the behavior of PFeC-900 in the first hour.

Table 3.4 Comparison of preparation methods and ORR activities of reported phosphorus-doped, Iron phosphorous-doped electrocatalysts with PFeC-900 and PC-900 in 0.1 M KOH (Al.) medium or 0.1 M HClO₄ / 0.5 M H₂SO₄ (Ac.). (If the exact values are not mentioned in the paper, an estimated number from the corresponding graphs is used for this Table.)

Catalyst (given name)	Electrolyte	Onset Potential catalyst/Pt/C (V vs. RHE)	Half wave Potential catalyst/Pt/C (V vs. RHE)	Limiting Current Density (mA cm ⁻²)	Electron Transfer Number, n	Surface Area (m ² g ⁻¹)	Reference
PFeC-900	Al.	1.01/1.04	0.88/0.90	-7.29 RRDE	3.97	967	This work
PFeC-900	Ac.	0.95/1.0	0.71/0.77	-6.61 RRDE	3.98	967	
PC-900	Al.	0.95/1.04	0.79/0.88	-8.51 RRDE	3.88	1137	
PC-900	Ac.	0.81/1.0	0.6/0.77	-6.22 RRDE	3.5	1137	
Fe-P-C	Al.	0.95/0.97	~ 0.78	-5.01 RRDE	3.61	1371	
Fe-P-C	Ac.	0.84/~0.97	~ 0.6	-5.80 RRDE	3.8	1371	
GPF_e	Al.	0.93/0.96	~ 0.82	-6.72 RRDE	3.6	612.15	
GPF_e	Ac.	0.62/0.84	~ 0.5/0.8	-4.11 RRDE	3.84	612.15	
Fe₂P(3nm) @BC	Al.	0.96/0.97	0.82/	-5.18 RDE	3.9	314.9	
Fe₂P(3nm) @BC	Ac.	0.78/0.89	0.65/0.72	4.1 RDE	3.7	314.9	
FeP@PNC- 900	Al.	0.92/0.92	0.84/0.82	-5.50 RDE	4.1	724	32
P(Co)-C	Al.	~ 0.85/0.97	~ 0.75/0.82	~ -6.1 RRDE	3.79	1349	24
POMC-3	Al.	~ 0.87/0.92	0.74/0.78	~ -5.50 RDE	3.91	1182	33
FeP@NPC	Al.	ΔV= 15 mV	ΔV= 15 mV	-5.85 RDE	4	381	22
P-doped graphite/GC	Al.	~0.87/0.98	~0.72/0.85	-5.50 RDE	3	3986	34

3.4 conclusion

A simple synthetic route was developed to synthesize Fe₂P supported on highly porous P-doped carbon by the thermolysis of triphenylphosphine in the presence of ZnCl₂ and FeCl₂. PFeC-900 has demonstrated its high ORR activity in both alkaline and acidic solutions. The Fe₂P particles are well-defined and distributed in the P-doped porous carbon creating abundant active sites for ORR. The electrocatalytic activity of synthesized PFeC catalyst toward ORR in both electrolyte solutions showed competitive onset potential and ~ 4 electron transfer number. The catalytic system has superior long-term stability and was also found to be inert toward alcohol oxidation in contrast to commercially available Pt/C in an alkaline solution. The role of iron in the activity towards ORR was found to be crucial as the iron-leached sample, PC-900, showing negatively shifted onset and half-wave potential and a lower electron transfer number compared to the developed PFeC-900. Our work highlights the potential of combining electropositive phosphorus and iron in highly porous carbon for ORR applications using simple synthetic routes, which helps in addressing the use of scarce and expensive metals such as platinum in fuel cells.

References

- (1) Wang, W.; Jia, Q.; Mukerjee, S.; Chen, S. Recent Insights into the Oxygen-Reduction Electrocatalysis of Fe/N/C Materials. *ACS Catal.* **2019**, *9* (11), 10126–10141.
- (2) Steele, B. C. H.; Heinzel, A. Materials for Fuel-Cell Technologies. *Nature* **2001**, *414*, 345–352.
- (3) Gong, K.; Du, F.; Xia, Z.; Durstock, M.; Dai, L. Nitrogen-Doped Carbon Nanotube Arrays with High Electrolytic Activity for Oxygen Reduction. *Science* **2009**, *323* (5915), 760–764.
- (4) Oberlin, A. Carbonization and Graphitization. *Carbon N. Y.* **1984**, *22* (6), 521–541.
- (5) Singh, K. P.; Bae, E. J.; Yu, J. S. Fe-P: A New Class of Electroactive Catalyst for Oxygen Reduction Reaction. *J. Am. Chem. Soc.* **2015**, *137* (9), 3165–3168.
- (6) Ye, Y.; Duan, W.; Yi, X.; Lei, Z.; Li, G.; Feng, C. Biogenic Precursor to Size-Controlled Synthesis of Fe₂P Nanoparticles in Heteroatom-Doped Graphene-like Carbons and Their Electrocatalytic Reduction of Oxygen. *J. Power Sources* **2019**, *435*, 226770.
- (7) Fechler, N.; Fellingner, T. P.; Antonietti, M. “salt Templating”: A Simple and Sustainable Pathway toward Highly Porous Functional Carbons from Ionic Liquids. *Adv. Mater.* **2013**, *25* (1), 75–79.
- (8) Ashourirad, B.; Arab, P.; Islamoglu, T.; Cychosz, K. A.; Thommes, M.; El-Kaderi, H. M. A Cost-Effective Synthesis of Heteroatom-Doped Porous Carbons as Efficient CO₂ Sorbents. *J. Mater. Chem. A* **2016**, *4* (38), 14693–14702.
- (9) Gewirth, A. A.; Varnell, J. A.; Diascro, A. M. Nonprecious Metal Catalysts for Oxygen Reduction in Heterogeneous Aqueous Systems. *Chem. Rev.* **2018**, *118* (5), 2313–2339.
- (10) Thommes, M.; Kaneko, K.; Neimark, A. V.; Olivier, J. P.; Rodriguez-Reinoso, F.; Rouquerol, J.; Sing, K. S. W. Physisorption of Gases, with Special Reference to the Evaluation of Surface Area and Pore Size Distribution (IUPAC Technical Report). *Pure Appl. Chem.* **2015**, *87* (9–10), 1051–1069.
- (11) Lee, S. H.; Kim, J.; Chung, D. Y.; Yoo, J. M.; Lee, H. S.; Kim, M. J.; Mun, B. S.; Kwon, S. G.; Sung, Y. E.; Hyeon, T. Design Principle of Fe-N-C Electrocatalysts: How to Optimize Multimodal Porous Structures? *J. Am. Chem. Soc.* **2019**, *141* (5), 2035–2045.
- (12) Pampel, J.; Fellingner, T.-P. Opening of Bottleneck Pores for the Improvement of Nitrogen Doped Carbon Electrocatalysts. *Adv. Energy Mater.* **2016**, *6* (8), 1–8.

- (13) Seo, W.-G.; Matsuura, H.; Tsukihashi, F. Calculation of Phase Diagrams for the FeCl₂ PbCl₂ and ZnCl₂ Binary Systems by Using Molecular Dynamics Simulation. *Metall. Mater. Trans. B* **2006**, *37* (2), 239–251.
- (14) Liang, H. W.; Wei, W.; Wu, Z. S.; Feng, X.; Mullen, K. Mesoporous Metal-Nitrogen-Doped Carbon Electrocatalysts for Highly Efficient Oxygen Reduction Reaction. *J. Am. Chem. Soc.* **2013**, *135* (43), 16002–16005.
- (15) Li, D.; Baydoun, H.; Kulikowski, B.; Brock, S. L. Boosting the Catalytic Performance of Iron Phosphide Nanorods for the Oxygen Evolution Reaction by Incorporation of Manganese. *Chem. Mater.* **2017**, *29* (7), 3048–3054.
- (16) Sun, J.; Lee, H. W.; Pasta, M.; Yuan, H.; Zheng, G.; Sun, Y.; Li, Y.; Cui, Y. A Phosphorene-Graphene Hybrid Material as a High-Capacity Anode for Sodium-Ion Batteries. *Nat. Nanotechnol.* **2015**, *10* (11), 980–985.
- (17) Ma, G.; Xiang, Z.; Huang, K.; Ju, Z.; Zhuang, Q.; Cui, Y. Graphene-Based Phosphorus-Doped Carbon as Anode Material for High-Performance Sodium-Ion Batteries. *Part. Part. Syst. Charact.* **2017**, *34* (5), 1–7.
- (18) Sharifi, T.; Hu, G.; Jia, X.; Wagberg, T. Formation of Active Sites for Oxygen Reduction Reactions by Transformation of Nitrogen Functionalities in Nitrogen-Doped Carbon Nanotubes. *ACS Nano* **2012**, *6* (10), 8904–8912.
- (19) Hsu, L.-Y. Y.; Teng, H. Influence of Different Chemical Reagents on the Preparation of Activated Carbons from Bituminous Coal. *Fuel Process. Technol.* **2000**, *64* (1), 155–166.
- (20) Proctor, A.; Sherwood, P. M. A. A. X-Ray Photoelectron Spectroscopic Studies of Carbon Fibre Surfaces. I. Carbon Fibre Spectra and the Effects of Heat Treatment. *J. Electron Spectros. Relat. Phenomena* **1982**, *27* (1), 39–56.
- (21) Razmjooei, F.; Singh, K. P.; Bae, E. J.; Yu, J.-S. A New Class of Electroactive Fe- and P-Functionalized Graphene for Oxygen Reduction. *J. Mater. Chem. A* **2015**, *3* (20), 11031–11039.
- (22) Zhang, R.; Zhang, C.; Chen, W. FeP Embedded in N, P Dual-Doped Porous Carbon Nanosheets: An Efficient and Durable Bifunctional Catalyst for Oxygen Reduction and Evolution Reactions. *J. Mater. Chem. A* **2016**, *4* (48), 18723–18729.
- (23) Blanchard, P. E. R.; Grosvenor, A. P.; Cavell, R. G.; Mar, A. X-Ray Photoelectron and Absorption Spectroscopy of Metal-Rich Phosphides M₂P and M₃P (M = Cr-Ni). *Chem. Mater.* **2008**, *20* (22), 7081–7088.
- (24) Wu, J.; Yang, Z.; Li, X.; Sun, Q.; Jin, C.; Strasser, P.; Yang, R.; Strasser, P.; Yang, R. Phosphorus-Doped Porous Carbons as Efficient Electrocatalysts for Oxygen Reduction. *J. Mater. Chem. A* **2013**, *1* (34), 9889–9896.
- (25) Kwong, W. L.; Gracia-Espino, E.; Lee, C. C.; Sandstrom, R.; Wagberg, T.; Messinger, J. Cationic Vacancy Defects in Iron Phosphide: A Promising Route toward Efficient and Stable Hydrogen Evolution by Electrochemical Water Splitting. *ChemSusChem* **2017**, *10* (22), 4544–4551.
- (26) Billeter, E.; McGlamery, D.; Aebli, M.; Piveteau, L.; Kovalenko, M. V.; Stadie, N. P. Bulk Phosphorus-Doped Graphitic Carbon. *Chem. Mater.* **2018**, *30* (14), 4580–4589.
- (27) Kaviani, S.; Mohammadi Ghaleni, M.; Tavakoli, E.; Nejati, S. Electroactive and

- Conformal Coatings of Oxidative Chemical Vapor Deposition Polymers for Oxygen Electroreduction. *ACS Appl. Polym. Mater.* **2019**, *1* (3), 552–560.
- (28) Lee, B.; Kim, C.; Park, Y.; Kim, T.-G.; Park, B. Nanostructured Platinum/Iron Phosphate Thin-Film Electrodes for Methanol Oxidation. *Electrochem. Solid-State Lett.* **2006**, *9* (10), E27–E30.
- (29) Deng, C.; Zhong, H.; Li, X.; Yao, L.; Zhang, H. A Highly Efficient Electrocatalyst for Oxygen Reduction Reaction: Phosphorus and Nitrogen Co-Doped Hierarchically Ordered Porous Carbon Derived from an Iron-Functionalized Polymer. *Nanoscale* **2016**, *8* (3), 1580–1587.
- (30) Abdelmoaty, Y. H.; Tessema, T.-D. D.; Norouzi, N.; El-Kadri, O. M.; Turner, J. B. M. G. M.; El-Kaderi, H. M. Effective Approach for Increasing the Heteroatom Doping Levels of Porous Carbons for Superior CO₂ Capture and Separation Performance. *ACS Appl. Mater. Interfaces* **2017**, *9* (41), 35802–35810.
- (31) Fellingner, T. P.; Hasche, F.; Strasser, P.; Antonietti, M. Mesoporous Nitrogen-Doped Carbon for the Electrocatalytic Synthesis of Hydrogen Peroxide. *J. Am. Chem. Soc.* **2012**, *134* (9), 4072–4075.
- (32) Xu, X.; Shi, C.; Chen, R.; Chen, T. Iron Phosphide Nanocrystals Decorated in Situ on Heteroatom-Doped Mesoporous Carbon Nanosheets Used for an Efficient Oxygen Reduction Reaction in Both Alkaline and Acidic Media. *RSC Adv.* **2017**, *7* (36), 22263–22269.
- (33) Yang, D. S.; Bhattacharjya, D.; Inamdar, S.; Park, J.; Yu, J. S. Phosphorus-Doped Ordered Mesoporous Carbons with Different Lengths as Efficient Metal-Free Electrocatalysts for Oxygen Reduction Reaction in Alkaline Media. *J. Am. Chem. Soc.* **2012**, *134* (39), 16127–16130.
- (34) Liu, Z. W.; Peng, F.; Wang, H. J.; Yu, H.; Zheng, W. X.; Yang, J. Phosphorus-Doped Graphite Layers with High Electrocatalytic Activity for the O₂ Reduction in an Alkaline Medium. *Angew. Chemie- Int. Ed.* **2011**, *50* (14), 3257–3261.

Chapter 4

Heterogeneous Catalysis by Ultra-small Bimetallic Nanoparticles Surpassing Homogeneous Catalysis for Carbon-Carbon Bond Forming Reactions

4.1 Introduction

Catalytic processes that lead to cross-coupling bond formation are vital for many industrial applications and in particular the pharmaceutical industry where the synthesis of complex organic molecules is routinely encountered. Traditionally and since cross-coupling reaction is coined homogenous catalysts have played a dominant role.^{1,2} The remarkable high activity and selectivity of these homogeneous catalysts are tailored through the use of a variety of metals and organic ligands that modulate the electronic state of metal centers during catalytic cycles and render catalysts highly soluble in reaction media.³ Despite their high catalytic activity, homogeneous catalysts still face several challenges that hinder their wide and effective use in industrial processes. These challenges are high solubility which precludes catalysts recovery and reuse, product contamination, and high cost.⁴ Since the early 70s, a new group of supported metal center catalysts has been introduced^{5,6} with the hope that they will be able to match homogenous catalysts activity and address the shortcomings. Different morphologies of active metal centers have been studied as heterogeneous catalysts. This wide spectrum includes a macroscopic form

of Pd metal, such as Pd wire and sponge, all the way to metal nanoparticles deposited on a variety of supports. The superiority of metal NPs is inevitable.⁷⁻⁹ Various synthetic methodologies have enabled control over the composition, shape, and size of NPs, as well as methods for the preparation of supported NPs. Very interestingly, alloying Pd metal active centers with base metals affords bimetallic nanoparticles with superior catalytic properties compared to their monometallic counterparts because of the ability of base metals to donate charge to the Pd atoms.¹⁰⁻¹² Catalyst's support plays an important role in nanoparticle formation, size control, distribution, and stability. Some features of the support such as well distribution of surface functionality, high surface area, and pore size are all considered to contribute to the required role of the support.^{13,14}

In this chapter, we demonstrate the effective use of co-SEA in the preparation of ultra-small bimetallic nanoparticles from Pd and base metals Cu, Ni, and Co and report their remarkable catalytic activity in SCC reactions. The catalytic activity of the catalysts and the effect of alloying base metals with Pd toward SCC was investigated and show that CuPd/SiO₂ is superior to Pd/SiO₂ and the other bimetallic NPs achieving full biphenyl conversion in 30 minutes as opposed to three hours under the same conditions for monometallic Pd/SiO₂. Studying the recyclability and activity toward different derivatives confirmed the outstanding catalytic performance and stability of CuPd/SiO₂. The high turnover frequency for all catalysts, especially CuPd/SiO₂, with turn over frequency of 248000 attests to its superior activity.

4.2 Experimental Section

4.2.1 Materials and Preparation of Silica Supported Bimetallic Nanoparticles

Amorphous fumed silicon (IV) oxide, (Alfa Aesar, surface area 350-420 m² g⁻¹) was used without any further modification. Copper (II) nitrate trihydrate (Sigma Aldrich, 98.0-103%), nickel (II) nitrate hexahydrate (Alfa Aesar, 98%), cobalt (III) nitrate hexahydrate (J.T. Baker, 99.1%), and tetraamminepalladium (II) nitrate solution in 10 wt% H₂O (Sigma Aldrich). 20000 ppm stock solutions of base metal salts were prepared using 5 N NH₃ solution. The total volume of the solution used for SEA studies was calculated to yield a surface loading of 1000 m²L⁻¹ (Eq. 4.1), where surface loading (SL, m²L⁻¹), surface area (SA, m² g⁻¹), the mass of the support (g) and total volume of the solution (L) are used. The intended weight loading of the metal stock solution was pipetted into the support solution and stirred for 30 min; this allows the cationic metal precursor to adsorb. The solution containing deposited metal salt on the surface of fumed silica is centrifuged in water and then EtOH to replenish the basic solution. The samples are air-dried overnight at ambient conditions followed by drying in an oven for four h at 120 °C. The samples are reduced under a flow of 5% H₂ (in Argon) at 400 °C in a tube furnace one h.

$$SL = \frac{SA * mass\ of\ the\ support}{Volume} \quad (4.1)$$

4.2.2 Instrumentation

Inductively coupled plasma optical emission spectrometry (ICP-OES) was used to measure the bulk composition of metals. Temperature Programmed Reduction (TPR) profiles were measured by a Micromerics AutoChem II coupled with a Thermal

Conductivity Detector (TCD) in a quartz U-tube to examine the reduction temperatures of the metals. Powder X-ray diffraction (PXRD) was examined with X-ray diffraction patterns collected at room temperature using a PANalytical X'Pert PRO Multipurpose Diffractometer (MPD). The samples were mounted on a zero-background sample holder measured in transmission mode using Ni-filtered Cu K α radiation (operated at 40 kV, 45 mA; $\lambda = 0.15418$ nm), the diffraction angle ranging from 10° to 80° with a step size of 0.07878° and a rate of 4.67° min⁻¹. X-ray photoelectron spectroscopy (XPS) analysis was performed on a PHI VersaProbe III Scanning XPS Microprobe employing a monochromatic, micro-focused, scanning x-ray source equipped with a hemispherical analyzer and argon gun. Samples for XPS measurements were prepared by pressing the specimen into a piece of double-sided tape, which was then mounted onto the sample holder. During XPS analysis, a combination of a low-energy electron flood gun and an argon ion flood gun was utilized for charge compensation. For some samples, the Ar gun was also used to sputter ~10 nm from the top of the samples with a rate of 2 nm min⁻¹ before performing XPS analysis. The binding energy scale was calibrated by setting the Si 2p peak at 103.5 eV. The XPS results were analyzed with the CasaXPS software (v4.84). High Resolution Transition Electron Microscopy (HR-TEM) was performed using a FEI Titan 300 kV equipped with a Gatan 794 Multi-Scan Camera, a HAADF-STEM detector. Samples were drop-casted on carbon-coated grids (Ted Pella, Inc.) and left to dry overnight at room temperature. Captured images were processed using ImageJ software. Gas chromatography - flame ionization detector (GC-FID) has been used to analyze the SCC reactants and products. An Agilent 6890N GC equipped with an Agilent J&W GC HP-

5MS capillary column was used in conjunction with an FID detector. 4 μ l of samples were injected with a microsyringe.

4.2.3 Suzuki Cross-coupling reaction at room temperature and pressure condition

Pd-supported catalysts (Pd: 1.05 μ mol, 0.3 mol%) were added to and dispersed in a glass vial with 2 mL of ethanol and 2 mL of deionized (DI) water. Bromobenzene (50 mg, 0.32 mmol, 1 equiv) along with benzenboronic acid (47 mg, 0.38 mmol, 1.2 equiv), and potassium carbonate (133 mg, 0.96 mmol, 3 equiv) was added to the solution. The reactions were performed at room temperature (RT) and atmospheric pressure with continuous stirring until completion or after 3 hours. For the duration of the reaction, small aliquots were collected at regular intervals to monitor product formation. The biphenyl product was extracted with ethyl acetate via centrifugation and the progression of the reaction was monitored by GC–FID.

4.2.4 Suzuki Cross-coupling Reaction at Microwave reaction condition

Pd-supported catalysts (Pd: 1.05 μ mol, 0.3 mol%) were added to and dispersed in a microwave reaction vessel with 2 mL of ethanol and 2 mL of deionized (DI) water. Bromobenzene (50 mg, 0.32 mmol, 1 equiv) along with benzenboronic acid (47 mg, 0.38 mmol, 1.2 equiv), and potassium carbonate (133 mg, 0.96 mmol, 3 equiv) was added to the solution. The vessels were sealed and heated at 60 °C for 5 min under MWI. After the reactions were completed, aliquots were collected, and the reaction yield was monitored as described above. SCC reactions for different derivatives of the reactants and the recyclability of the catalyst were studied under MWI reaction condition. For recycling catalysts, after the reaction was completed, the catalyst was collected by centrifugation,

washed thoroughly 3 times with DI water and 3 times with ethanol, and then dried at 80 °C overnight. The dried catalyst was used for the consecutive run using aforementioned method. A small aliquot of sample was collected after each run to analyze with GC-FID to monitor the conversion. After each run, a small amount of catalyst was used for ICP analysis.

4.3 Results and Discussions

4.3.1 Catalysts Preparation and Characterization

Given the effectiveness and versatility of co-SEA in bimetallic nanoparticle preparation, it was employed to prepare the catalysts. The SEA method depends on the ionic attraction forces between the precursor ions and the surface charge of the support. The point of zero charge (PZC) is the fundamental surface characterization governing SEA, and the surface charge of the support can be adjusted by altering the pH of the solution containing the support. For pH values above PZC the hydroxyl groups on the surface of silica become deprotonated and hence negatively charged, and for pH values below PZC the hydroxyl groups become protonated and positively charged. For pH values near the support's PZC, minimal or no precursor-support interaction occurs, hence the uptake strongly depends on the pH.¹⁵ Adsorption of metal complexes is an electrostatic interaction, which can be described as physical adsorption, since no ion exchange or chemical reaction takes place during SEA.^{16,17} The fumed silica used in this study has a PZC of 3.6 in line with other silica-supported reported in literature.^{14,18-20} The SEA process was initiated by dispersing the silica support in MQ water and then the pH of the solution was adjusted to 11.8 using 5 N NH₃ to optimize electrostatic adsorption.¹⁴ As the pH increases, the native hydroxy groups of the surface become deprotonated. It is worth mentioning that the addition of excess base results in lower adsorption, as metal precursors are shielded from the surface charge due to high ionic strength which according to kinetic studies diminishes the adsorption equilibrium constant and results in a phenomenon known as the double-layer screening effect.¹⁵ High pH values above 12 also known to disintegrate silica support.

While the silica solution is continuously stirred, the intended weight loading of the metal stock solution is pipetted into the support solution, allowing the cationic metal precursor to adsorb, and the solution is further stirred for 30 minutes. Following the deposition, the solution is centrifuged to replenish the basic solution, the sample is air-dried overnight, oven-dried at 120 °C for four h and then reduced under a flow of 5% H₂ (in argon) at 400 °C for one hour using a tube furnace. Because the precursor ions are only physically adsorbed on the surface of the support, the metal nanoparticles are expected to be in the ground state after reduction with H₂. Four monometallic catalysts were prepared by SEA, namely Cu/SiO₂, Co/SiO₂, Ni/SiO₂, and Pd/SiO₂. The co-SEA was used to synthesize bimetallic catalysts where positively charged precursor ions of the two metals are introduced in the solution simultaneously. These ions participate in competitive physical adsorption on the silica surface. To investigate the impact of base metal alloying on catalytic activity, three bimetallic catalysts were synthesized by the co-SEA method; CuPd/SiO₂, NiPd/SiO₂, and CoPd/SiO₂ (Fig. 4.1). Furthermore, the most active catalytic system CuPd/SiO₂ was optimized by varying the Pd content in Cu matrix: 0.5Cu1Pd/SiO₂, 1Cu0.5Pd/SiO₂, and 2Cu1Pd/SiO₂. While the latter has a similar Cu/Pd ratio to 1Cu0.5Pd/SiO₂, it was prepared with the intention to maximum catalyst loading by saturating the surface of the support (complete monolayer coverage) with [Cu(NO₃)₂]²⁺ and [Pd(NO₃)₂]²⁺. As such, this comparison could help in identifying the minimum amount of Pd needed for optimum catalytic activity.

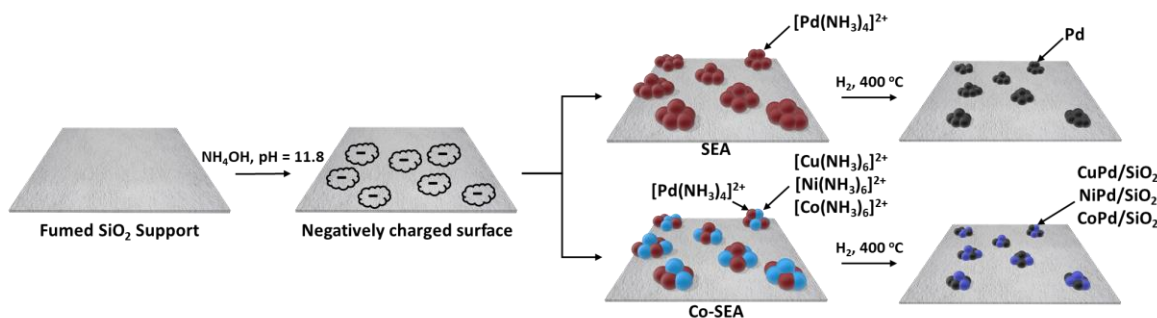


Figure 4.1 SEA and Co-SEA reaction schematic.

4.3.2 Catalysts Characterization

For mono and bimetallic catalysts, the comparison between targeted weight loading and the final bulk composition of each metal in wt % was measured by ICP-OES. Close agreement between intended wt % and bulk composition for bimetallic catalysts suggest that the simultaneous adsorption of metal ions during co-SEA is not affected by their different competitive adsorption at low weight loading of 1 wt % (Table 4.1 and Table 4.2). The amount of metal adsorbed on the surface of the support by the SEA method depends on its surface area known as adsorption density ($\mu\text{mol m}^{-2}$).²¹ This defines the maximum ability of metal adsorption (μmol) on the support surface area (m^2). Other studies have also concluded that in similar bimetallic complexes, for a complete monolayer coverage, maximum adsorption of 1.0 to 1.3 $\mu\text{mol m}^{-2}$ can be achieved.¹⁴ According to our ICP analysis, it is clear that for all the catalysts more than 85% of the metals were adsorbed on the support surface. In comparison with the monometallic catalysts, metals adsorption in bimetallic catalysts also maintains a close correlation between the targeted and the actual weight loading according to ICP data. ICP measurements were performed on the catalysts

used for the recycling test, Pd/SiO₂ and CuPd/SiO₂. The findings help identify the vulnerability of the catalyst toward leaching and the effects on the activity of the catalysts. After each run of the recycling, the catalysts were collected, washed and underwent ICP analysis, to find out if any metal has leached back into the solvent during the reaction. From the data collected by ICP, shown in table 3, it is apparent that for the Pd/SiO₂ sample only 3 % of Pd has leached away throughout the entire 6 recycle runs (Table 4.3). The CuPd/SiO₂ catalyst does not lose much Pd (0.04 wt %) throughout the first 4 recycling runs. The high stability of the catalyst is one of the advantageous of base metal alloying.²² The amount of leached Pd increases to 26% by the end of the 7th recycling run. In contrast, 19% of Cu is leached from the surface after the first run, and then during the following consecutive runs, the amount of Cu does not change significantly (Table 4.4). The loss of Cu during the first run may be explained by the leaching of some Cu particles not adsorbed on the surface of the support strongly. However, as the Cu remains consistent throughout the rest of the recyclability runs, it can be assumed that the rest of the Cu was adsorbed strongly and thus the amount of Cu does not change much during the consecutive runs.

Table 4.1 Bulk composition of metals for mono and bimetallic samples collected by ICP-OES. (BM stands for base metal)

Catalyst Name	Targeted weight loading (wt%)		Adsorbed Metal (%)		Actual weight loading (wt%)		Catalyst Denomination
	BM	Pd	BM	Pd	BM	Pd	
Cu/SiO ₂	1		99		0.99		0.99 Cu
Co/SiO ₂	1		86		0.86		0.86 Co
Ni/SiO ₂	1		99		0.99		0.99 Ni
Pd/SiO ₂		1		96		0.94	0.94 Pd
CuPd/SiO ₂	1	1	97	97	0.97	0.97	0.97 Cu 0.97 Pd
CoPd/SiO ₂	1	1	88	87	0.88	0.87	0.88 Co 0.87 Pd
NiPd/SiO ₂	1	1	85	86	0.85	0.86	0.85 Ni 0.86 Pd

Table 4.2 Bulk composition of various metal loading for Cu-Pd combination collected by ICP- OES

Sample Name	Targeted weight loading (wt%)		Adsorbed Metal (%)		Actual weight loading (wt%)		Catalyst Denomination
	BM	Pd	BM	Pd	BM	Pd	
CuPd/SiO ₂	1		97	97	0.97	0.97	0.97 Cu 0.97 Pd
2Cu1Pd/SiO ₂	2	1	89	95	1.78	0.95	1.78 Cu 0.95 Pd
0.5Cu1Pd/SiO ₂	0.5	1	98	95	0.49	0.95	0.49 Cu 0.95 Pd
1Cu0.5Pd/SiO ₂	1	0.5	97	99	0.97	0.99	0.97 Cu 0.97 Pd

Table 4.3 Bulk composition of metals for Pd/SiO₂ catalyst after each recycling run.

Run	Metal Concentration (wt.%)
	Pd
1	0.96
2	0.95
3	0.93
4	0.93
5	0.93

Table 4.4 Bulk composition of metals for CuPd/SiO₂ catalyst after each recycling run.

Run	Metal Concentration (wt.%)	
	Cu	Pd
1	0.97	0.97
2	0.78	0.95
3	0.77	0.94
4	0.77	0.93
5	0.76	0.86
6	0.76	0.75
7	0.74	0.71

TPR was performed and the bimetallic samples were compared with their monometallic counterparts. The TPR profile of monometallic Pd/SiO₂ shows a reduction peak at 190 °C (Fig. 4.2a) and Cu/SiO₂ shows a peak at 250 °C with a broad shoulder starting at 480 °C (Fig. 4.2a). It is expected that Cu²⁺ was reduced to metallic Cu⁰ directly and there is no transient stage. The presence of complexes with higher reduction temperatures attests to their stronger interaction with the support.¹⁴ For the bimetallic CuPd/SiO₂, a sharp peak at 190 °C and a smaller peak at 365 °C is present. The first peak can be assigned to the reduction of Cu-Pd alloyed NPs, and the second, much smaller, peak corresponds to the metallic Cu reduction shoulder with a ~100 °C shift towards lower reduction temperatures. This shift is due to the hydrogen spillover from Pd species to the remaining unreduced Cu confirming the proximity of Pd and Cu atoms on the support surface (Fig. 4.2a).¹⁴ The TPR profile of Ni/SiO₂ shows a broad peak centered at 510 °C corresponding to the reduction of Ni complex (Fig. 4.2b). In contrast, NiPd/SiO₂ shows two sharp peaks at 170 °C and 315 °C, corresponding to the reduction of bimetallic alloyed Ni-Pd complexes and the shifted monometallic Ni complexes respectively (Fig. 4.2b). The TPR profile of CoPd/SiO₂ also shows two peaks, a sharp peak at 178 °C and a small peak at 328 °C, while the monometallic Co/SiO₂ also has two peaks but at much higher temperatures of 463 °C and 775 °C. These peaks can be assigned to the reduction of Co³⁺ to Co²⁺ and another due to the reduction of Co²⁺ to metallic Co⁰.²³ Low metal loading for Co causes these two peaks to merge. The reduction temperatures for bimetallic CoPd/SiO₂ follows the same pattern as the other bimetallic samples (Fig. 4.2c). Overall, the TPR profiles of bimetallic NP samples exhibit temperature shifts induced by the presence of Pd

in close proximity to the base metal as well as the effect of hydrogen spillover on the reduction temperatures which validate the intimacy of the alloyed NPs.

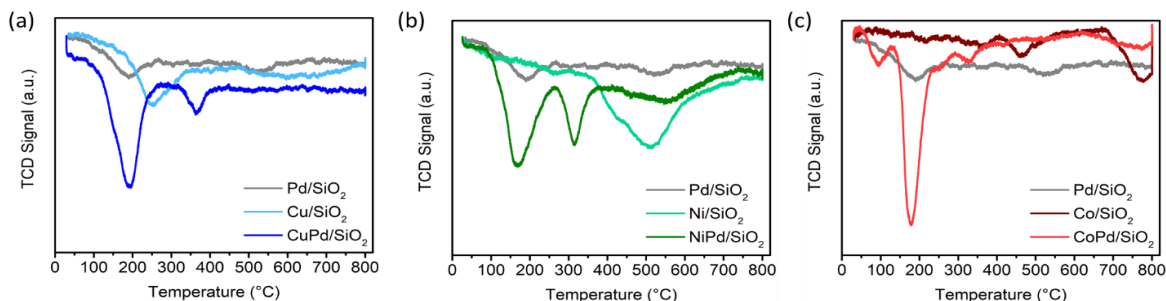


Figure 4.2 TPR patterns for (a) Pd/SiO₂, Cu/SiO₂, and CuPd/SiO₂, (b) Pd/SiO₂, Ni/SiO₂, and NiPd/SiO₂, and (c) Pd/SiO₂, Co/SiO₂, and CoPd/SiO₂.

The XRD patterns for the mono and bimetallic catalysts are shown in Figure 4.3a. There are no distinguishable characteristic peaks present for any of the catalysts. The hump present at $\sim 22^\circ$ for all the samples is characteristic of the amorphous structure of SiO₂.^{18,20} The absence of any other peaks indicates that ultra-small particles have formed and no signs of particles aggregation as typically XRD has a 2-2.5 nm size limit.²⁴ XRD analysis was also performed on recycled CuPd/SiO₂ as shown in figure 4.3b. The SiO₂ amorphous hump $\sim 22^\circ$ is prominent for all the recycled samples, and no other distinguishable peaks are noticed; a very small hump starts to appear at $\sim 40^\circ$ from 3rd run of the recycled catalyst. This hump is correlated to the Pd (111) plane.²⁵⁻²⁷ The small and broad nature of the peak instead of a sharp peak may suggest that while the metallic nanoparticles start to aggregate in the recycled catalyst, the size of the particle is still smaller than 2.5 nm, the particle size is further discussed in TEM section. The same trend is also noticed on the XRD patterns

of the recycled Pd/SiO₂ catalyst in Figure 2b, though the hump at ~40° starts to appear after the 1st cycle. The hump, in this case, is also very small and broad which shows that the Pd particles are still very small. Most importantly, for the CuPd/SiO₂ catalyst, the hump does not appear until after the 3rd recycle which implies that the Cu-Pd alloying is playing a role in preventing the Pd from aggregating.

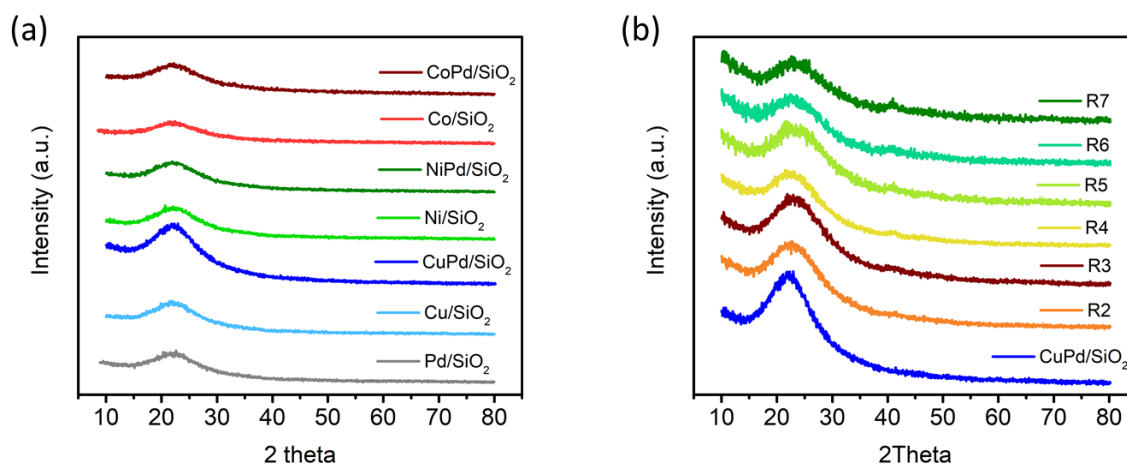


Figure 4.3 (a) XRD patterns for all mono and bimetallic catalysts. (b) XRD patterns for pristine CuPd/SiO₂ and consecutive recycling test catalysts.

XPS has also been performed on all of the catalysts. The surface composition of silicon and oxygen is reported in Table S4. The silica support shows a single peak at 103.5 eV for the Si 2p spectra (Fig. 4.4b), and a single peak at 532.9 for O 1s spectra (Fig 4.4c).²⁸ The fitted/assigned peaks for Si and O and their corresponding elemental composition (at%), reported in figure 4.4, suggest that exposure to the 5N ammonium hydroxide solution does not affect the chemical composition of the surface of silica. The deconvolution of the Cu 2p_{3/2} spectra shows a single peak at 933.1 eV for the monometallic

sample, Cu/SiO₂, and a single peak at 933.2 eV for the bimetallic CuPd/SiO₂. This 0.1 eV shift for the bimetallic sample corresponds to the alloying of the two metal species (Fig. 4.4d). It is also known that any small shift from metallic Copper with a binding energy of 932.8^{29,30}, may also be induced by surface oxidation. Copper (I) oxide and copper (II) oxide have a binding energy of 933.0 and 933.5 eV respectively, making the differentiation between the metallic species and the Cu⁺ challenging.³¹ For all samples, the low content of the metals and their ultra-small particle size results in low intensities. In the case of Co 2p_{3/2} spectra, the monometallic, Co/SiO₂ has a very weak peak at 783.0 eV, which has the closest correlation to Co²⁺.^{32,33} No peaks in the Co 2p spectra for the bimetallic sample can be detected (Fig. 4.4e). The deconvolution of Ni 2p_{3/2} spectra shows a peak at 856.2 eV and a satellite hump at 861.8 eV for the monometallic Ni/SiO₂. The bimetallic sample, NiPd/SiO₂, shows a peak at 856.5 eV and a satellite peak at 861.7 eV can also be fitted (Fig. 4.4f).³⁴ The 0.3 eV shift for the bimetallic sample in comparison to Ni/SiO₂, indicates a potential shift in electron cloud distribution for the Ni-Pd alloy, suggesting that Ni atoms carry more negative charge and consequently the Pd atoms carry a more positive charge. This phenomenon has the potential to hamper the desired Pd⁰ state, essential for catalytic activity. As the comparison between the transition metal species in bimetallic samples suggests, the deconvoluted Copper spectra for those samples more closely correlates with metallic Copper, which can play a significant role in the catalytic activity for the cross-coupling reactions. The deconvolution of Pd 3d spectra in figure 4.4g, characterized by spin-orbital splitting (Pd 3d_{5/2} and Pd 3d_{3/2}) shows two peaks at 335.6 eV and 340.3 eV for the bimetallic CuPd/SiO₂ sample which can both be assigned to the Pd⁰ state³⁵; 336.1 eV

and 341.9 eV are the corresponding peaks for CoPd/SiO₂ and 336.1 eV and 341.2 eV are the corresponding peaks for NiPd/SiO₂. Interestingly, the Pd atoms in CuPd/SiO₂ have average binding energies closer to the metallic Pd at 334.8-335.4 eV and 340.1-340.7 eV.³⁵⁻³⁷ Chemical shifts in the range of 0.4-0.7 can also be traced back to the strong interaction between the Pd 3p core level and the base metal.³⁵ It has also been reported that Cu may strongly modify the Pd valance shell through electrons being injected into the sp orbital. The solution containing deposited metal salt on the surface of fumed silica is centrifuged to replenish the basic solution before drying. on the other hand, the binding energy of Pd atoms alloyed with Co and Ni correlates better with the Pd²⁺ species with the binding energy of 336.7 eV, which can be traced back to possible to surface oxidation or shifts in electron cloud distribution, either would affect the catalytic activity of those samples.³⁸ In the case of monometallic Pd/SiO₂, a peak at 336.3 eV and a peak at 341.6 eV can be deconvoluted. The positive shift towards higher energies and a closer correlation with Pd²⁺ binding energy, highlights the important role base metals play in keeping the catalytically active Pd, at zero oxidation state, intact throughout the cross-coupling experiments and even general handling. In order to study the effects of each cross-coupling experiment on CuPd/SiO₂, the catalysts after the 3rd and 6th run were chosen to investigate the changes in the intimacy of the alloy and their binding energies. Deconvolution of Cu 2p spectra, for both the 3rd and 6th experiment, shows a single peak at 933.2 eV (Fig. S2d). This finding indicates that copper atoms maintain their integrity without going through any surface changes. In the case of the Pd 3d spectra, the 3rd run peaks at 336.0 eV and 341.1 eV are deconvoluted, and the 6th run peaks at 336.7 eV and 341.6 eV indicate a shift

towards higher binding energies suggesting the Pd atoms are becoming more positively charged and therefore less active (Fig. 4.4g). The ability to reach full conversion in cross-coupling reaction even after the 6th run can be traced back to the well-alloyed Cu-Pd catalysts.

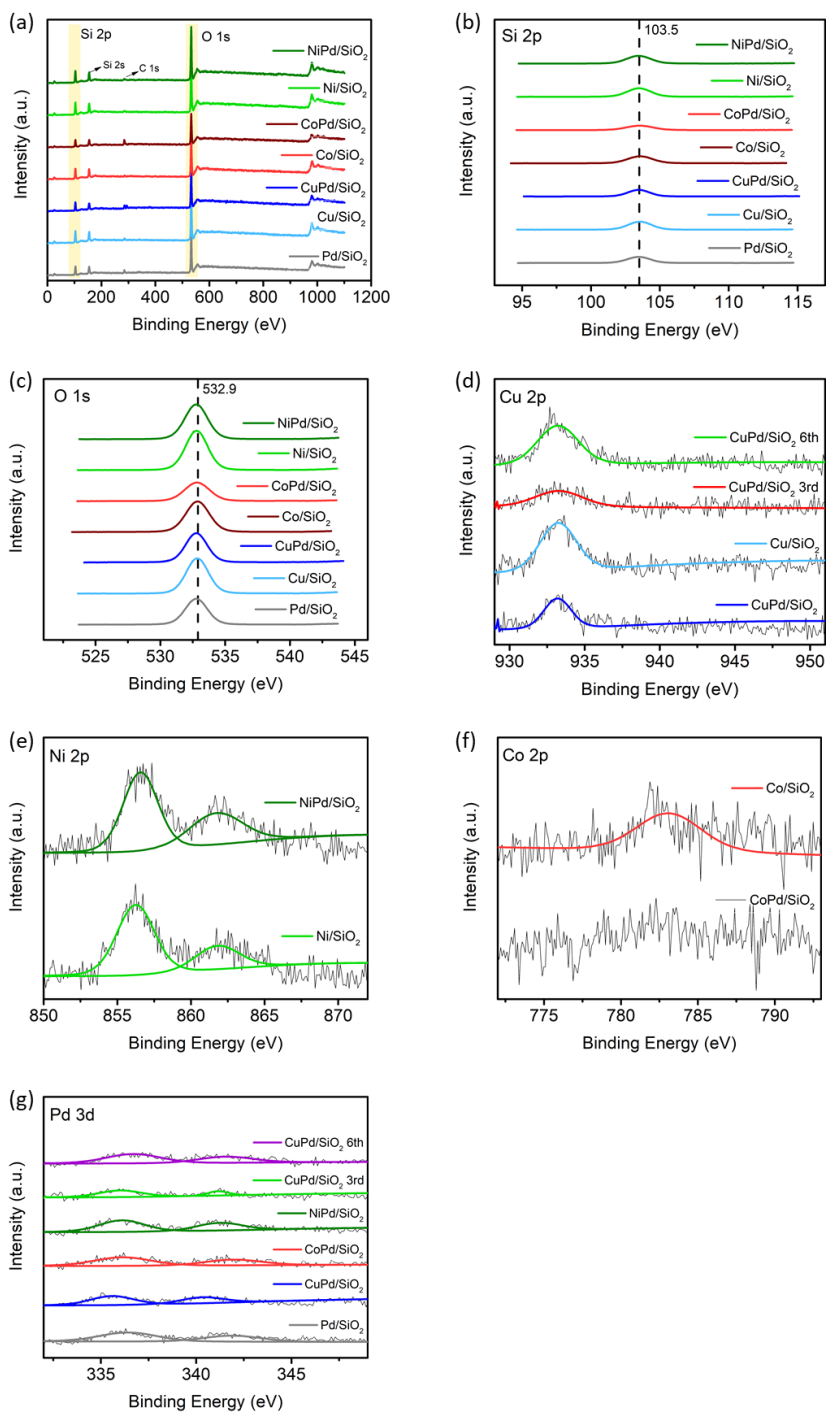


Figure 4.4 XPS spectra of all bimetallic and monometallic samples (a) Survey spectra (b) Deconvoluted Si 2p spectra, (c) Deconvoluted O 1s spectra, (d) Deconvoluted Cu 2p spectra, (e) Deconvoluted Ni 2p spectra, (f) Deconvoluted Co 2p spectra, (g) Deconvoluted Pd 3d spectra.

Table 4.5 Surface composition of mono and bimetallic samples. Collected with XPS.

Sample Name	Silicon (At%)	Oxygen (At%)
Cu/SiO₂	40.27	59.73
Co/SiO₂	40.03	59.97
Ni/SiO₂	39.83	60.17
Pd/SiO₂	36.92	63.08
CuPd/SiO₂	37.07	62.93
CoPd/SiO₂	39.60	60.40
NiPd/SiO₂	38.65	61.35

Table 4.6 Surface composition of CuPd/SiO₂ and the 3rd and 6th recycled catalysts. Collected with XPS.

Sample Name	Silicon (At%)	Oxygen (At%)
CuPd/SiO₂	37.07	62.93
CuPd/SiO₂ 3rd	39.76	60.24
CuPd/SiO₂ 6th	39.43	60.57

HRTEM and STEM images were collected and analyzed to determine the metal nanoparticle size and distribution. It is clear from the particle size analysis that all samples have active metal particle sizes in the 0.7-2.3 nm range (Fig. 4.5). The particle size distribution is narrow for all samples. Of particular interest, is that the addition of a transition metal along with Pd did not change the particle size significantly. This is because the SEA prevents more than a monolayer coverage of metal ion deposition as it only depends on the surface charge and after a monolayer of deposition the reduced effect of the surface charge prevents agglomeration. Thus, upon reduction of the physically adsorbed precursors, larger nanoparticles are more difficult and less likely to form. This finding is in agreement with the absence of any peaks in the XRD plots as even small particles can result in broad peaks with very low intensity and that only becomes apparent after a few consecutive recycling experiments. Smaller particles also have a higher exposed surface area per particle which should result in a higher catalytic activity compared to bigger particles.

HRTEM analysis of the CuPd/SiO₂ catalyst studied for recyclability was performed on the 4th and 6th recycling runs to examine the integrity of the catalyst and any changes that might take place on average particle size (Fig. 4.6). The particle size analysis shows that there is almost no change in the average particle size during the recycling runs which indicates a strong catalyst-support interaction and the superior sustainability of a well alloyed Cu-Pd catalyst. The strong interaction with the silica support achieved by the co-SEA method protects the active metal particles from sintering.

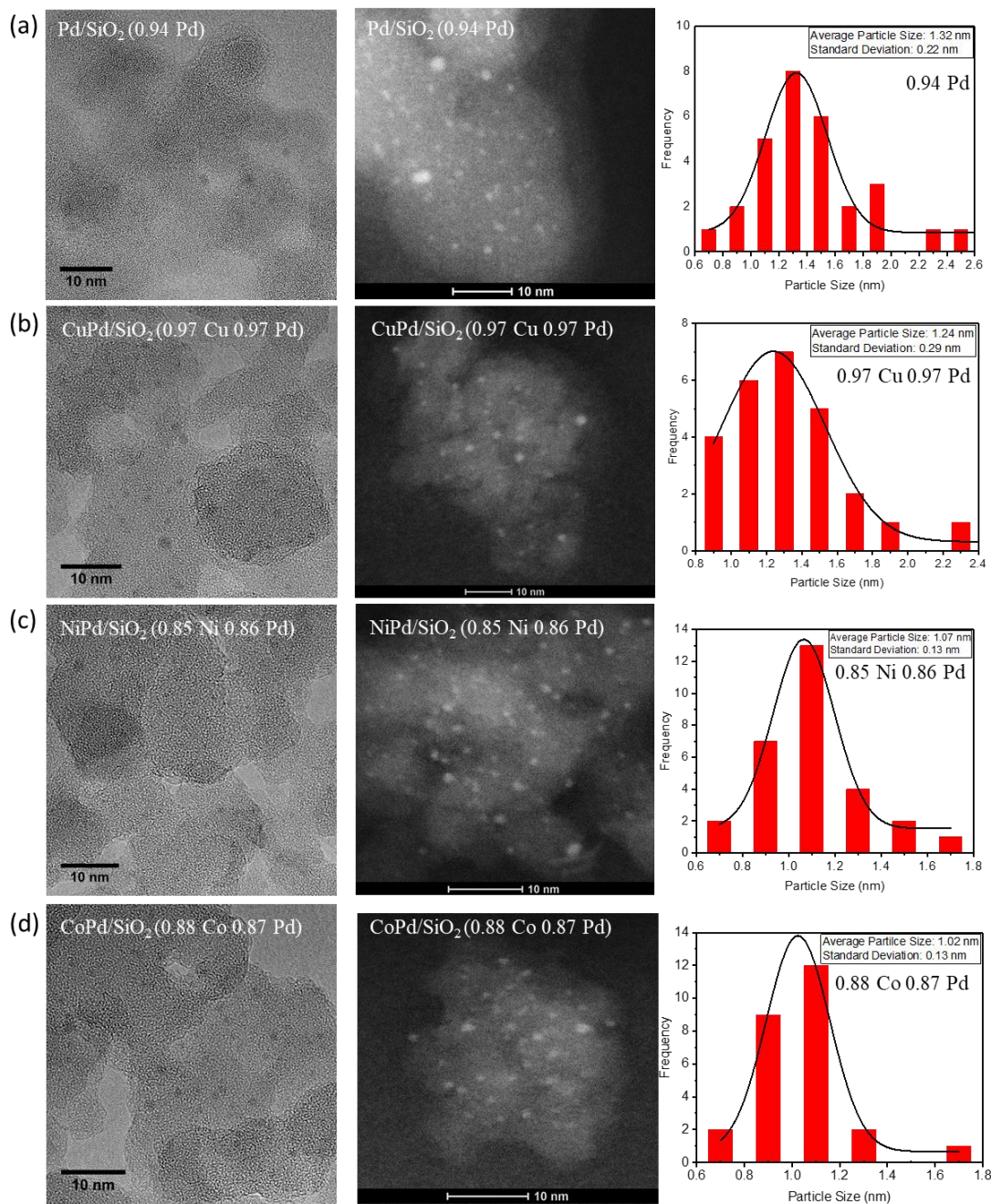


Figure 4.5 HRTEM, STEM, and the corresponding particle size distribution for (a) Pd/SiO₂, (b) CuPd/SiO₂, (c) NiPd/SiO₂ and (d) CoPd/SiO₂.

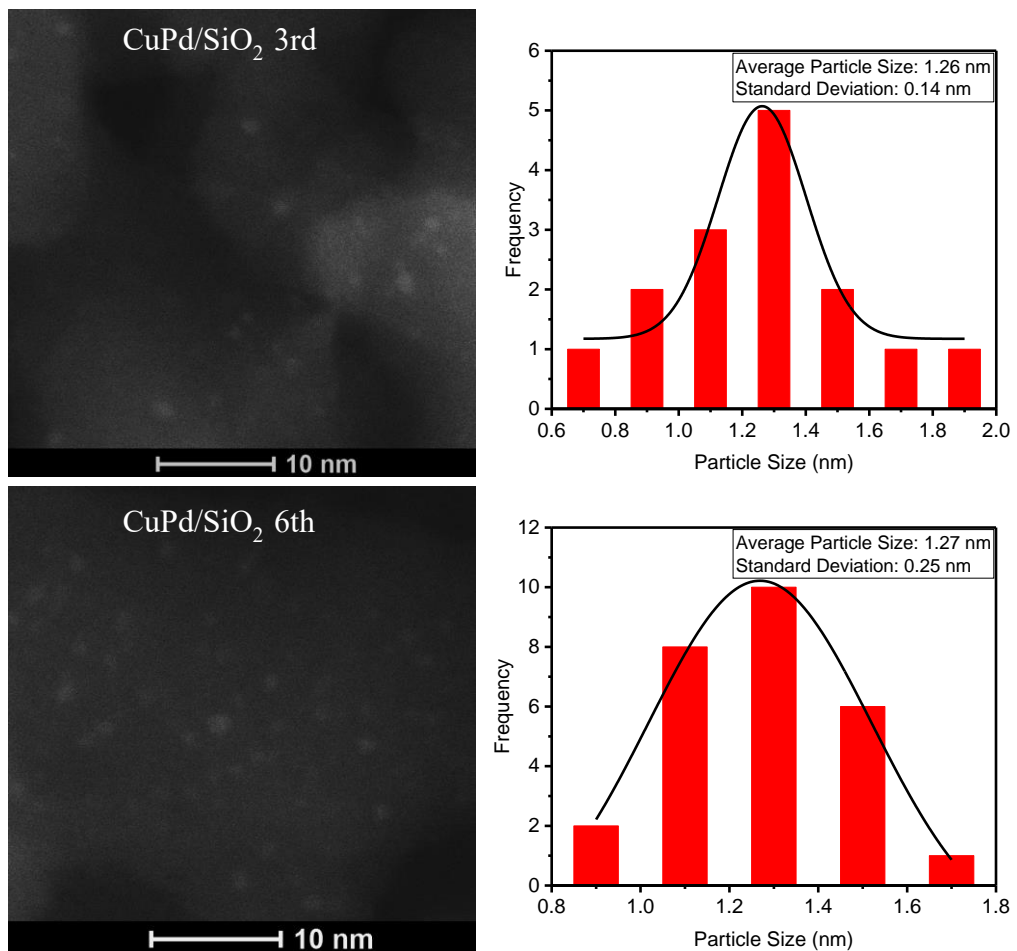


Figure 4.6 HRTEM, STEM and the corresponding particle size distribution for (a) CuPd/SiO₂ 3rd, (b) CuPd/SiO₂ 6th recycled runs.

4.4 Suzuki cross-coupling catalytic performance

The aforementioned monometallic and bimetallic catalysts were studied for SCC reactions at room temperature (RT). Among all catalysts, CuPd/SiO₂ shows superior activity reaching a biphenyl conversion of 35% after one minute and a full conversion in only 30 minutes under ambient conditions (Fig. 4.7a). This result surpasses all the other bimetallic catalysts and the monometallic Pd catalyst, which reaches full conversion after three hours (Fig. 4.7a). The second-best sample, NiPd/SiO₂, reaches a biphenyl conversion of 18% after one minute and a full biphenyl conversion in 90 minutes. On the other hand, dilution of Pd in a Co matrix does not seem to enhance the catalytic activity when compared to the other bimetallic catalysts and has similar activity to Pd/SiO₂; it required three hours to perform the full biphenyl conversion. Catalysts composed of the monometallic base metals were found to be inactive towards the SCC reaction at RT. The superior activity of the Cu-Pd alloyed system encouraged us to investigate the impact of Cu/Pd ratio on catalytic activity. These samples are named using the targeted metal loading the loading calculated from the ICP measurement is reported in table S1. To study the effect of Pd dilution in Cu matrix, 0.5Cu1Pd/SiO₂, 1Cu0.5Pd/SiO₂, and 2Cu1Pd/SiO₂ were synthesized. Even though 2Cu1Pd/SiO₂ has a similar Cu/Pd ratio as 1Cu0.5Pd/SiO₂, this sample was prepared by saturating the support surface with metal ions for complete monolayer coverage formation.¹⁴ The biphenyl conversion yields from the SCC reaction show that the dilution of 1 wt% Pd in various Cu loadings of 0.5, 1 to 2 wt%, in 0.5Cu1Pd/SiO₂, CuPd/SiO₂, and 2Cu1Pd/SiO₂ respectively, has almost no effect on the overall catalytic activities, with all the catalysts achieving 100% biphenyl conversion in 30 min (Fig. 4.7b).

Lower loading of Pd, investigated by 1Cu0.5Pd/SiO₂ catalyst, required almost 90 min to reach the full conversion. Few catalyst characteristics stand out among those in which superior catalytic activity is traced back to. Small nanoparticles, narrow size distribution, particle distribution on the support, and base metal alloying are among those characteristics of well-performing catalysts. Smith et al. reported that agglomerated but small CuPd nanoparticles with an average size of 4.5, achieved TOF of 72000, and performed well for various cross-coupling reactions tracing the activity back to the larger surface to volume ratio with more active sites.¹¹ Catalytic performance of 1:1 ratio Ni:Pd alloyed nanoparticle with the average particle size of 5.3 nm deposited on mesoporous silica maintained good activity while recycling, correlated to metallic base metal inhibiting the oxidation of Pd.³⁹ Base metal alloying is also found to be crucial to catalyst stability during consecutive recyclability runs.²⁷

The superior catalytic activity of CuPd/SiO₂ in comparison to NiPd/SiO₂ and CoPd/SiO₂ can be explained by the electronic properties of each system and the expected synergistic effects of the metals involved in the bimetallic catalysts. According to the XPS studies, Cu in the Cu-Pd alloy helps maintain Pd in the unoxidized state (Pd⁰) whereas the deconvoluted Pd spectra of Ni-Pd and Co-Pd alloys reveal binding energies shifted toward Pd²⁺. It is worth noting that density functional theory (DFT) calculations of the bimetallic catalysts suggest the presence of an enhanced synergistic electronic structure upon base metal doping which increases electron density on Pd and hence facilitates the oxidative addition of the aryl halide which is the rate-limiting step in SCC.^{40,41} Our observation is consistent with the catalytic activity trend of MIL-101 supported bimetallic alloys wherein

the catalytic activity was found to be superior for CuPd/MIL-101 followed by NiPd/MIL-101 and CoPd/MIL-101, achieving TOF value of 248 h^{-1} for CuPd/MIL-101.

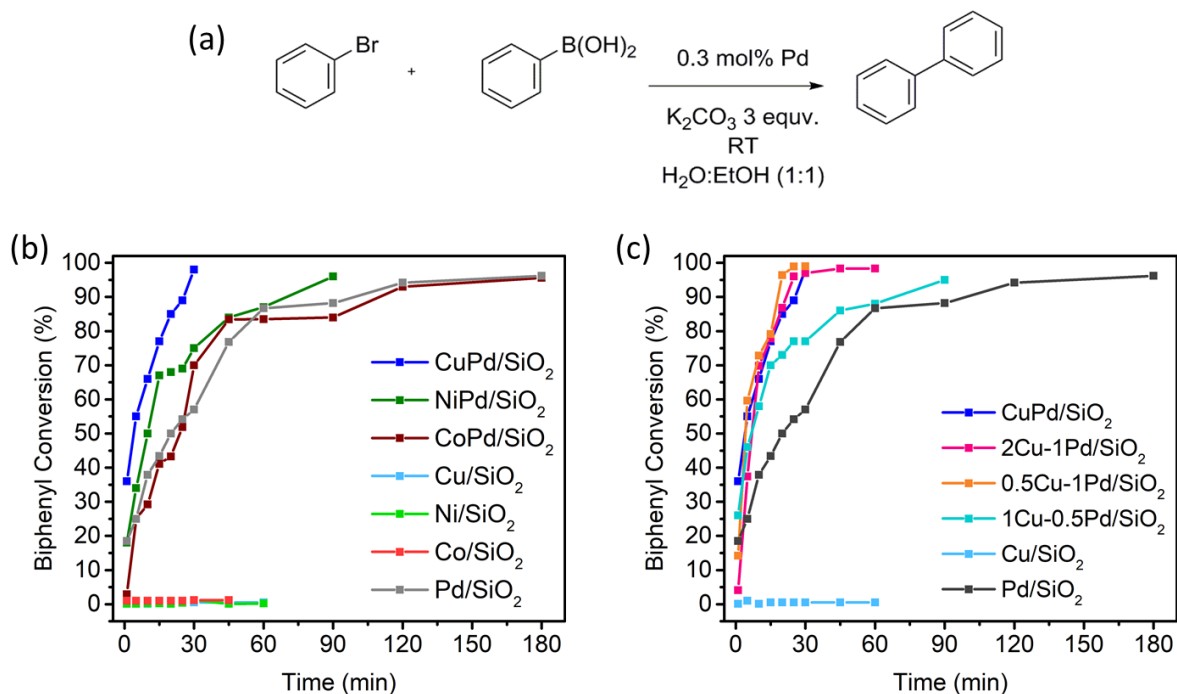


Figure 4.7 (a) Cross-coupling reaction between Bromobenzene with benzenboronic acid (b) Biphenyl conversion of mono and bimetallic NP, (c) biphenyl conversion of various dilution of Pd in Cu NP.

4.4.1 Catalyst Recycling Studies under Microwave Irradiation

Recyclability of the catalyst is a very important criterion for large scale applications. The ability to recycle the best performing catalyst, CuPd/SiO₂ was investigated under MWI at 60 °C for 5 min and compared with the monometallic Pd/SiO₂. The CuPd/SiO₂ catalyst shows excellent recyclability with a biphenyl conversion of 100% achieved for 7 consecutive runs (Table 4.7). The high activity of CuPd/SiO₂ even after

successive runs suggests that the catalyst maintains remarkable activity indicating high stability against sintering and deactivation. The stability of the catalyst was probed by studying the surface morphology and bulk chemical composition of the recycled catalyst by using XRD. The collected XRD patterns for the recycled catalyst after each run are almost identical to the pristine catalyst with a new very broad peak at $\sim 40^\circ$ which is due to small NPs aggregation (Fig. 4.3b). The surface morphology of the catalyst after the 3rd and 6th run was examined via XPS; the result of that, as discussed in the aforementioned XPS section, suggests that the chemical nature of the Cu-Pd alloy is maintained after the runs (Fig. 4.4 and Table 4.6). The bulk metal composition collected by ICP-OES after each run shows that for CuPd/SiO₂ an initial 19% loss in Cu content after the first run, but only an additional 4% loss during the next 6 runs. In contrast, during the first three runs, the content of the Pd only drops by 4% and then has a larger loss of 26% during the recycling runs (Table 4.4). On the other hand, recycled Pd/SiO₂ under similar conditions exhibits a steady drop-in activity upon cycling where the conversion drops to 11% by the 6th run. The ICP also suggests that by the 6th run only 3% of the initial content of Pd has leached ruling out leaching as the primary cause for catalyst deactivation (Table 4.8).

Table 4.7. Recyclability of CuPd/SiO₂ for Suzuki cross-coupling.

Run	Conversion (%)	Run	Conversion (%)
1	100	5	100
2	100	6	100
3	100	7	100
4	100		

Table 4.8 Biphenyl conversions for recyclability of Pd/SiO₂ for Suzuki cross-coupling.

Run	Conversion (%)
1	100
2	97
3	93
4	92
5	91
6	89

For all of the SCC reactions performed under RT and MWI conditions, the Pd content is normalized to 0.3 mol% Pd. To calculate the turn over frequency (TOF) the mol% Pd is lowered (Fig. 4.8 and Table 4.9). TON and TOF are calculated for CuPd/SiO₂, NiPd/SiO₂, CoPd/SiO₂ and Pd/SiO₂. For the SCC reaction catalyzed by CuPd/SiO₂ under MWI condition, the run using 0.03 mol% yielded a 100% biphenyl conversion, the run with 0.01 mol% had a conversion of 97% the run with 0.003 mol% had a conversion of 69% (Fig. 4.8). Lowering Pd content from 0.3 mol%, 0.03 mol%, 0.01 mol% to 0.003 mol% for Pd/SiO₂ catalyst, resulted in biphenyl conversion calculated by GC-FID to be at 100%, 100%, 94% and 84% respectively. Respective conversion%, TOF, and TON values measured for NiPd/SiO₂ and CoPd/SiO₂ are also reported in Fig. 4.8 and Table. 4.9.

The synthesis of different biphenyl products was also investigated under MWI condition to demonstrate the versatility of the optimized CuPd/SiO₂ catalyst. Biphenyl products functionalized with electron-withdrawing terminals such as nitrile (a), nitro (f), and aldehyde (e) except reaction d, containing nitrile group are efficiently synthesized. Reactions containing electron-donating groups, methoxy (b and c) are also catalyzed with a high yield (Fig. 4.9).

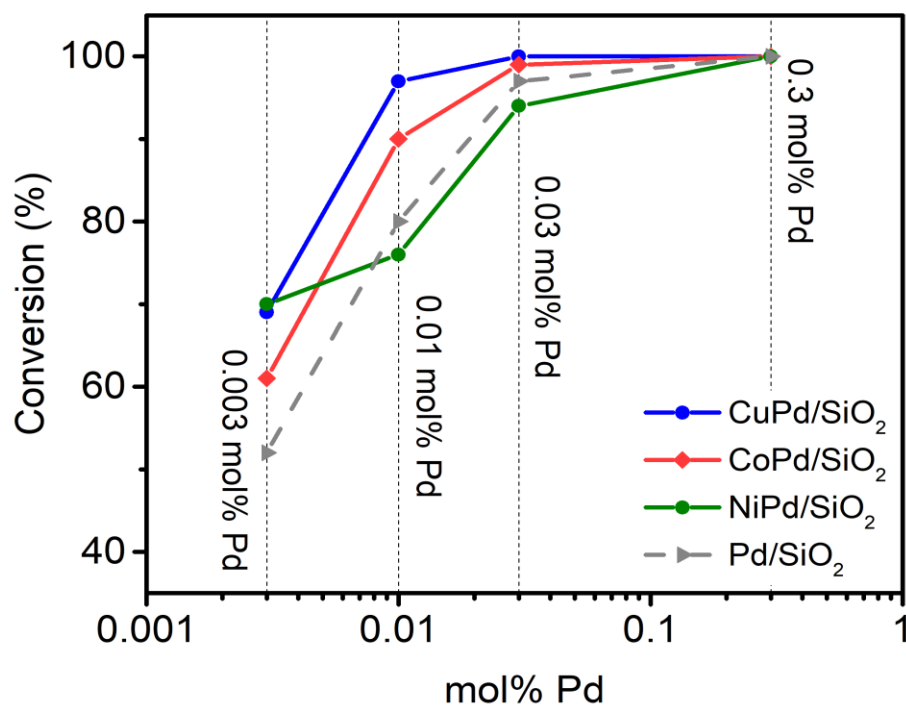


Figure 4.8 Biphenyl Conversion % for bimetallic catalysts and 1 Pd for different mol% Pd.

Table 4.9. TON and TOF calculation for bimetallic catalysts and Pd/SiO₂ for different mol% Pd.

mol% Pd	CuPd/SiO ₂		CoPd/SiO ₂		NiPd/SiO ₂		Pd/SiO ₂	
	TON	TOF (h ⁻¹)	TON	TOF (h ⁻¹)	TON	TOF (h ⁻¹)	TON	TOF (h ⁻¹)
0.3	333	4000	333	4000	333	4000	333	4000
0.03	3333	40000	3266	39196	3233	38800	3233	38800
0.01	9700	116400	9000	108000	7600	91200	8000	96000
0.003	20667	248000	19999	239997	20667	248000	17333	207997

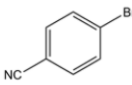
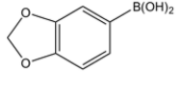
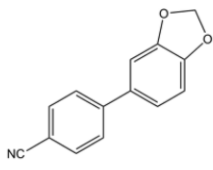
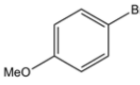
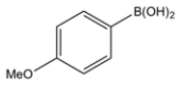
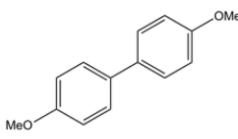
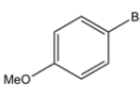
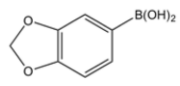
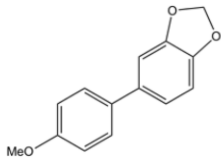
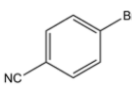
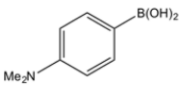
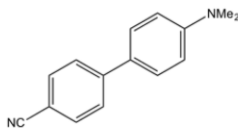
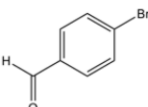
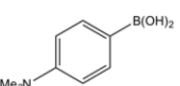
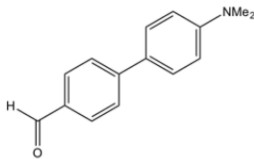
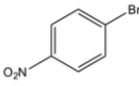
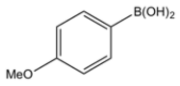
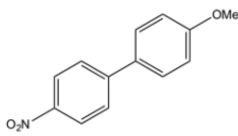
	Aryl bromide	Aryl boronic acid	Products (%) ^b
(a)			
(b)			
(c)			
(d)			
(e)			
(f)			

Figure 4.9 Aryl bromide (0.32 mmol, 1 equiv), arylboronic acid (0.38 mmol, 1.2 equiv), potassium carbonate (133 mg, 0.96 mmol, 3 equiv), and 1Cu1Pd (10.5 mg, 1.05 mmol, 0.3 mol %) in 4 mL (1:1 H₂O–EtOH) was heated at 60 °C (MWI) for 5 min. Conversion (%) was determined by GC–FID analysis.

4.5 Conclusion

A facile, general, reproducible, and highly applicable synthetic technique, strong electrostatic adsorption, has been used for the formation of ultra-small bimetallic alloy nanoparticles. Through this synthetic method, very low bulk content of the precious metal, Pd is alloyed with low content inexpensive base metals (Cu, Ni, and Co). TPR curves for bimetallic samples and their monometallic counterparts confirms the formation of alloyed NPs. The absence of characteristic metal peaks in XRD measurements taken together with HR-TEM images showed the particle size to be on average 1.3 nm. This ultra-small nanoparticle formation increases the efficiency of Pd atoms for catalytic activities. Among the three bimetallic catalysts (CuPd/SiO₂, NiPd/SiO₂, and CoPd/SiO₂) the Cu-Pd catalyst had the superior activity. Under RT and atmospheric pressure conditions, this catalyst reached complete biphenyl conversion in 30 minutes, while NiPd/SiO₂ performed the same reaction in 90 minutes. Monometallic Pd/SiO₂ and CoPd/SiO₂ have only reached full conversion after three hours. The performance of CuPd/SiO₂ for cross-coupling derivatives also yields high conversion values. It was found that CuPd/SiO₂ was highly recyclable while maintaining high catalytic activity. High TON and TOF have also been calculated for all catalysts, especially CuPd/SiO₂. It was shown that bimetallic alloying could alter the electronic structure of the Pd. XPS studies show the Cu-Pd alloy helps maintain Pd at the desired catalytic status of Pd⁰ better than the other bimetallic samples. According to DFT studies, Cu-Pd complexes result in the upward shift of the d-band structure. This synergistic effect validates the superior performance of CuPd/SiO₂ in comparison to the other catalysts. We believe the facile formation of these ultra-small nanoparticles and their

superior catalytic activity can give rise to a new generation of highly efficient Heterogeneous catalysts.

References

- (1) Johansson Seechurn, C. C. C.; Kitching, M. O.; Colacot, T. J.; Snieckus, V. Palladium-Catalyzed Cross-Coupling: A Historical Contextual Perspective to the 2010 Nobel Prize. *Angew. Chem., Int. Ed.* **2012**, *51*, 5062.
- (2) Tasker, S. Z.; Standley, E. A.; Jamison, T. F. Recent Advances in Homogeneous Nickel Catalysis. *Nature* **2014**, *509*, 299–309.
- (3) Cross Coupling Reactions in Organic Synthesis Themed Issue. *Chem. Soc. Rev.* **2011**, *40*, 4877.
- (4) Bi, A.; Centomo, P.; Zotto, A. Del; Zecca, M.; Chimiche, S.; Padova, U.; Padova, I.; Agroalimentari, S.; Sezione, A.; Udine, U.; Scienze, V. Pd Metal Catalysts for Cross-Couplings and Related Reactions in the 21st Century: A Critical Review. **2018**.
- (5) Julia, M.; Duteil, M. Condensation Des Halogénures Aromatiques Avec Les Oléfine Catalysées Par Le Palladium. *Bull. Soc. Chim. Fr* **1973**, 2790, 2790.
- (6) Julia, M.; Duteil, M.; Grard, C. K. E.; Kunz, E. Etude de La Condesation de Chlorures Aromatiques Aves Les Olefines Catalisee Par Le Palladium. *Bull. Soc. Chim. Fr.* **1973**, No. 9–10, 2791–2794.
- (7) Trzeciak, A. M.; Augustyniak, A. W. The Role of Palladium Nanoparticles in Catalytic C–C Cross-Coupling Reactions. *Coord. Chem. Rev.* **2019**, *384*, 1–20.
- (8) Rafiee, F.; Khavari, P.; Payami, Z.; Ansari, N. Palladium Nanoparticles Immobilized on the Magnetic Few Layer Graphene Support as a Highly Efficient Catalyst for Ligand Free Suzuki Cross Coupling and Homo Coupling Reactions. *J. Organomet. Chem.* **2019**, *883*, 78–85.
- (9) Bao, G.; Bai, J.; Li, C.; Yu, D. Carbon Nanofibers Supported Ultra-Small Palladium Oxide Nanoclusters as an Efficient and Continuable Catalyst for Suzuki Coupling Reaction. *Catal. Letters* **2018**, *148* (11), 3389–3401.
- (10) Yang, Y.; Reber, A. C.; Gilliland, S. E.; Castano, C. E.; Gupton, B. F.; Khanna, S. N. Donor/Acceptor Concepts for Developing Efficient Suzuki Cross-Coupling Catalysts Using Graphene-Supported Ni, Cu, Fe, Pd, and Bimetallic Pd/Ni Clusters. *J. Phys. Chem. C* **2018**, *122* (44), 25396–25403.
- (11) Smith, S. E.; Siamaki, A. R.; Gupton, B. F.; Carpenter, E. E. CuPd Nanoparticles as a Catalyst in Carbon–Carbon Cross-Coupling Reactions by a Facile Oleylamine Synthesis. *RSC Adv.* **2016**, *6* (94), 91541–91545.
- (12) Rai, R. K.; Gupta, K.; Behrens, S.; Li, J.; Xu, Q.; Singh, S. K. Highly Active Bimetallic Nickel-Palladium Alloy Nanoparticle Catalyzed Suzuki-Miyaura Reactions. *ChemCatChem* **2015**, *7* (12), 1806–1812.
- (13) Soled, B. S. Silica-Supported Catalysts Get a New Breath of Life. *Science* **2015**, *350* (6265), 1171–1172.
- (14) Wong, A.; Liu, Q.; Griffin, S.; Nicholls, A.; Regalbuto, J. R. Synthesis of Ultrasmall,

- Homogeneously Alloyed, Bimetallic Nanoparticles on Silica Supports. *Science* **2017**, 358 (6369), 1427–1430.
- (15) Spieker, W. A.; Regalbuto, J. R. A Fundamental Model of Platinum Impregnation onto Alumina. *Chem. Eng. Sci.* **2001**, 56 (11), 3491–3504.
- (16) Jiao, L.; Regalbuto, J. R. The Synthesis of Highly Dispersed Noble and Base Metals on Silica via Strong Electrostatic Adsorption: I. Amorphous Silica. *J. Catal.* **2008**, 260 (2), 329–341.
- (17) Brunelle, J. P. Preparation of Catalysts by Metallic Complex Adsorption on Mineral Oxides. *Pure Appl. Chem.* **1978**, 50 (9–10), 1211–1229.
- (18) Kyriakidou, E. A.; Alexeev, O. S.; Wong, A. P.; Papadimitriou, C.; Amiridis, M. D.; Regalbuto, J. R. Synthesis of Ag Nanoparticles on Oxide and Carbon Supports from Ag Diammine Precursor. *J. Catal.* **2016**, 344, 749–756.
- (19) Cho, H. R.; Regalbuto, J. R. The Rational Synthesis of Pt-Pd Bimetallic Catalysts by Electrostatic Adsorption. *Catal. Today* **2015**, 246, 143–153.
- (20) Van Den Berg, R.; Elkjaer, C. F.; Gommers, C. J.; Chorkendorff, I.; Sehested, J.; De Jongh, P. E.; De Jong, K. P.; Helveg, S. Revealing the Formation of Copper Nanoparticles from a Homogeneous Solid Precursor by Electron Microscopy. *J. Am. Chem. Soc.* **2016**, 138 (10), 3433–3442.
- (21) Santhanam, N.; Conforti, T. A.; Spieker, W.; Regalbuto, J. R. Nature of Metal Catalyst Precursors Adsorbed onto Oxide Supports. *Catalysis today*. Amsterdam 1994, pp 141–156.
- (22) Rai, R. K.; Gupta, K.; Tyagi, D.; Mahata, A.; Behrens, S.; Yang, X.; Xu, Q.; Pathak, B.; Singh, S. K. Access to Highly Active Ni-Pd Bimetallic Nanoparticle Catalysts for C-C Coupling Reactions. *Catal. Sci. Technol.* **2016**, 6 (14), 5567–5579.
- (23) Carmen, M. L.; Oropeza, F.; Alvarez, J.; Goldwasser, M.; Francisco, L.; Josefina, M. P. HMS Mesoporous Silica as Cobalt Support for the Fischer–Tropsch Synthesis: Pretreatment, Cobalt Loading and Particle Size Effects. *J. Mol. Catal. A Chem.* **2008**, 281 (1–2), 146–153.
- (24) O’Connell, K.; Regalbuto, J. R. High Sensitivity Silicon Slit Detectors for 1 Nm Powder XRD Size Detection Limit. *Catal. Letters* **2015**, 145 (3), 777–783.
- (25) Wang, M.; Guo, D. J.; Li, H. L. High Activity of Novel Pd/TiO₂ Nanotube Catalysts for Methanol Electro-Oxidation. *J. Solid State Chem.* **2005**, 178 (6), 1996–2000.
- (26) Li, X.; Wang, Z.; Zhang, Z.; Yang, G.; Jin, M.; Chen, Q.; Yin, Y. Construction of Au–Pd Alloy Shells for Enhanced Catalytic Performance toward Alkyne Semihydrogenation Reactions. *Mater. Horizons* **2017**, 4 (4), 584–590.
- (27) Jamwal, B.; Kaur, M.; Sharma, H.; Khajuria, C.; Paul, S.; Clark, J. H. Diamines as Interparticle Linkers for Silica-Titania Supported PdCu Bimetallic Nanoparticles in Chan-Lam and Suzuki Cross-Coupling Reactions. *New J. Chem.* **2019**, 43 (12), 4919–4928.
- (28) Hegde, M. S.; Caracciolo, R.; Hatton, K. S.; Wachtman, J. B. Electronic Structure and Bonding in Silicon Oxynitride Films: An XPS Study. *Appl. Surf. Sci.* **1989**, 37 (1), 16–24.
- (29) Mondal, P.; Sinha, A.; Salam, N.; Roy, A. S.; Jana, N. R.; Islam, S. M. Enhanced Catalytic Performance by Copper Nanoparticle-Graphene Based Composite. *RSC*

- Adv.* **2013**, *3* (16), 5615–5623.
- (30) Gonzalez-Arellano, C.; Balu, A. M.; Luque, R.; MacQuarrie, D. J. Catalytically Active Self-Assembled Silica-Based Nanostructures Containing Supported Nanoparticles. *Green Chem.* **2010**, *12* (11), 1995–2002.
- (31) Natesakhawat, S.; Lekse, J. W.; Baltrus, J. P.; Ohodnicki, P. R.; Howard, B. H.; Deng, X.; Matranga, C. Active Sites and Structure-Activity Relationships of Copper-Based Catalysts for Carbon Dioxide Hydrogenation to Methanol. *ACS Catal.* **2012**, *2* (8), 1667–1676.
- (32) Liu, M.; Liu, J.; Li, Z.; Wang, F. Atomic-Level Co₃O₄ Layer Stabilized by Metallic Cobalt Nanoparticles: A Highly Active and Stable Electrocatalyst for Oxygen Reduction. *ACS Appl. Mater. Interfaces* **2018**, *10* (8), 7052–7060.
- (33) Rana, S.; Ram, S. X-Ray Diffraction and X-Ray Photoelectron Spectroscopy Studies of Stabilised Cobalt Nanoparticles with a Thin Al₂O₃ Surface Layer. *Mater. Sci. Technol.* **2005**, *21* (2), 243–249.
- (34) Mahata, N.; Cunha, A. F.; Órfão, J. J. M.; Figueiredo, J. L. Hydrogenation of Nitrobenzene over Nickel Nanoparticles Stabilized by Filamentous Carbon. *Appl. Catal. A Gen.* **2008**, *351* (2), 204–209.
- (35) Yin, Z.; Zhou, W.; Gao, Y.; Ma, D.; Kiely, C. J.; Bao, X. Supported Pd-Cu Bimetallic Nanoparticles That Have High Activity for the Electrochemical Oxidation of Methanol. *Chem. - A Eur. J.* **2012**, *18* (16), 4887–4893.
- (36) Yuan, B.; Pan, Y.; Li, Y.; Yin, B.; Jiang, H. A Highly Active Heterogeneous Palladium Catalyst for the Suzuki-Miyaura and Ullmann Coupling Reactions of Aryl Chlorides in Aqueous Media. *Angew. Chemie - Int. Ed.* **2010**, *49* (24), 4054–4058.
- (37) Sawai, K.; Tatumi, R.; Nakahodo, T.; Fujihara, H. Asymmetric Suzuki-Miyaura Coupling Reactions Catalyzed by Chiral Palladium Nanoparticles at Room Temperature. *Angew. Chemie - Int. Ed.* **2008**, *47* (36), 6917–6919.
- (38) Yang, H.; Han, X.; Li, G.; Wang, Y. N-Heterocyclic Carbene Palladium Complex Supported on Ionic Liquid-Modified SBA-16: An Efficient and Highly Recyclable Catalyst for the Suzuki and Heck Reactions. *Green Chem.* **2009**, *11* (8), 1184–1193.
- (39) Saha, J.; Bhowmik, K.; Das, I.; De, G. Pd–Ni Alloy Nanoparticle Doped Mesoporous SiO₂ Film: The Sacrificial Role of Ni to Resist Pd-Oxidation in the C–C Coupling Reactio. *Dalt. Trans.* **2014**, *43* (35), 13325–13332.
- (40) Sperger, T.; Le, C. M.; Lautens, M.; Schoenebeck, F. Mechanistic Insights on the Pd-Catalyzed Addition of C–X Bonds across Alkynes – a Combined Experimental and Computational Study. *Chem. Sci.* **2017**, *8* (4), 2914–2922.
- (41) Alvaro, E.; Hartwig, J. F. Resting State and Elementary Steps of the Coupling of Aryl Halides with Thiols Catalyzed by Alkylbisphosphine Complexes of Palladium. *J. Am. Chem. Soc.* **2009**, *131* (22), 7858–7868.

Chapter 5

Nickel Nanoparticles Supported on Nitrogen-doped Porous Carbon as Cathode Materials for Lithium-Sulfur Batteries

5.1 Introduction

As energy demands continue to grow, fossil fuels have been the dominant source of energy and their consequential harmful environmental effects of consuming fossil fuel have also been growing. Transitioning from fossil fuels to renewable energy sources has gained a lot of attention. Lithium ion batteries (LIBs) have revolutionized the portable energy demanding devices, whether they are mobile phones or cars. Vast research and investment on LIBs have facilitated the commercialization of these batteries, but their shortcomings such as low energy-to-weight ratios (140–260 Whkg⁻¹) and high production costs (>\$300 per kWh for battery packs)¹ have hampered their application in devices with larger energy demands such as electronic vehicles (EVs) and energy storage systems (ESSs). One of the most promising candidates to answer the shortcomings of LIBs are lithium-sulfur batteries (LSBs), they are composed of a lithium metal anode and a sulfur cathode with a high theoretical capacity (sulfur: 1672 mAh g⁻¹, lithium metal: 3860 mAh g⁻¹).² The production cost for LSBs is projected to be at <125 per kWh, which is a much more suitable price-to-energy ratio for EVs industry.¹

To compete with LIBs, there are few practical requirements that LSBs should have such as sufficient sulfur content, high areal sulfur loading, and low electrolyte to sulfur ratios. While overcoming these requirements exposes the challenges involved with LSBs, such as the poor electrical conductivities of sulfur ($5 \times 10^{-30} \text{ S cm}^{-1}$) and Li_2S and the large volume change between S_8 and Li_2S . Furthermore, the loss of active materials in between battery components leads to the overall loss of activity, and the soluble lithium polysulfide can dissolve in the organic electrolyte, which can then shuttle in between battery electrodes lowering the coulombic efficiency. The efforts to address these problems can be summarized in the development of a conductive framework that is also sulfur adsorbent.³

In this chapter, Ni NPs (~ 4.3 nm) are deposited on the high surface area N-doped carbon support (BIDC-900, $3560 \text{ m}^2 \text{ g}^{-1}$) through SEA to address the aforementioned shortcoming of LSBs. The deposited Ni NPs (0.9 wt%) on the surface act as active centers inducing catalytic activity by enhancing the adsorption of lithium polysulfides and facilitating the redox reactions of LPS which mitigates their dissolution from the cathode.

5.2 Experimental Section

5.2.1 Synthesis of Nitrogen-doped Carbon Support

Benzimidazole (TCI America, >98%) an inexpensive and commercially available precursor and potassium hydroxide (Alfa Aesar, ACS, 85% min, K_2CO_3 2.0% max pellets) were chosen as a precursor and activation agent for the carbonization/chemical activation reaction. For an easier mass transport in the solid-solid reaction, as purchased KOH pellets were crushed inside a glovebox using a mortar and pestle, and the fine KOH powder was degassed overnight in Quantachrome's MasterPrep Degasser before being mixed with BI

inside the glovebox before the carbonization. KOH and benzimidazole were mixed in a 2:1 weight ratio as it had been investigated that the 2:1 weight ratio yields highly porous nitrogen-doped carbon.⁴ The white powder mixture was transferred to Carbolite temperature-programmed tube furnace under a steady flow of argon. The temperature was increased to 900 °C at a ramp rate of 5 °C min⁻¹ and a holding time of 1 hour, then cooled to room temperature. The benzimidazole derived carbon was given the name of B IDC-900, where 900 indicates the activation temperature. The carbonized product requires post purification, by first, soaking in 1.0 M HCl to remove residual salt and metallic potassium; second, washing with 2 liters of distilled water and finally washed with ethanol to replace the water in the pores for easier drying.

According to thermogravimetric analysis (TGA) results for benzimidazole, weight loss transformation starts at 150 °C and reaches a complete mass loss at around 300 °C. KOH low melting point (170 °C) makes it a suitable activation agent for the generation of an optimized porous structure. Benzimidazole initially reacts with KOH to form potassium-benzimidazole salt, which according to TGA data is non-volatile and in the presence of excess KOH, thermal activation continues through various methods such as, etching (by redox reactions), gasification (by evolving gaseous species such as H₂O and CO₂) and expansion (by metallic potassium) of the carbon framework porosity development at 900 °C will lead to highly porous nitrogen-doped carbon, B IDC-900 was degassed under vacuum at 200 °C for 12 h on Quantachrome Autosorb-iQ before gas sorption measurements.

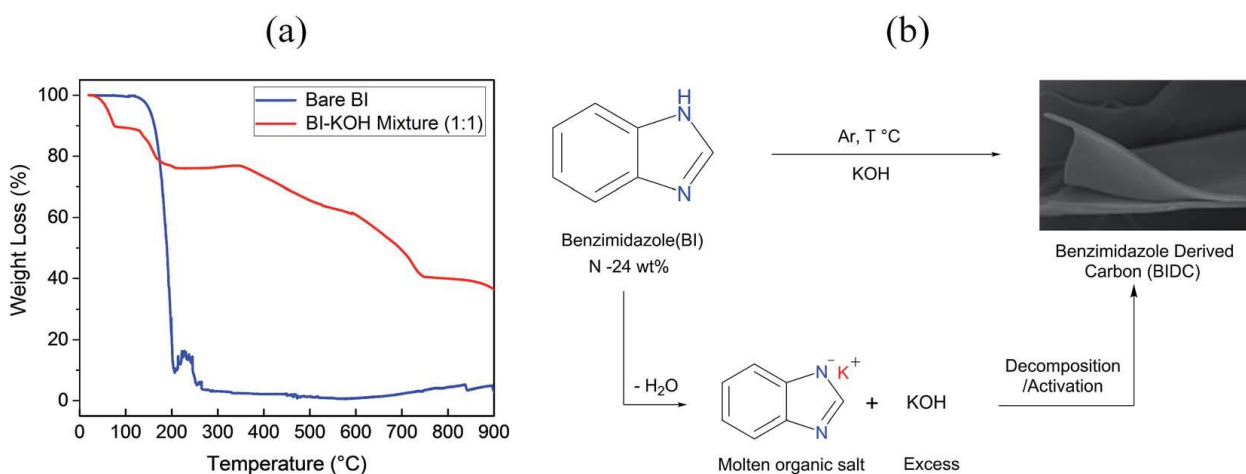


Figure. 5.1 (a) Thermogravimetric analysis of a pure organic building block versus a mixture of BI with KOH. (b) The reaction of the organic building block with KOH and conversion to porous carbon using excess KOH. (Copyright 2016 American Chemical Society)

5.2.2 Strong Electrostatic Adsorption

5.3.2.1 Point of Zero Charge

The pH of the point of zero charge (PZC) for the nitrogen-doped carbon was measured using the pH drift method.⁵⁻⁷ In this technique, 10 mg of BIDC-900 is dispersed into 30 mL of MQ water, and the pH of the solutions was adjusted between 2 and 12, using HCl and NaOH solutions at two different concentrations of 0.01 M and 1 M. The initial pH values were recorded. All solutions are stirred for 24 hours at room temperature, for the pH to stabilize, after that the final pH is recorded. The graph of final pH vs initial pH is drawn and the PZC is the point in which initial pH and final pH values are equal, according to the Figure 5.2, BIDC-900 has the PZC of ~ 6.5.

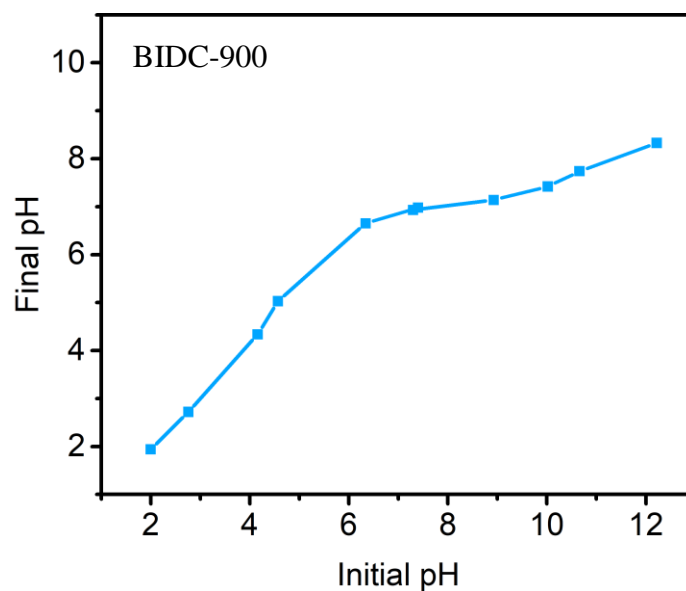


Figure 5.2 Final pH vs. initial pH, PZC measured using pH drift method.

5.2.2.3 Deposition of Nickel on B IDC-900 by Strong Electrostatic Adsorption

The SEA synthesis technique was performed according to methods reported in the literature.^{8,9} In brief, a measured amount of the support is dispersed in MQ water and the pH of the solution is adjusted to 12 using 5N NH₃. The cationic precursor salt used for SEA was Nickel (II) nitrate hexahydrate (Alfa Aesar, 98%), 2000 ppm Ni stock solution was prepared by dissolving the required amount of metal salt in 5N NH₃ solution. A known support mass was taken and the total volume of the solution was calculated to yield a surface loading of 1000 m² L⁻¹ (Eq. 5.1). Surface loading (SL) in m² L⁻¹, surface area (SA) in m² g⁻¹, the mass of the support in g and total volume of the solution in L. While the support solution is continuously stirred, the 2 wt% loading of the metal stock solution is

pipetted into the support solution, allowing the cationic metal precursor to adsorb, and the solution is further stirred for 30 minutes. Following the deposition, the support is filtered using a filter funnel with a fritted disc and washed with water and ethanol. The sample is air-dried overnight, oven-dried at 120 °C for 4 h, and then reduced under a flow of H₂ (5% in N₂) at 600 °C for one hour using a tube furnace. After reduction, Ni nanoparticles are formed on the surface of Ni/BIDC-900.

$$SL = \frac{SA * \text{mass of the support}}{\text{Volume}} \quad (5.1)$$

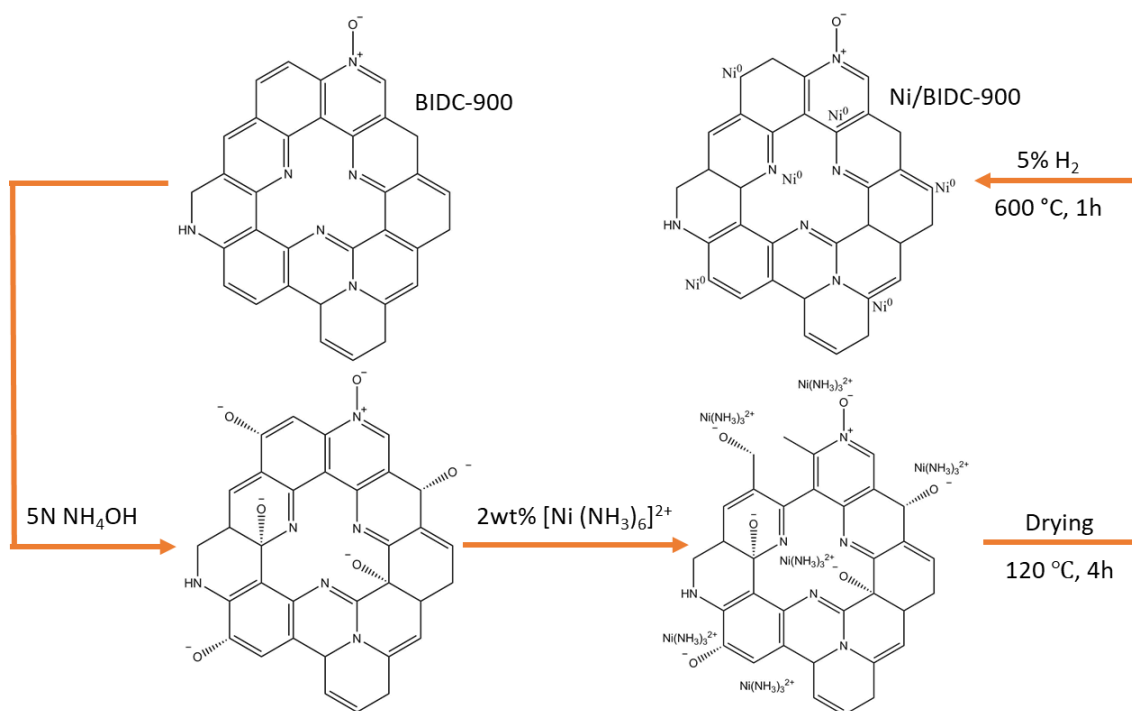


Figure 5.3 Synthesis of Ni/BIDC-900 using the SEA method.

5.2.3 Electrochemical Measurements

The electrochemical activity of the batteries was investigated using 2032-type cells vs. Li. A slurry of the active material, Super-P additives (Alfa Aesar, 99+%), and polyvinylidene fluoride (PVDF, Alfa Aesar, 99%) at a weight ratio of 8:1:1 in was mixed in N-methyl-2-pyrrolidinone (NMP, ACS grade, Alfa Aesar, 99%) to form a homogeneous solution, which was then pasted onto battery-grade aluminum foil current collector by doctor blading. The paste was dried in a vacuum at 60 °C overnight to remove all solvents and moisture. The resulting foil was rolled pressed and cut into discs with a diameter of 13 mm. The sulfur loading (mgs cm^{-2}) is reported for each battery. Lithium foil was used as the anode, and Celgard 2400 was used as the separator. The electrolyte was 1M lithium bis trifluoromethane sulfonyl imide (LiTFSI, Alfa Aesar, 98%) in 1,3-dioxolane (DOL, Acroseal, Acros Organic, 99.8%) and 1,2-dimethoxyethane (DME, Acroseal, Acros Organic, 99%), (v/v = 1:1) containing 0.5 M lithium nitrate (LiNO_3 , Alfa Aesar, 99%). All the batteries assembly was carried out in an argon-filled glovebox (Mbraun UNIlab 2000 Plus Glove Box). The assembly of any Li-S coin cell was done inside the glovebox with \leq 1 ppm concentration for both H_2O and O_2 . The charge/discharge tests were carried out in a voltage range of 1.7–3.0 V. All capacity values were calculated based on the mass of sulfur loading. Cyclic voltammetry (CV) was conducted with a CHI 660D electrochemical measurement system. The CV tests were performed at a scan rate of 0.1 mV s^{-1} in the voltage range of 1.7–3.0 V. All the electrochemical tests were conducted at room temperature. The other battery testing technique used to characterize batteries is

galvanostatic charge/discharge, where over a defined voltage range, a constant current is carried for charge and discharge, while the potential across the cell is measured.

This testing allows the determination of electrode capacity, cell energy, and coulombic efficiency. Typically, standardized charging currents (C rates) are used for this testing based on the active material theoretical capacity, which is calculated according to equation 5.2 where n is the number of electrons transferred in the cell reaction, F is faraday's constant, and M is the active material molar mass.

$$Capacity = \frac{nF}{M} \quad (5.2)$$

The theoretical capacity, typically expressed in units of mAh g⁻¹, is used for calculation of cationic and anionic currents to deliver specific cycle lengths. If the charge durations are 10 hr, 1 hr, and 0.5 hr, corresponding C rates are 0.1C, 1C, and 0.5C, respectively. At these currents the actual capacity of the cells is calculated using equation 5.3 where I , is the applied current, t is the time of discharge, and m is the mass of active material.

$$Capacity = \frac{it}{m} \quad (5.3)$$

Coulombic efficiency is another identification parameter in which the capacity of the discharge is divided by the capacity of the charge (Eq. 5.4), the reversibility of the cell reaction is assessed with this metric.

$$Columbic\ efficiency = \frac{C_{discharge}}{C_{charge}} \quad (5.4)$$

5.2.4 Instrumentation

Textural properties of doped porous carbon samples were investigated using nitrogen adsorption/desorption isotherms collected by Quantachrome Autosorb-iQ at 77 K based on the Brunauer–Emmett–Teller (BET) equation. Pore size distribution (PSD) analysis based on the N₂ isotherm was investigated via quenched solid density functional theory (QSDFT) model. The ratio of the micropore volume to the total pore volume ($V_{\text{mic}}/V_{\text{total}}$) was calculated from the cumulative pore volume branch of PSD curves. Powder X-ray diffraction was examined with X-ray diffraction (P-XRD) patterns collected at room temperature using a Panalytical X'Pert Pro Multipurpose Diffractometer (MPD). The samples were mounted on a zero-background sample holder measured in transmission mode using Cu K α radiation (operated at 40 kV, 45 mA; $\lambda=0.15418$ nm), the diffraction angle ranging from 10° to 70° with a step size of 0.02° and a rate of 1.2° min⁻¹. X-ray photoelectron spectroscopy (XPS) analysis was performed on a Thermo Fisher Scientific ESCALAB 250 spectrometer employing an Al K α (1486.68 eV) X-ray source equipped with a hemispherical analyzer and XR5 Gun 500 μm (15 kV). Samples for XPS measurements were prepared by pressing the carbon specimen into a piece of indium foil, which was then mounted onto the sample holder using double-sided tape. During XPS analysis, the combination of a low-energy electron flood gun and an argon ion flood gun was utilized for charge compensation. The binding energy scale was calibrated by setting the C 1s peak at 284.8 eV. The XPS results were analyzed with the CasaXPS software (v4.84). Inductively coupled plasma – optical emission spectrometry (ICP-OES) was also conducted, measuring the bulk composition of the metal in the carbonaceous structure.

High Resolution Transition Electron Microscopy (HR-TEM) was performed using a FEI Titan 300 kV equipped with a Gatan 794 Multi-Scan Camera, a HAADF-STEM detector. Samples were drop-casted on carbon-coated grids (Ted Pella, Inc.) and left to dry overnight at room temperature. Captured images were processed using ImageJ software.

5.3 Result and Discussion

5.3.1 Characterization

The textural properties of the doped-carbon support, B IDC-900, were measured by nitrogen isotherms using the nitrogen adsorption isotherms collected by Quantachrome Autosorb-iQ at 77K based on Brunauer-Emmett-Teller (BET) equation. The surface area of B IDC-900 is $3560 \text{ m}^2 \text{ g}^{-1}$ with a total pore volume of $2.0 \text{ cm}^3 \text{ g}^{-1}$, respectively (Figure 5.4 and Table 5.1). According to IUPAC classification, B IDC-900 shows a hybrid type I/IV isotherm with a sharp initial rise in the N_2 uptake at very low relative pressures, a distinct feature of type I isotherms consisting of micropores, followed by a gradual increase in the uptake for the remaining of the pressure range, indicating the presence of mesopores. (Figure 5.4a). Benzimidazole has a pre-formed aromatic structure with high initial nitrogen content (25 wt%) facilitating the formation of nitrogen-doped, highly porous graphitic structure. In comparison with the theoretical surface area of graphene ($\sim 2600 \text{ m}^2 \text{ g}^{-1}$), the obtained specific surface area value of $3560 \text{ m}^2 \text{ g}^{-1}$ (Table 5.1) suggests that it can be regarded as 3D textured framework made up from nanosheets and that most nitrogen/carbon atoms are accessible from the sides.⁴ B IDC-900 has 60% micropores and 40% mesopores, calculated from the cumulative pore volume branch of pore size distribution curves via quenched solid density functional theory (QSDFT) for slit-shaped pores.

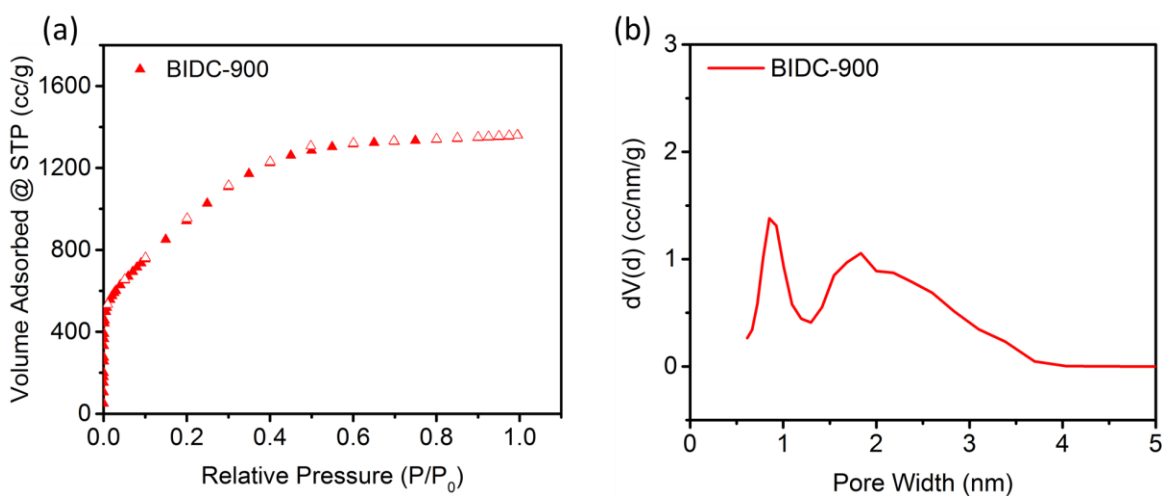


Figure 5.4 (a) N₂ sorption isotherm of B IDC-900 at 77 K (solid symbols denote adsorption points, and hollow symbols denote desorption points). (b) Pore size distribution from QSDFT model using N₂ isotherms at 77 K.

Table 5.1 Textural Properties of B IDC-900 Determined by Nitrogen Porosity Measurements.

Sample	S _{BET} ^a (m ² g ⁻¹)	V _{TOT} ^b (cm ³ g ⁻¹)	V _{Mic} ^c (cm ³ g ⁻¹)	V _{meso} ^c (cm ³ g ⁻¹)	C (wt %)	O (wt %)	N (wt %)
B IDC-900	3560	1.972	1.19(60)	0.77	84	10.5	3.1

^a Brunauer–Emmett–Teller (BET) surface area. ^b Total pore volume at P/P₀ = 0.99. ^c Determined by PSD assuming slit-shaped pores and the QSDFT model from N₂ adsorption data at 77 K (the values in parentheses is the percentages of mesopore volume relative to total pore volume). Weight percentages determined by elemental analysis.

P-XRD patterns for the pristine B IDC-900 and the Ni/B IDC-900 were collected. Highly disordered materials such as amorphous carbon-containing big carbon flakes yield high background intensity diffractions, especially at low angles.^{10,11} This phenomenon results in the graphitic peak at 23° that corresponds to the (002) plane to be concealed. The hump at 43° corresponds to the (100) plane of the graphitic structure of the sample (Fig 5.5). The absence of metal characteristic peaks suggests metal nanoparticles are ultra-small and cannot be detected.¹²

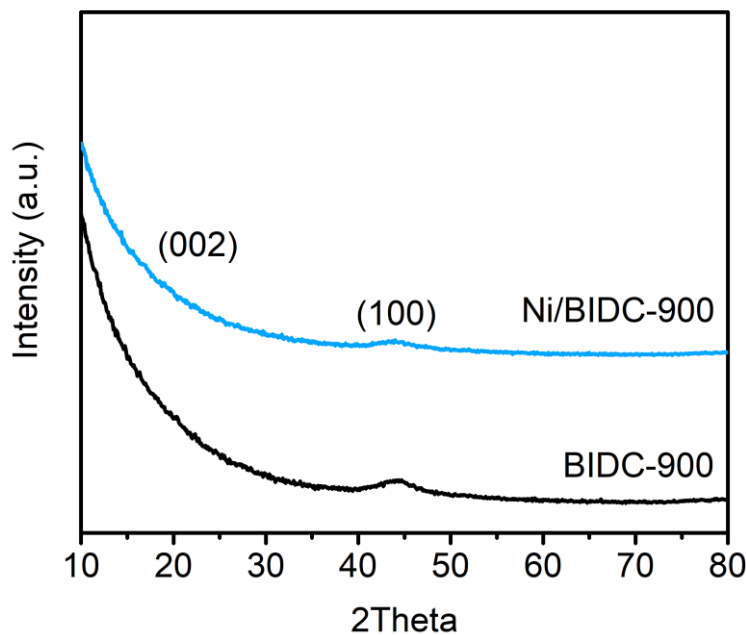


Figure 5.5 P-XRD patterns for B IDC-900 and Ni/B IDC-900.

To determine the bulk content of Ni in Ni/B IDC-900, ICP-OES was performed. A sample (5 mg) was digested in aqua regia overnight at 60 °C while stirring, and 5% nitric

acid matrix was prepared using the entire digested samples. From the initial 2 wt% Ni introduced to the synthesis solution, 45% has been adsorbed leading to 0.9 wt% Ni adsorbed on the surface. Immediately after the deposition, the sample was filtered before washing, an aliquot of the filtrate was diluted to 5% nitric acid. The ICP result from the filtrate showed 88% of the introduced Ni is adsorbed on the surface, yielding the metal loading of 1.76 wt%. Almost half of the deposited Ni that is weakly adsorbed are lost while washing and drying.

XPS survey spectra for B IDC-900 and Ni/B IDC-900 provide the surface chemical composition and confirm the presence of carbon, oxygen, nitrogen, and nickel (Figure 5.6 a). The C 1s spectra of both samples show the dominant presence of sp^3 -hybridized carbon, suggested by a peak at 284.8 eV and an asymmetric tail at 288.9 eV towards higher binding energies.¹³ Another peak in the C 1s spectrum correlates to the sp^2 -hybridized carbon-carbon double bond at 285.9 eV (Figure 5.6 b).¹⁴ The spectrum for N 1s is low in intensity, and based on N spectrum reported for benzimidazole derived porous carbons,⁴ the deconvoluted spectrum does not represent the full characteristic of the N-dopant. For both samples only a single peak positioned at 400.4 - 400.6 eV can be detected, this peak can be assigned to the pyrrolic nitrogen (Fig. 5.6 c).¹³ Detailed deconvolution of O 1s suggests C-O, an oxidized derivative of an aromatic compound with a peak at 532.9 - 533.0 eV for both samples.¹⁵ For the B IDC-900 another peak at 534.5 eV is also present, this broad peak can be assigned to COOH, the carboxylic group (Figure 5.6 d).¹⁶ Disappearance of this peak in Ni/B IDC-900 sample suggests that the carboxylic functionality is the adsorption site for Ni cation during SEA synthesis. With the increase

of pH during SEA above BDC-900's point of zero charge at 6.5 to 12, the carboxylic groups deprotonate and provide the adsorption sites for the metal cation. While it is expected that the metal cation might be adsorbed to the lone electron pair of the nitrogen atoms in the carbon framework, the low intensity of the nitrogen peak does not provide enough detail to reach such a conclusion. The deconvoluted Ni 2p_{3/2} can be deconvoluted to three peaks at 853.9, 855.8 and 856.9 eV corresponding to Ni⁰, Ni²⁺, and Ni⁺³.¹⁷ The satellite peak which is expected to have ~6 eV shift, has a peak at 859.9 eV.¹⁷

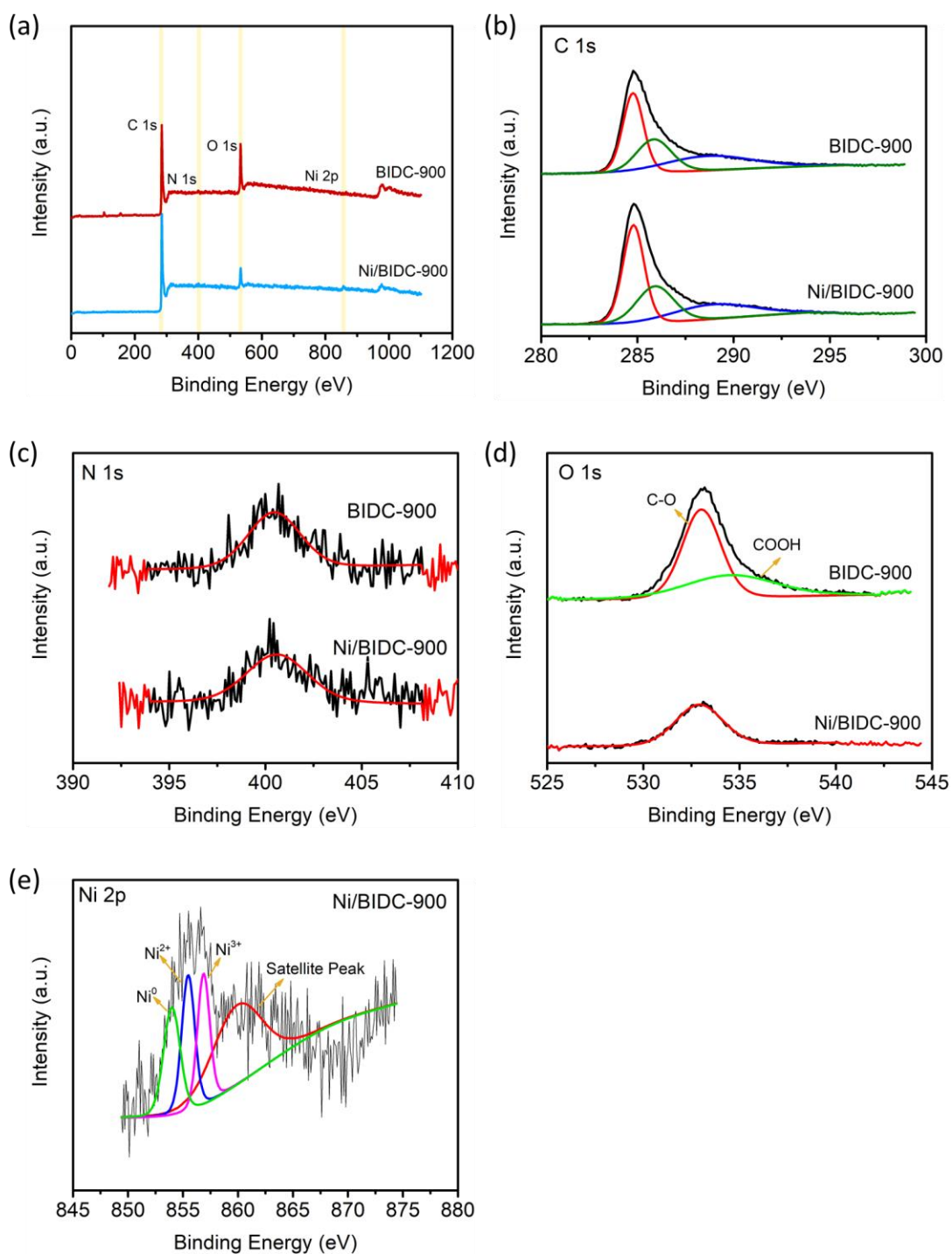


Figure 5.6 (a) Survey spectra of Ni/BIDC-900. (b) Deconvoluted C 1s spectra. (c) Deconvoluted N 1s spectra. (d) Deconvoluted O 1s spectra. (e) Deconvoluted Ni 2p spectra.

Table 5.2 Surface chemical composition of BIDC-900 and Ni/BIDC-900 collected from XPS Survey Spectrum.

Sample	C (At%)	O (At%)	N (At%) XS	Ni (At%)
BIDC-900	84.3	15.1	0.6	N/A
Ni/BIDC-900	94.1	5.6	0.3	0.04

HRTEM and STEM images were collected and analyzed to determine the metal nanoparticle size and distribution. The uniform distribution of the particle is apparent from the HRTEM images. It can also be concluded that the particle size distribution is narrow, ranging from 3.0-6.0 nm and centered about 4.3 nm.

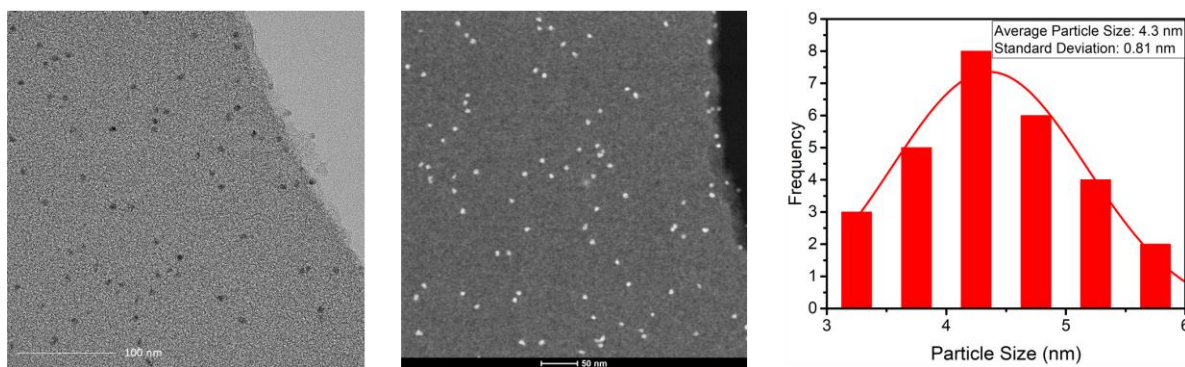


Figure 5.7 HRTEM, STEM, and the corresponding particle size distribution for Ni/BIDC-900.

5.3.2 Electrochemical Measurements

Cyclic voltammetry (CV) was performed at a scan rate of 0.1 mV s^{-1} . The conversion rate of polysulfide, which entails a series of liquid-solid reactions determines the overall performance of the battery. The reduction wave of the CV curve for LSB has two peaks corresponding to the reduction of S_8 to the soluble lithium polysulfides (LiS_x , $8 < x < 4$), and insoluble Li_2S_2 or Li_2S , respectively. For S/Ni/BIDC-900 the peaks are poisoned at 2.32 and 2.0 mV and in the case of S/BIDC-900 the reduction peaks are at 2.25 and 1.98 mV (Fig. 5.8). For the onset reduction potentials of S/Ni/BIDC-900 the peaks have positive shifts of 7 mV and 2 mV, respectively in comparison to S/BIDC-900. This positive shift in the position of the peaks, suggests a faster reduction reaction that requires less overpotential.¹⁸ The shift in overpotential could also be induced by the removal of a reaction barrier. The onset oxidation potential remains almost the same for both samples. The peaks for S/Ni/BIDC-900 are positioned at 2.45 and 2.55 mV. Whereas the peaks for S/BIDC-900 are merged and not easily distinguishable. They are positioned at 2.36 and 2.44 mV. It can be expected that the diffusion layer is becoming thinner in S/Ni/BIDC-900.¹⁹ A comprehensive conclusion requires performing CV at different scan rates. It is expected that the i_p (A) increases linearly with the square root of the scan rate v (V s^{-1}), in which the slope corresponds to the Lithium-ion diffusion coefficients (D_{Li^+}) that can be calculated using the Randles–Sevcik equation (Eq. 5.6). Bigger cathodic peaks and larger intensities show the enhanced LPSs conversion in S/Ni/BIDC-900 than S/BIDC-900.²⁰

$$i_p = 0.446nFAC^0 \left(\frac{nFvD_0}{RT} \right)^{1/2} \quad (5.6)$$

i_p (A) is peak current, scan rate ν ($V s^{-1}$), n is the number of electrons transferred in the redox event, A (cm^2) is the electrode surface area (usually treated as the geometric surface area), D_0 ($cm^2 s^{-1}$) is the diffusion coefficient of the oxidized analyte, and C^0 ($mol cm^{-3}$) is the bulk concentration of the analyte.

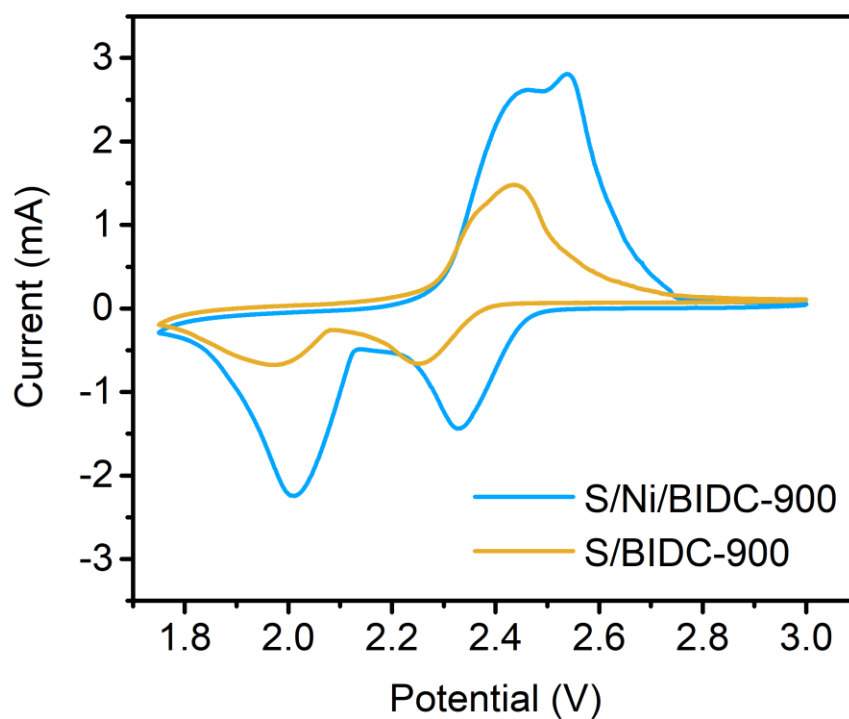


Figure 5.8 cyclic voltammetry profile of S/Ni-BIDC-900 and S/BIDC-900 collected at a scan rate of $0.1 mV S^{-1}$ in the potential range 1.75–3 V

Table 5.3 The peak voltages of asymmetrical Li-S cells using different host composites of B IDC/S and Co-B IDC/S in the CV profiles (Figure 5.8).

Host Materials	Peak voltage (V)			
	$S_8 \rightarrow Li_2S_x (8 < x < 4)$	$Li_2S_x (8 < x < 4) \rightarrow Li_2S$	$Li_2S \rightarrow Li_2S_x (8 < x < 4)$	$Li_2S_x (8 < x < 4) \rightarrow S_8$
S/B IDC-900	2.25	1.98	2.36	2.44
S/Ni/B IDC-900	2.32	2.00	2.45	2.55

Table 5.4 The peak current density of asymmetrical Li-S cells using different host composites of B IDC/S and Co-B IDC/S in the CV profiles (Figure 5.8).

Host Materials	Peak current density (mA. g ⁻¹)			
	$S_8 \rightarrow Li_2S_x (8 < x < 4)$	$Li_2S_x (8 < x < 4) \rightarrow Li_2S$	$Li_2S \rightarrow Li_2S_x (8 < x < 4)$	$Li_2S_x (8 < x < 4) \rightarrow S_8$
S/B IDC-900	-0.67	-0.70	1.19	1.49
S/Ni/B IDC-900	-1.46	-2.25	2.60	2.80

The S/Ni/BIDC-900 and the non-metal doped counterpart cells were evaluated using galvanostatic charge/discharge at 0.05 C (Fig. 5.9) S/Ni/BIDC-900, with a low sulfur loading of $1.5 \text{ mg}_S \text{ cm}^{-1}$, delivered a competitive discharge capacity of 1006 mAh g^{-1} for the first cycle, which decreased to 857 mAh g^{-1} by the end of the fifth cycle. The sample without Ni NPs, S/BIDC-900, with similar mass loading of sulfur at the 0.05 C, showed a discharge capacity of 445 mAh g^{-1} , which decreased to 397 mAh g^{-1} by the end of the fifth discharge cycle. The Sharp decay in the capacity at the first few cycles is a known feature of LSB and it is attributed to the growth of solid electrolyte interface (SEI) or an electrode passivation layer.²¹ These film formations are due to undesired reactions of polysulfides and lithium ions nearby the surface of the electrodes, after the layer formation these side reactions are stopped and the capacity of the battery stabilizes at the lower values.²² The plateau regions of the discharge curve, in which the voltage changes are nominal, indicates the electrochemical reactions. The discharge curve has two plateau regions correspond to the long-chain lithium polysulfide and the short-chain lithium polysulfides respectively. The discharge curve for both samples shows similar features.

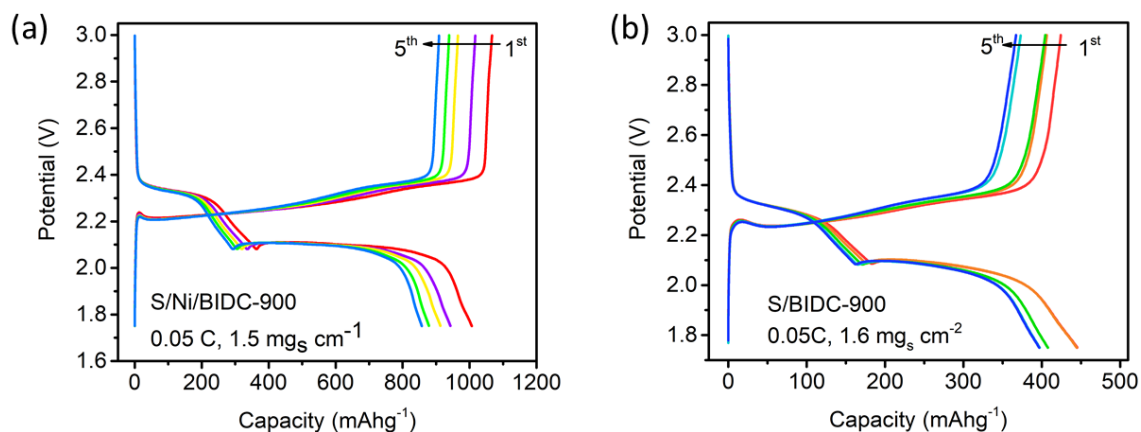


Figure 5.9 The charge/discharge voltage profile for the 5 cycles at 0.05 C for (a) S/Ni/BIDC-900 and (b) S/BIDC-900.

Following the guideline provided by US Department of Energy (DOE), a higher mass loading of sulfur has greatly sought after. Thicker cathode casts have been prepared and the yielded discharge capacity directly correlates with sulfur loading, in which coin cells with higher loading of sulfur deliver lower capacities. For a coin cell with the sulfur loading of $4.20 \text{ mg}_S \text{ cm}^{-2}$, discharge capacities of 662, 382, 287, 167, 58, 27 mAh g^{-1} at Crates of 0.05, 0.1, 0.2, 0.5, 1 and 2C, respectively were collected (Fig. 5.10). The comparison between S/Ni/BIDC-900 coin cells with 1.5 and $4.2 \text{ mg}_S \text{ cm}^{-2}$ shows that with the S loading of 2.8 times higher the capacity is lowered from 1006 mAh g^{-1} to 662 mAh g^{-1} . It is expected that the insulating nature of sulfur will hamper the capacity of the coin cell.

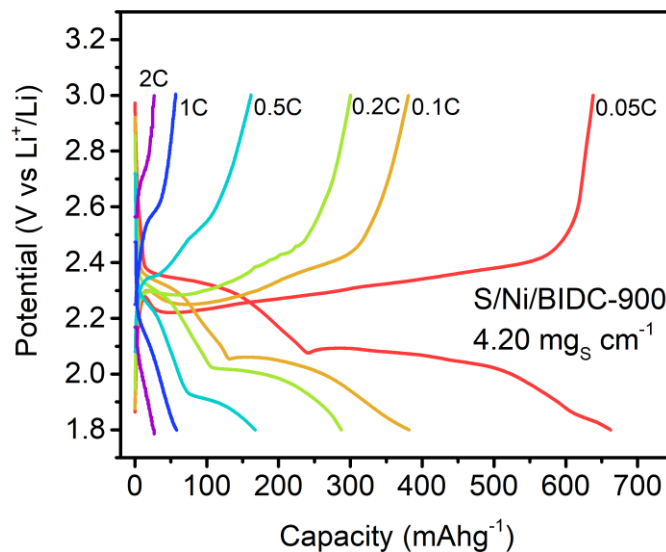


Figure 5.10 The charge/discharge profile of S/Ni/BIDC-900 with S loading of $4.20 \text{ mg}_s \text{ cm}^{-1}$ at 0.05-2C.

The rate performance of the S/Ni/BIDC-900 was investigated using a coin cell with a sulfur loading of $4.2 \text{ mg}_s \text{ cm}^{-2}$ at 0.05-2C. The specific capacities collected at 0.05C were unstable at the beginning and decreased from 662 mAh g^{-1} to 533 mAh g^{-1} by the end of the 10th cycle, due to the formation of SEI layer followed by the capacities at 0.1-2 C rates showing minimal loss of capacity at each C rates. Upon repetition of the charge/discharge measurements at 1C followed by 0.1C, 99% coulombic efficiency and capacity retention was observed (Fig 5.11)

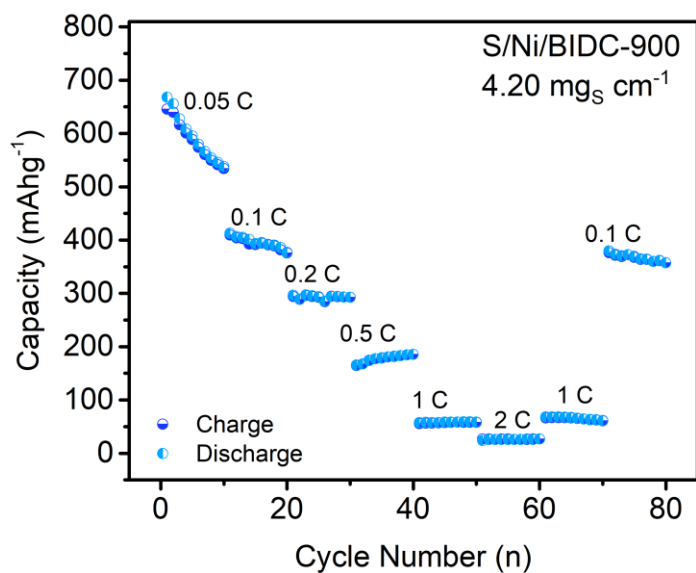


Figure 5.11 The rate performances of S/Ni/BIDC-900 at current densities varying from 0.05 to 2C.

Long-term stability and coulombic efficiency of S/Ni/BIDC-900 were studied. For these measurements, the coin cell used had a mass loading of $2.67 \text{ mg}_S \text{ cm}^{-2}$ at 0.1C. Throughout the 50 cycles performed the coin cell shows a 35% capacity loss, with capacity decay of 0.7% per cycle, but the coulombic efficiency remains above 96% (Fig 5.12). The high coulombic efficiency for the S/Ni/BIDC-900, is traced back to Ni NPs acting as a catalytic center for the redox reaction. The strong interaction between Lewis acid Ni (II) and Ni (III) centers and the polysulfide base species decreases the migration of the soluble polysulfides and keeps them trapped in the carbon porous structure leading to improvement in coulombic efficiency.²³

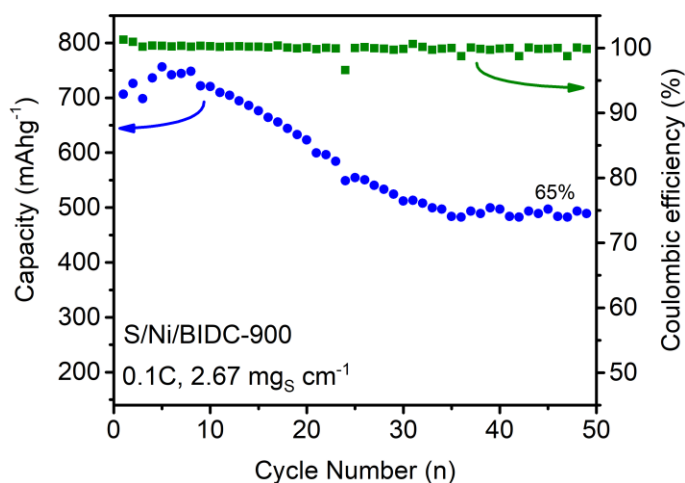


Figure 5.12 long-term stability (50 cycles) and coulombic efficiency of S/Ni/BIDC-900.

5.4 Outlook

The shortcomings of the S/Ni/BIDC-900, especially loss of activity, suggest certain areas can be improved. The utilization of a high surface area doped porous carbon support, with high pore volume, has many advantages such as providing the required conductive support, enabling a high sulfur loading, and immobilizing soluble LPSs during cycling. By using BIDC-900 as sulfur host, high sulfur loading of 70% has been achieved but the high loading does not lead to a high capacity even at 0.05 C, and loss of activity becomes problematic as the battery is cycled. The inefficient utilization of sulfur or loss of the active materials leads to the overall low capacity. In here, the N-doped carbon matrix is also the support for Ni NPs deposited through SEA and greatly contributes to particle distribution which prevents particle agglomeration. The initial particle distribution is depicted through HRTEM images, but studying the cycled battery is still required and can be greatly beneficial for understating the Ni NPs role in the adsorption of LPSs during cycling, as

agglomeration can hamper the catalytic role of Ni NPs in this process. Inadequate adsorption of LPSs in this process is also contributing to low sulfur utilization and the consequential low capacity. In the XPS discussion, it was shown that Ni cation complexes are adsorbed on carboxylic groups and not only on nitrogen sites, which might be due to low content of nitrogen in BDC-900. Therefore, we suggest that N-doped support with a high content of nitrogen might be more suitable for use in SEA. The effects of the low content of functional groups suitable for adsorption of Ni complexes are also apparent in the ICP results as only 45% of the Ni cation introduced into the solution was adsorbed on the support. Increasing the Ni NPs loading can be more beneficial toward the catalytic aspect of the carbon-based support; it also provides more sites for the adsorption of LPSs and thus improve battery cycling.

5.5 conclusion

A cathode material for lithium-sulfur batteries, utilizing small Ni nanoparticles (~4.3 nm) deposited on high specific surface area nitrogen-doped carbon support has been developed (Ni/BIDC-900). HRTEM images showed a high distribution of the Ni NPs on the surface of the carbon support. Ni/BIDC-900 and pristine BIDC-900 were studied as a cathode host for Li-S batteries and the effects of ~1 wt% Ni NPs loading on the performance of the coin cell have been studied. The CV data showed that S/Ni/BIDC-900 has higher peak current intensities at a scan rate of 0.1 mV s^{-1} in both reduction and oxidation waves. Also, the reduction wave had a positive shift toward higher potentials for S/Ni/BIDC-900. Galvanostatic charge/discharge performance of the S/Ni/BIDC-900 and S/BIDC-900 at a sulfur loading of $\sim 1.5 \text{ mg}_S \text{ cm}^{-2}$ yielded capacities of 1006 and 445 mAh g^{-1} , respectively at 0.05C. To increase the S loading, thicker cathodes were prepared and their performance was studied in a coin cell setting. The mass loading of $4.2 \text{ mg}_S \text{ cm}^{-2}$, yielded a discharge capacity of 667 mAh g^{-1} at 0.05C. The S/Ni/BIDC-900 showed good capacity retention. The long-term stability result showed a 35% loss of activity after 50. We believe longer battery cycling studies would be needed to fully understand the stability and overall performance of S/Ni/BIDC-900. Our finding in this study suggests that carbon support with a higher content of nitrogen is more suitable for the adsorption of Ni cations and the overall higher loading of the Ni NPs, which greatly contributes to the catalytic aspect of the carbon electrode used in our study for the utilization of high sulfur loading and adsorption of soluble LPSs for more efficient cycling.

References

- (1) Ding, Y.; Cano, Z. P.; Yu, A.; Lu, J.; Chen, Z. Automotive Li-Ion Batteries: Current Status and Future Perspectives. *Electrochem. Energy Rev.* **2019**, *2* (1), 1–28.
- (2) Yin, Y. X.; Xin, S.; Guo, Y. G.; Wan, L. J. Lithium-Sulfur Batteries: Electrochemistry, Materials, and Prospects. *Angew. Chemie - Int. Ed.* **2013**, *52* (50), 13186–13200.
- (3) Lim, W. G.; Kim, S.; Jo, C.; Lee, J. A Comprehensive Review of Materials with Catalytic Effects in Li–S Batteries: Enhanced Redox Kinetics. *Angew. Chemie - Int. Ed.* **2019**, *58* (52), 18746–18757.
- (4) Ashourirad, B.; Arab, P.; Islamoglu, T.; Cychosz, K. A.; Thommes, M.; El-Kaderi, H. M. A Cost-Effective Synthesis of Heteroatom-Doped Porous Carbons as Efficient CO₂ Sorbents. *J. Mater. Chem. A* **2016**, *4* (38), 14693–14702.
- (5) Jia, Y. F.; Xiao, B.; Thomas, K. M. Adsorption of Metal Ions on Nitrogen Surface Functional Groups in Activated Carbons. *Langmuir* **2002**, *18* (2), 470–478.
- (6) Lopez-Ramon, M. V.; Stoeckli, F.; Moreno-Castilla, C.; Carrasco-Marin, F. On the Characterization of Acidic and Basic Surface Sites on Carbons by Various Techniques. *Carbon N. Y.* **1999**, *37* (8), 1215–1221.
- (7) Lambert, S.; Job, N.; D’Souza, L.; Pereira, M. F. R.; Pirard, R.; Heinrichs, B.; Figueiredo, J. L.; Pirard, J. P.; Regalbuto, J. R. Synthesis of Very Highly Dispersed Platinum Catalysts Supported on Carbon Xerogels by the Strong Electrostatic Adsorption Method. *J. Catal.* **2009**, *261* (1), 23–33.
- (8) Wong, A.; Liu, Q.; Griffin, S.; Nicholls, A.; Regalbuto, J. R. Synthesis of Ultrasmall, Homogeneously Alloyed, Bimetallic Nanoparticles on Silica Supports. *Science* **2017**, *358* (6369), 1427–1430.
- (9) Schreier, M.; Regalbuto, J. R. A Fundamental Study of Pt Tetraammine Impregnation of Silica: 1. The Electrostatic Nature of Platinum Adsorption. *J. Catal.* **2004**, *225* (1), 190–202.
- (10) Manoj, B.; Kunjomana, A. G. Study of Stacking Structure of Amorphous Carbon by X-Ray Diffraction Technique. *Int. J. Electrochem. Sci.* **2012**, *7* (4), 3127–3134.
- (11) Kang, D. S.; Lee, S. M.; Lee, S. H.; Roh, J. S. X-Ray Diffraction Analysis of the Crystallinity of Phenolic Res-in-Derived Carbon as a Function of the Heating Rate during the Carbonization Process. *Carbon Lett.* **2018**, *27* (1), 108–111.
- (12) O’Connell, K.; Regalbuto, J. R. High Sensitivity Silicon Slit Detectors for 1 Nm Powder XRD Size Detection Limit. *Catal. Letters* **2015**, *145* (3), 777–783.
- (13) Abdelmoaty, Y. H.; Tessema, T.-D. D.; Norouzi, N.; El-Kadri, O. M.; Turner, J. B.

- M. G. M.; El-Kaderi, H. M. Effective Approach for Increasing the Heteroatom Doping Levels of Porous Carbons for Superior CO₂ Capture and Separation Performance. *ACS Appl. Mater. Interfaces* **2017**, *9* (41), 35802–35810.
- (14) Kaviani, S.; Mohammadi Ghaleni, M.; Tavakoli, E.; Nejati, S. Electroactive and Conformal Coatings of Oxidative Chemical Vapor Deposition Polymers for Oxygen Electroreduction. *ACS Appl. Polym. Mater.* **2019**, *1* (3), 552–560.
- (15) Norouzi, N.; Choudhury, F.; El-Kaderi, H. M. Iron Phosphide Doped-Porous Carbon as an Efficient Electrocatalyst for Oxygen Reduction Reaction. *ACS Appl. Energy Mater.* **2020**, *3* (3), 2537–2546.
- (16) Deng, C.; Zhong, H.; Li, X.; Yao, L.; Zhang, H. A Highly Efficient Electrocatalyst for Oxygen Reduction Reaction: Phosphorus and Nitrogen Co-Doped Hierarchically Ordered Porous Carbon Derived from an Iron-Functionalized Polymer. *Nanoscale* **2016**, *8* (3), 1580–1587.
- (17) Grosvenor, A. P.; Biesinger, M. C.; Smart, R. S. C.; McIntyre, N. S. New Interpretations of XPS Spectra of Nickel Metal and Oxides. *Surf. Sci.* **2006**, *600* (9), 1771–1779.
- (18) Sun, Z.; Zhang, J.; Yin, L.; Hu, G.; Fang, R.; Cheng, H.; Li, F. Conductive Porous Vanadium Nitride/Graphene Composite as Chemical Anchor of Polysulfides for Lithium-Sulfur Batteries. *Nat. Publ. Gr.* **2017**.
- (19) Wang, Y.; Liu, W.; Liu, R.; Pan, P.; Suo, L.; Chen, J.; Feng, X.; Wang, X.; Ma, Y.; Huang, W. Inhibiting Polysulfide Shuttling Using Dual-Functional Nanowire/Nanotube Modified Layers for Highly Stable Lithium-Sulfur Batteries. *New J. Chem.* **2019**, *43* (37), 14708–14713.
- (20) Liu, Z.; Zhou, L.; Ge, Q.; Chen, R.; Ni, M.; Utetiwabo, W.; Zhang, X.; Yang, W. Atomic Iron Catalysis of Polysulfide Conversion in Lithium–Sulfur Batteries. *ACS Appl. Mater. Interfaces* **2018**, *10* (23), 19311–19317.
- (21) Arora, P.; White, R. E.; Doyle, M.; Carolina, S. Capacity Fade Mechanisms and Side Reactions in Lithium-Ion Batteries. *J. Electrochem. Soc.* **1998**, *145* (10), 3647–3667.
- (22) Risse, S.; Angioletti-uberti, S.; Dzubielia, J.; Ballauff, M. Capacity Fading in Lithium/Sulfur Batteries: A Linear Four-State Model. *J. Power Sources* **2014**, *267*, 648–654.
- (23) Zheng, J.; Tian, J.; Wu, D.; Gu, M.; Xu, W.; Wang, C.; Gao, F.; Engelhard, M. H.; Zhang, J. G.; Liu, J.; Xiao, J. Lewis Acid-Base Interactions between Polysulfides and Metal Organic Framework in Lithium Sulfur Batteries. *Nano Lett.* **2014**, *14* (5), 2345–2352.

Chapter 6

Conclusions and Outlook

In this dissertation, supported metal nanoparticles (NPs) on high surface area supports are synthesized and their surface and bulk characteristics are tailored toward addressing the current challenges of catalytic materials for various applications. NPs with controlled size, composition, and dispersity over high surface area supports are among the highly sought-after materials in energy conversion and storage and catalytic processes. In the process of designing the studies practiced here, we have used facile and scalable synthesis techniques while minimizing the cost of materials to achieve enhanced reaction kinetics, catalytic activity, and efficiency.

In the first project discussed in chapter 3, we reported a facile synthesis route to prepare iron phosphide doped porous carbon support as a cathode catalyst for oxygen reduction reaction in alkaline and acidic fuel cells. Currently, platinum-doped carbon (20 wt% Pt/C) and platinum group metals are being used as catalysts in fuel cells. Sluggish ORR mechanism and lack of long-term stability demand for a more sustainable, inexpensive, and kinetically efficient replacement catalysts. Inexpensive and commercially available materials such as triphenylphosphine, iron (II) chloride, and zinc (II) chloride

were used for the synthesis of the samples through carbonization/chemical activation. Various reaction parameters such as calcination temperature, chemical activator ratio and composition, and metal presence are studied for the development of new catalysts with superior electrocatalytic activity. Iron phosphide nanoparticles incorporated in a phosphorus-doped porous carbon, with a high specific area ($S_{\text{BET}} = 967 \text{ m}^2 \text{ g}^{-1}$) selectively reduce O_2 via an efficient reaction pathway of 4 e^- reduction reaction and exhibit superior long-term stability than Pt/C. This catalyst is also inert toward methanol crossover.

In the second project discussed in chapter 4, ultrasmall, well-alloyed bimetallic NPs are deposited on high surface area silica support ($S_{\text{BET}} = 350 \text{ m}^2 \text{ g}^{-1}$) through facile synthesis technique of strong electrostatic adsorption (SEA) and used as catalysts for Suzuki-Miyaura cross-coupling (SCC) reactions. In principle, SEA is carried using support's point of zero charge (PZC) which is the pH value at which the net charge of the surface is zero. At pH values above PZC, the surface of the support deprotonates and at pH values below PZC the surface of the support protonates. Here, silica support with PZC of 3.6 is dispersed in a solution with a pH of 11.8 then active metal Pd and base metals (Cu, Ni, and Co) cations are deposited on the silica support through SEA. After reduction with 5% H_2 (in argon), it yields homogeneously alloyed nanoparticles with an average size of 1.3 nm. All bimetallic catalysts were found to be highly active toward SCC surpassing the activity of monometallic Pd/SiO₂. Remarkably, a catalyst consisting of Cu and Pd, CuPd/SiO₂, performed the SCC with a turnover frequency of 248000. The combination of

Pd with base metals helps in retaining the Pd⁰ status by charge donation from base metals to Pd and thus facilitates the SCC.

In the third project discussed in chapter 5, a catalytically active material consisting of small Ni NPs supported on high surface area nitrogen-doped porous carbon ($S_{\text{ABET}} = 3560 \text{ m}^2 \text{ g}^{-1}$) was used as a cathode in lithium-sulfur batteries (LSB). Previously established high surface area carbon-based materials used as LSB cathodes are insufficient to address the shortcomings of these batteries especially the shuttle effect. The electrochemical performance of LSB can be largely improved by enhancing reversible conversion of lithium polysulfides to Li₂S during discharge and to elemental S during charge. The transformation of carbon electrodes into catalytic electrodes has shown the capability to enhance the overall activity of LSB. In our studies, Ni NPs act as active centers for the adsorption of polysulfides during the discharge process and rapidly convert them to Li₂S while catalyzing Li₂S oxidation to sulfur in the reverse process. We have demonstrated that the addition of Ni NPs improves the reaction kinetics and capacity retention of LSB.

The use of inexpensive transition metal NPs incorporated on the high surface area carbon and silica supports have shown great potential for replacing scarce and expensive metals like Pt and Pd which are well-known for their high catalytic activity. We have shown that incorporation of transition metal NPs with controlled size and composition, while facilitating their uniform dispersion on high surface area supports, can be beneficial for many applications.